Vibrational Raman Scattering of Liquid Water

Quantitative Incorporation into a Numeric Radiative Transfer Model of the Atmosphere-Ocean System and Analysis of its Impact on Remote Sensing Applications

vorgelegt von

Jonas von Bismarck

Dissertation

zur Erlangung des akademischen Grades eines
Doktors der Naturwissenschaften
am Fachbereich für Geowissenschaften
der Freien Universität Berlin

1. Gutachter: Prof. Dr. Jürgen Fischer
2. Gutachter: Prof. Dr. Ralf Bennartz

Tag der Disputation: 28. April 2015

Contents

Kurzfassung

Die inelastische Raman Streuung von Licht an Vibrationszustandsübergängen des flüssigen Wassers hat einen starken Einfluss auf das Spektrum des kurzwelligen Lichtes welches mit dem Ozean in Wechselwirkung steht. Hieraus ergibt sich die Notwendigkeit, diesen Effekt für eine akkurate Beschreibung des Strahlungstransports im Ozean und der Atmosphäre zu berücksichtigen. Dies trifft insbesondere auf Strahlungstransport Simulationen für den Anwendungsbereich der Ozeanfernerkundung zu, kann aber aufgrund der Größenordnung des Effekts auch eine Rolle bei der Atmosphärenfernerkundung über dem Ozean spielen. Während einige bestehende Strahlungstransportmodelle den Effekt qualitativ berücksichtigen, bestand jedoch ein Mangel an Modellen welche den Einfluss des Effekts auf das gekoppelte Atmosphäre-Ozean System unter Berücksichtigung der azimutalen Winkelabhängigkeit vorhersagen können.

In der vorliegenden Arbeit wurde daher ein Verfahren zur Berücksichtigung der inelastischen Raman Streuung an Vibrationsübergängen des flüssigen Wassers in einem numerischen Strahlungstransportmodell entwickelt, implementiert, validiert und angewendet. Zunächst werden hierzu die theoretischen und empirischen Grundlagen beschrieben, die zur genauen Berechnung des Effekts notwendig sind. Ferner wurden ebenfalls die Grundlagen weiterer inelastischer Streuprozesse, insbesondere der atmosphärischen Raman Streuung aber auch der Fluoreszenz von Ozeaninhaltsstoffen, zusammengetragen und für ersteres in Form von Vorprozessoren für die künftige Verwendung im Strahlungstransportmodell vorbereitet.

In dem folgenden Abschnitt wird das Strahlungstransportmodell, mit Schwerpunkt auf den neu entwickelten Verfahren zur Einbindung der inelastischen Streuung, erläutert. Dies beinhaltet die Berechnung der Streueffekte mit Fourier-entwickelter Azimutalabhängigkeit und eine akkurate aber dennoch schnelle Methode zur Berechnung der Raman Streubeiträge in optisch dicken, homogenen Schichten. Ferner wurden einige Erweiterungen an dem Modell bezüglich der Berechnung von Streu- und Absorptionseigenschaften des Wassers in Abhängigkeit von Temperatur und Salinität vorgenommen. Ebenfalls werden die in der Arbeit Verwendung findenden bio-optischen Modelle beschrieben.

Ein weiterer Abschnitt befasst sich mit der Validierung der neuen Modellversion. Dies stellte aufgrund des Mangels an zur Verfügung stehenden geeigneten Referenzmodellen, die ebenfalls die Winkelabhängigkeit der Raman Streuung korrekt berücksichtigen, eine Herausforderung dar. Daher wurde ein gemischter Ansatz gewählt, der aus Modellvergleichen für einfache kanonische Probleme, der Überprüfung der Konsistenz der beteiligten Berech-

nungen sowie dem qualitativen Vergleich der Winkelabhängigkeit mit erwarteten Verläufen bestand.

Der letzte Abschnitt stellt einige Anwendungen des neuen Modells vor. Hervorzuheben ist eine umfangreiche Studie des Einflusses der Raman Streuung auf die Lichtfelder in Ozean und Atmosphäre im sichtbaren Spektralbereich. So beträgt der Anteil des zusätzlich erzeugten Lichtes gegenüber der Vernachlässigung des Effekts im aufwärtsgerichteten Strahlungsfeld an der Ozeanoberfläche in klaren Gewässern von 10 bis über 30%. Es stellte sich heraus dass eine Vernachlässigung der Winkelabhängigkeit des Effekts zu Fehlern in den Radianzen von mehreren Prozent führen kann. Da der Anteil des aus dem Ozean entwichenen Lichtes am Oberrand der Atmosphäre im sichtbaren Strahlungsbereich in grober Schätzung nur noch etwa 10% beträgt, wurde auch untersucht wie stark der Effekt die Signale am Oberrand der Atmosphäre beeinflusst, um Rückschlüsse auf Satelliten-Fernerkundungsverfahren zu ermöglichen. Auch hier können die Raman Beiträge etliche Prozent betragen. Dies ist hauptsächlich im blauen und grünen Spektralbereich der Fall und weniger im roten, wo der Ozean stark absorbiert. Es wird auch gezeigt, dass selbst in dem Winkelbereich über einem durch Wind aufgerauten Ozean, der durch direkte Sonnenreflexe beeinflusst ist, der Beitrag noch durchaus signifikant sein kann. Eine weitere Studie beschäftigt sich spezifisch mit dem Effekt in den Kanälen des künftigen abbildenden Spektrometers OLCI der ESA Sentinel-3 Mission. Hierbei konnte u.A. gezeigt werden, dass der Raman Beitrag selbst in den roten Spektralkanälen noch technisch von dem Instrument aufgelöst werden kann. Der abschließende Beitrag stellt ein Gemeinschaftsprojekt unseres Instituts mit der Firma Brockmann Consult vor, in der die neue Strahlungstransportmodellversion erfolgreich zur Erstellung einer Lookup-Tabelle für ein allgemeines Fernerkundungsverfahren für Inhaltsstoffe des Ozeans zur Verwendung kam.

Die Entwicklungsarbeit der ersten Modellversion sowie deren Validierung und eine Sensitivitätsstudie bezüglich der Beiträge der Ozean Raman Streuung in den Kanälen des künftigen OLCI Instruments auf dem ESA Satelliten Sentinel-3 wurden im Rahmen des ESA finanzierten *support to science* Projektes *WaterRadiance* gefördert (von Bismarck and Fischer [123], Hollstein et al. [45], von Bismarck and Fischer [124], Rüdiger Röttgers [103]. Der Abschnitt 5.3 in der vorliegenden Arbeit wurde dem im Rahmen des Projekts verfassten Validierungsbericht[124] entnommen. Teile der Arbeit wurden ebenfalls, mit unterschiedlichen Schwerpunkten, auf verschiedenen internationalen Konferenzen vorgestellt (u.A. von Bismarck and Fischer [122, 125]). Eine spezifische Studie bezüglich des Effekts einer vereinfachten Behandlung der Raman Streuung wurde als als Konferenzveröffentlichung des *International Radiation Symposium 2012* veröffentlicht (von Bismarck and Fischer [121]).

Abstract

The inelastic (Raman) scattering of daylight due to due vibrational state transitions of liquid water is known to have a significant influence on the spectra of ocean leaving radiation. This effect therefore needs to be considered in radiative transfer (RT) models of the atmosphere-ocean system for which a high accuracy is required, e.g. for ocean color remote sensing applications. While many qualitative studies of the effect have been published in the past decades, a lack of fast radiative transfer models of the combined atmosphere-ocean system that allow for a detailed angular and spectral investigation of the effect had been identified. In this thesis, a method for the quantitative and angular resolved incorporation of water Raman scattering effects into a matrix-operator radiative transfer model of the coupled atmosphere-ocean system has been developed, implemented, validated, and applied to several problems. The theoretical and empirical basis for the optical properties of Raman scattering, including the spectral redistribution, the phase function, and the scattering coefficient, are discussed, as they are important input values for a radiative transfer model. Furthermore, the optical properties of two other inelastic scattering effects are discussed: the rotational Raman scattering of atmospheric nitrogen and oxygen, and the fluorescence of yellow substance and chlorophyll in the ocean. An approach focused on accuracy and computation speed was developed for the incorporation of water Raman scattering into an existing radiative transfer model based on the matrix-operator method. Furthermore, the new model was accompanied by preprocessors for the salinity and temperature dependent computation of elastic scattering and absorption-coefficients of water, as well as for the optical properties of dissolved and suspended oceanic matter. The new RT model version was then successfully validated by a comparison of the results for canonical problems to those of other radiative transfer models. To validate components of the model that were not featured by the other models, e.g. the precise angular dependence of the Raman contribution, sanity and consistency checks of contributing model components were performed. Applications performed with the new model include a detailed study of the Raman contribution to radiation emerging from Case 1 waters, which reaches several tens of percent in the visible spectral range for clear water. The reduction of the effect in turbid waters and the effect of the water salinity was also studied. Angular effects have proven to be significant, whereas higher orders of Raman scattering are shown to be of minor importance. The Raman contribution was also studied at the top of the atmosphere, and it was shown that the Raman scattered radiation fraction for a standard case will be detectable in all visible channels of the upcoming OLCI instrument on the ESA Sentinel-3

Satellite. Finally, the new RT model version was used in an ocean constituent retrieval scheme, which is adaptable to the spectral channels of different remote sensing satellites.

Motivation and Overview

One may summarize the general objective of all geosciences being to provide the best possible description of the Earth's system state and its temporal evolution in the past, present and future. The motivation for this thesis is aimed at the improvement of the description of the present state of the ocean and atmosphere. The variety of tools available for the direct and indirect measurements of the state of the atmosphere and ocean has increased rapidly in the past century. With the beginning of the second half of the 20th century, the field of optical remote sensing of the atmosphere utilized the theory of radiative transfer (RT), which was initially developed by astrophysicists (i.a. Schwarzschild [106] and Chandrasekhar [16]) to infer stellar properties from its spectrum, to relate measured solar and sky radiances to atmospheric properties. With the launch of environmental satellites in the last quarter of the century, a new class of remote sensing tools that enabled global and temporal coverage were available. However, in the nadir viewing geometry of passive radiometers, the relation between many atmospheric and oceanic properties and the measured radiometric quantities had become so complex it could not be described analytically and therefore numeric methods based on the principals of radiative transfer theory became an essential part of remote sensing applications. The latter process was driven by the fact that available computation power increased exponentially with time, being a manifestation of the prediction of Moore's law. I.a. owing to the description of monochromatic radiation propagation in the basic RT formalisms, the contributions of trans-spectral processes have often been neglected in numeric radiative transfer models. Of the latter processes, the vibrational Raman scattering of clear liquid water is an effect known to cause a significant spectral distribution of radiation emerging from clear and modestly turbid ocean waters, with errors of up to several 10% induced to computed water-leaving radiances in the visible spectral range if the effect is neglected. The latter therefore not only affects retrieval processes of ocean constituents, but may also introduce a bias to the retrieval of aerosol and trace gas properties above the ocean. While approximative and more or less qualitative inclusions of the effect in radiative transfer simulations had been performed in the past decades, a lack of detailed quantitative examinations of the effect in terms of spectral and angular influence on the radiation distribution in the coupled atmosphere-ocean could be stated.

The dissertation contains the successful work of developing and implementing a method to quantitatively and efficiently incorporate the effects of water Raman scattering into the radiative transfer model MOMO (Matrix Operator MOdel) of the atmosphere-ocean system

and its application to different scientific problems. In chapter 1 the state of the art of the theoretical and phenomenological description of the optical properties of clear water Raman scattering and other important inelastic scattering effects is presented. These form the theoretical basis for the simulation of the effect. Chapter 2 introduces the radiative transfer model and in detail describes the methods that were developed for the incorporation of the Raman scattering effect. Chapter 3 discusses the models involved for the determination of the inherent optical properties of the ocean and atmosphere, some of which have been implemented in the framework of the thesis, including a model for the accurate treatment of salinity and temperature effects on clear water absorption and scattering as well as two bio-optical models for the simulation of Case 1 and Case 2 waters. Chapter 4 introduces the successive Model version that were developed in the thesis, starting with the initial code that was developed in the framework of the ESA *support to science project* WaterRadiance and the following versions that focused on the improvement of computation speed and accuracy, to the future code versions that are still in the development stage at our institute. In chapter 5 the successful validation efforts for the different code versions are discussed. Chapter 6 introduces a selection of applications that featured the newest model version. The effects of water Raman scattering on the light-field in the ocean-atmosphere were quantified in detail for a variety of Case 1 water types. Emphasis is put on the effect of omitting Raman scattering and on errors induced by a simplified treatment with a detailed discussion of the angular dependence of the effects. Furthermore, a study of the effect on future measurements performed by the OLCI instrument on the upcoming ESA Sentinel-3 mission is introduced. Finally, an overview of the DLR/BMWi funded SIOCS (Sensor Independent Ocean Colour Service) project is given, which features MOMO Raman model outputs in a scheme for the retrieval of ocean constituents from satellite images.

Introduction

Radiative transfer theory describes the relationship between radiation propagation in a medium and quantities defining its macroscopic optical properties of absorption, emission and scattering, governed by the radiative transfer equation. The inherent optical properties of the medium are assumed to be independent of the radiation intensity in the short time frame of light interaction, with the exclusion of indirect influences such as temperature changes on a longer timescale. The development of the concepts of radiative transfer theory was initially driven by scientists studying the photospheres of stars in the early 20th century and later applied to nuclear and atmospheric science problems around the middle of the century. When the concepts of radiative transfer theory are applied to the Earth's atmosphere and ocean, the inherent optical properties of both have to be derived from theoretical and empirical considerations in a sufficient accuracy. The principals of defining these optical properties in terms of inelastic scattering are the subject of chapter 1, whereas the definition of absorption and elastic scattering properties of the ocean and atmosphere and their relation to microphysical quantities will be discussed in chapter 3. Due to the lack of known solutions of the radiative transfer equation for realistic states of the combined atmosphere-ocean system, chapter 2 will deal with numeric radiative transfer theory and our approach to include vibrational water Raman scattering into a computer model based on the latter. Chapter 5 will discuss the successful validation efforts for the radiometric quantities predicted by the model and chapter 6 will introduce results and applications featuring the new model.

Chapter 1

Optical Properties of Raman Scattering

1.1 Introduction

In contrast to elastic scattering of radiation, inelastic scattering refers to those scattering processes that exhibit a difference in radiation wavelength of incident and scattered radiation. While first predicted by Smekal [108] in 1923, the effect of inelastic light scattering was first observed in fluids by C. V. Raman and K. S. Krishnan in 1928 [94]. The observed Raman spectra originate from an energy loss or gain of a photon when enabling a molecular energy state transition when scattered at the molecule. The resulting spectral lines are grouped into those for so called Stokes shifts, with an energy loss of the photon, and anti-Stokes shifts, were the scattered photon has a higher frequency. The molecular energy state transition probability depends on the population of the initial- and higher energy states and the Stokes lines are usually more pronounced than the anti-Stokes lines at room temperature. While many different types of molecular transitions are known to eventually participate in inelastic scattering events, only a few of these effects contribute to radiometric quantities in an order of magnitude that makes there consideration relevant for atmosphere, land surface or ocean remote sensing.

The Stokes shift introduced by inelastic scattering by vibrational transitions of the O-H bonds of liquid water is known to significantly redistribute radiation spectrally in the ocean. The effect accounts for up to several tens of percent in terms of Raman scattered fraction to the water-leaving radiation in the visible spectral range. Due to its order of magnitude, neglecting the effect in radiative transfer simulations not only affects the accuracy of predicted ocean color, but also may have a significant influence on the retrieval of atmospheric properties over water. This effect was therefore prioritized and chosen to be the initial angular dependent inelastic scattering effect that should be introduced to our radiative transfer model.

Although the vibrational Raman scattering (VRS) of liquid water is the main topic of this thesis, two other forms of inelastic scattering, that justify inclusion in radiative transfer computations due to their impact on certain fields of remote sensing applications, shall be introduced in this section to encourage a later inclusion by synergistically us-

ing the structures developed for the inclusion of VRS in our model. This includes the Stokes and anti-Stokes spectra originating from rotational Raman scattering (RRS) by atmospheric molecules, which account for the bulk of the Fraunhofer line filling observed in atmospheric radiance spectra in the UV and visible spectral range [50]. Although the latter effect accounts for only roughly 4% of all scattering events in the atmosphere [110], the smoothing of fine spectral features owed to the Raman shifts can not be accurately described by treating the effect as an additional "pseudo" absorber. In the remote sensing of absorbing trace gases with sensors featuring a sufficiently high spectral resolution to resolve the mentioned spectral features, the correct consideration of the effect in a retrieval can therefore be necessary. Examples include the ground-based DOAS (Differential Optical Absorption Spectroscopy) retrievals and the satellite based trace gas retrievals by GOME (Global Ozone Monitoring Experiment) and OMI (Ozone Monitoring Instrument). Furthermore, the remote sensing of vegetation fluorescence from satellite sensors such as TANSO-FTS (Thermal And Near infrared Sensor for carbon Observations - Fourier Transform Spectrometer) on GOSAT (Greenhouse gases Observing SATellite) or the FLORIS (FLuORescence Imaging Spectrometer) instrument on the proposed ESA FLEX (FLuorescence Explorer) mission is an application which may be affected by the RRS line filling effect (see e.g. Guanter et al. [41]). Fluorescence effects originating from electronic transitions in molecules are generally not considered a Raman scattering effect due to their fixed emission spectrum. Nevertheless, studying of the effects of chlorophyll and yellow substance fluorescence in the ocean in the red spectral region has a history in our institute and is of importance for ocean color retrievals in this spectral region (see e.g. Fischer et al. [29]), and will therefore also be briefly discussed.

1.2 Raman Scattering in Radiative Transfer Theory

The *interaction principle* is a concept arising from energy conservation considerations and the assumption of linearity for the interaction of radiation with a stratified medium, which expresses the radiation emerging from a finite medium in terms of the incident radiation and the radiation produced within the medium (see section 2.3 and [96, 39]). *"In the limit of vanishing thickness of the medium these principles lead to the integro-differential equations of radiative transfer."* (Peraiah [82]). For cases were the atmosphere-ocean system can be sufficiently represented by a plane-parallel medium with only a vertical coordinate, its monochromatic radiative transfer equation (RTE) can be expressed in the form:

$$|\mu|\frac{d}{d\tau}L(\tau,\mu,\phi) = -L(\tau,\mu,\phi) + J(\tau,\mu,\phi), \tag{1.1}$$

where μ is the cosine of the zenith angle θ and ϕ the azimuth angle of the incident radiation. The optical depth τ is used as a vertical position unit rather than the geometrical altitude z. The differential equation implies that the variation of the radiation intensity dL along an infinitesimal optical path $\delta\tau/\mu$ in a direction (μ,ϕ) at a vertical position τ is given by the sum of radiation-loss $-L$ and -gains J in that direction and at that position.

The radiation sources can be separated into a fraction J^E originating from elastic scattering and an inelastic fraction J^I, so that $J = J^E + J^I$. If a separate treatment of diffuse radiance and direct solar irradiance is desired, both fractions can be split up into a part treating single scattered solar radiation and a part for scattered diffuse radiation.

The decrease of incoming extraterrestrial direct solar irradiance S'° along its path through the atmosphere with the zenith angle μ'° to a given position τ due to extinction, described by the Lambert-Beer law[1], yields the direct irradiance available at τ:

$$E'^{\circ}(\tau) = S'^{\circ} e^{-\tau/\mu'^{\circ}}. \tag{1.2}$$

We define the single scattering albedo:

$$\omega_0 = \frac{b}{c}, \tag{1.3}$$

with b being the spectral scattering coefficient, $c = a + b$ the extinction coefficient and a the absorption coefficient. Furthermore, we define the phase function $P(\mu', \mu, \phi', \phi)$ describing the angular redistribution of incident radiation from (μ', ϕ') to (μ, ϕ) at the position τ due to elastic scattering processes. The single scattered fraction of J^E is then given by:

$$J^{\circ}(\mu, \phi) = \omega_0 P(\mu'^{\circ}, \mu, \phi'^{\circ}, \phi) E'^{\circ}(\mu'^{\circ}), \tag{1.4}$$

were ϕ'° is the solar azimuth angle which is normally by convention set to constantly be either 0° or 180°. To determine J^{diff}, the distribution of radiation from all directions (μ', ϕ') to a given direction of (μ, ϕ), the spherical integral of $P(\mu', \mu, \phi', \phi) L'(\mu', \phi')$ over the complete solid angle sphere Ω' has to be evaluated:

$$J^{diff}(\mu, \phi) = \omega_0 \int_{\Omega'} P(\mu', \mu, \phi', \phi) L'(\mu', \phi') d\Omega', \tag{1.5}$$

where $L'(\mu', \phi')$ is the local radiation field before the scattering process. As mentioned above, if L' would include the direct solar radiation, the right side of equation 1.5 would yield J^E rather than J^{diff}. Note that no sources of longwave emission are discussed due to our focus on the spectral region of daylight.

The inelastic fraction J^E accounts for trans-spectral scattering processes. Due to the wavelength shift the radiation undergoes during the scattering process, in addition to the angular integral a spectral integration over the wavelength range Λ' of radiation scattering

[1] If the path of direct radiance passes through a medium with a depth dependent real part of the refractive index, including discontinuities e.g. when entering a flat surfaced water body from the atmosphere, the change of μ'° due to refraction needs to be taken into account. Furthermore, the Lambert-Beer law is generally only valid for monochromatic radiation.

into the observation wavelength λ needs to be evaluated:

$$J^I(\mu,\phi,\lambda) = \frac{1}{c(\lambda)} \int\int_{\Omega'} \tilde{\beta}^I(\mu',\mu,\phi',\phi,\lambda',\lambda) L'(\mu',\phi',\lambda') d\Omega' d\lambda' \tag{1.6a}$$

$$+ \frac{1}{c(\lambda)} \int_{\Lambda'} \tilde{\beta}^I(\mu'^\circ,\mu,\phi'^\circ,\phi,\lambda',\lambda) E'^\circ(\mu'^\circ,\lambda') d\lambda'. \tag{1.6b}$$

were $\tilde{\beta}^I(\mu',\mu,\phi',\phi,\lambda',\lambda)$ is the volume scattering function of the sum of all elastic scattering processes. In the ocean this includes, but is not limited to, vibrational Raman scattering of clear water and chlorophyll fluorescence. In accordance with the notation for elastic scattering, the apostrophe denotes variables of the incident light-field at the excitation wavelengths λ'. If direct solar radiation is not present or is already contained in L', the second term in 1.6, describing the direct solar radiation that is Raman scattered, vanishes.

1.3 Vibrational Raman Scattering in Water

Vibrational Raman scattering by water is known to contribute significantly to the upwelling shortwave radiation leaving the ocean, especially if the water is clear. In water depths over a few ten meters, depending on the wavelength, Raman scattered photons account for the bulk of the radiation. The same is the case for water leaving radiances in some atmospheric absorption bands, due to line filling by the Raman scattered radiation. The magnitude of the vibrational Raman scattering contribution and the wide range of remote sensing applications that are affected by the negligence of the effect, lead to the decision to prioritize this inelastic scattering effect over other inelastic scattering effects regarding the implementation in our RT model.

The following sections discuss the optical properties of vibrational Raman scattering of liquid water, which form the basis for the inclusion of the effect in a radiative transfer model, described in chapter 2.

1.3.1 Raman Source

The trans-spectral process of Raman scattering contributes to the inelastic fraction J^I (equation 1.6). The Raman fraction of J^I can likewise be represented by a source term J^R describing the spectral and angular redistribution of radiation which is absorbed at the wavelength λ' and spectrally shifted and re-emitted at the observation wavelength λ:

$$J^R(\mu,\phi,\lambda) = \frac{1}{c(\lambda)} \int\int_{\Omega'} \tilde{\beta}^R(\mu',\mu,\phi',\phi,\lambda',\lambda) L'(\mu',\phi',\lambda') d\Omega' d\lambda' \tag{1.7a}$$

$$+ \frac{1}{c(\lambda)} \int_{\Lambda'} \tilde{\beta}^R(\mu'^\circ,\mu,\phi'^\circ,\phi,\lambda',\lambda) E'^\circ(\mu'^\circ,\lambda') d\lambda'. \tag{1.7b}$$

1.3.2 Raman Volume Scattering Function

The Raman volume scattering function $\tilde{\beta}^R$ in equation 1.7 describes the angular redistribution after the wavelength shift as well as the fraction of radiation being shifted to the emission wavelength λ from other wavelengths λ'. $c(\lambda)$ is the total extinction coefficient, -the sum of the absorption coefficient $a(\lambda)$ and the elastic- and inelastic-scattering coefficients $b(\lambda)$ and $b^R(\lambda)$, respectively. In contrast to rotational Raman lines dominating in the atmosphere, in vibrational water Raman scattering, only the Stokes shifts from a shorter to a longer wavelength are of significance ($\lambda > \lambda'$).

The water Raman volume scattering function $\tilde{\beta}^R$ may be separated into three factors, a wavelength dependent Raman scattering coefficient $b^R(\lambda')$, a normalized spectral redistribution function $f^R(\lambda', \lambda)$ depending on the spectral shift, and a phase function $P^R(\mu', \mu, \phi', \phi)$ depending on the angle between incident and scattered radiation:

$$\tilde{\beta}^R(\mu', \mu, \phi', \phi, \lambda', \lambda) = b^R(\lambda') f^R(\lambda', \lambda) P^R(\mu', \mu, \phi', \phi). \tag{1.8}$$

The definition of these three functions shall be discussed in the following.

1.3.3 Raman Phase Function

S. Porto showed in 1966 that there is a *"...one-to-one relationship between the depolarization factor [ρ] and the angular dependence of any Raman line..."* [88]. From theoretical considerations he derived the angular dependence of parallel ($I_{||}$) and perpendicularly ($I_{\perp}$) polarized Raman scattered radiation originating from a linear polarized light source (e.g. a laser)[88]:

$$I_{\perp} = C(3 + 3\rho)/\rho, \tag{1.9a}$$
$$I_{||} = C\{6 + [(3 - 3\rho)/\rho] \cos^2 \theta_s. \tag{1.9b}$$

Here, C is a proportionality constant. The scattering angle θ_s can be calculated from the zenith and azimuth angles with the following equation:

$$\cos \theta_s = \mu\mu' + \sqrt{1 - \mu^2}\sqrt{1 - \mu'^2} \cos(\phi - \phi'). \tag{1.10}$$

The Raman scattering phase function P^R is proportional to the sum of the parallel and perpendicular components ($I_{||} + I_{\perp}$) and is commonly shown in the following form [73, 35]:

$$P^R(\mu', \mu, \phi', \phi) = \frac{3}{16\pi} \frac{1 + 3\rho}{1 + 2\rho} \left(1 + \frac{1 - \rho}{1 + 3\rho} \cos^2 \theta_s\right) \tag{1.11}$$

The prefactors in equation 1.11 depend on the chosen normalization. Figure 1.1 shows the Raman Phase function in comparison to the elastic Rayleigh scattering function. Although the directionality of the Raman phase function is less pronounced than for Rayleigh scattering, the differences of approximately 30% between forward and sideward scattering

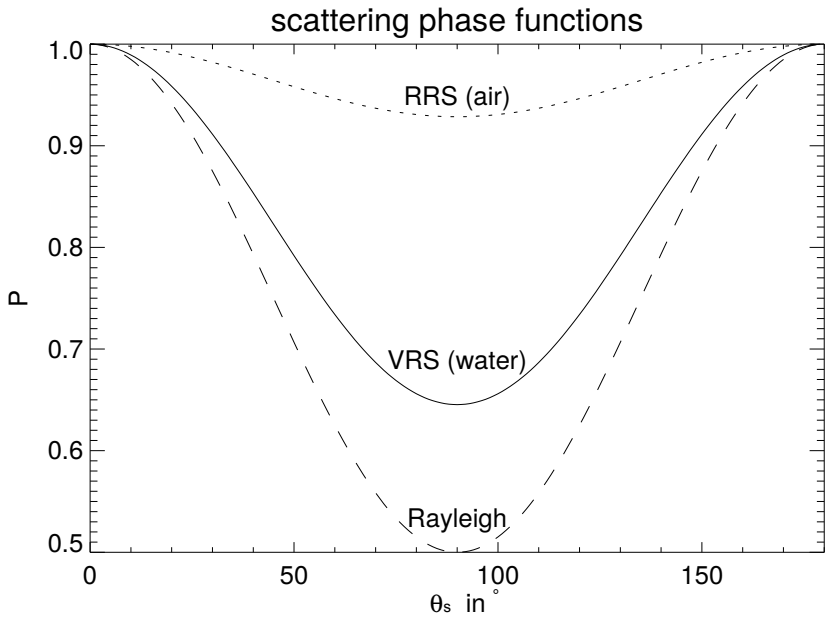

Figure 1.1: Qualitative comparison of scattering phase functions of vibrational Raman scattering in water (labeled VRS, solid line), elastic clear water scattering (labeled Rayleigh, dashed line) and rotational Raman scattering of at atmospheric Oxygen and Nitrogen molecules (labeled RRS, dotted line) for average depolarization values. The phase functions are normalized to their maximum value. Note that the ordinate axis (P) starts at 0.5.

do not justify the assumption of 'isotropic' Raman scattering for applications were accurate angular dependent radiation fields need to be derived. Nevertheless this simple approach can save some computation time if only interested in qualitative Raman contributions to irradiations, and therefore is additionally implemented as option in our model.

1.3.4 Raman Depolarization Ratio

The linear Raman depolarization ratio ρ in equation 1.11 is a measure for the linear depolarization of radiation in the Raman scattering process. It is defined as the ratio of backscattered radiation that is polarized perpendicular to the incoming radiation from a linear polarized light source and backscattered radiation that is polarized parallel to the source ($\rho := I_{\perp}/I_{||}$). The value can theoretically be directly derived from the components of the polarizability tensor of the scattering molecules. Due to the finite relaxation time of ions and electrons in the molecule after a displacement, the polarizability of the water molecules is spectrally dependent when the field inducing the dipole in the molecule is an electromagnetic wave with a sufficiently high frequency, as e.g. visible radiation. The works of Chang & Young [17] on sea water temperature measurements from Raman spectra include a detailed study and discussion of the spectral and temperature dependence of the Raman depolarization factor. They speculate that in ordinary seawater with temperatures

i	α_i	$\delta\tilde{\nu}_i(cm^{-1})$	$\delta\tilde{\nu}_i(cm^{-1})$	$\sigma_i(cm^{-1})$	$\sigma_i(cm^{-1})$
1	0.41	3250	(3225)	89.179	(95.549)
2	0.39	3425	(3425)	74.317	(74.316)
3	0.1	3530	(3520)	59.453	(63.699)
4	0.1	3625	(3612)	59.453	(63.699)

Table 1.1: Parameters of the Gaussian components of the Raman spectral redistribution function for $25°C$ ($10°C$) taken from [127] ([126]). The width parameter σ where derived from the published $FWHM$ (Full Width Half Maximum) values with the relation $\sigma = FWHM/(2\sqrt{2\ln 2})$. For a graphic representation see figure 1.2.

below $40°C$, in the underlying water mixture model concept, none or a maximum of one hydrogen bond of the four possible hydrogen bonds of every water molecule is broken by thermal energy, leading to two spectroscopically distinct types of coordination of the water molecules, -one with both hydrogen atoms bonded by hydrogen bonds and one with a free O-H. Both have different vibrational frequencies due to the different total bonding energies resulting in different Raman shifts. Due to the dependence of the bond breaking on the thermal energy, the ratio between both species is temperature dependent. Furthermore, only the lines caused by symmetric vibrations of the two O-H bonds of one molecule are non-depolarizing ($\rho < 0.25$), whereas all other Raman lines are depolarizing [17]. These mentioned effects explain why the contour of the Raman spectrum (and the corresponding depolarization ratio), being the sum of various temperature dependent Raman lines with different depolarization ratios, is itself temperature and wavelength dependent. A classification and component wise assignment of the different contributing Raman lines based on their origin (mode) and properties has e.g. been performed by Murphy and Bernstein [79]. Chang & Youngs measurements showed a temperature dependence of the linear Raman depolarization ratio of approximately 1.2% (1.7% for circular polarization) per $°C$ and a spectral variation of the value of ρ from less than 0.1 to about 0.3 in the main region of the Raman contour from 3000 to $3700cm^{-1}$ [17, 33]. Nevertheless, a fixed value of $\rho = 0.17$, supposedly sufficiently representing the true value in the spectral region of the maximum Raman emission around $3400cm^{-1}$, is generally used in RT models (e.g. [73, 105, 63, 98]). Both Tukhvatullin et al. [118] and Bray et al. [9] have recently published measurements that show in detail the steep increase (between the first and the second mode in figure 1.2) of ρ when moving from lower to higher frequencies in the Raman spectrum. While the average of Bray et al. [9] is close to the established value with $\rho = 0.156 \pm 0.004$, Tukhvatullin et al. [118] measured a comparable spectral slope but a significantly greater absolute value.

1.3.5 Spectral Redistribution by Raman Scattering

Not the spectral contours by Murphy & Bernstein mentioned in 1.3.4, but G. E. Walrafens measured Raman spectral contours of pure H_2O at $25°C$, excited by a mercury lamp at

435.8nm and numerically decomposed into four Gaussian components [126, 127], are the basis for the spectral redistribution function in many RT models that include ocean Raman scattering [67, 42, 132, 105] (see figure 1.2 and table 1.1). The measurements had been carried out at different temperatures from 10°C to 90°C, however the values at 25°C seem to be those most often used in RT models, neglecting the temperature dependence when simulating water bodies at lower or higher temperatures.

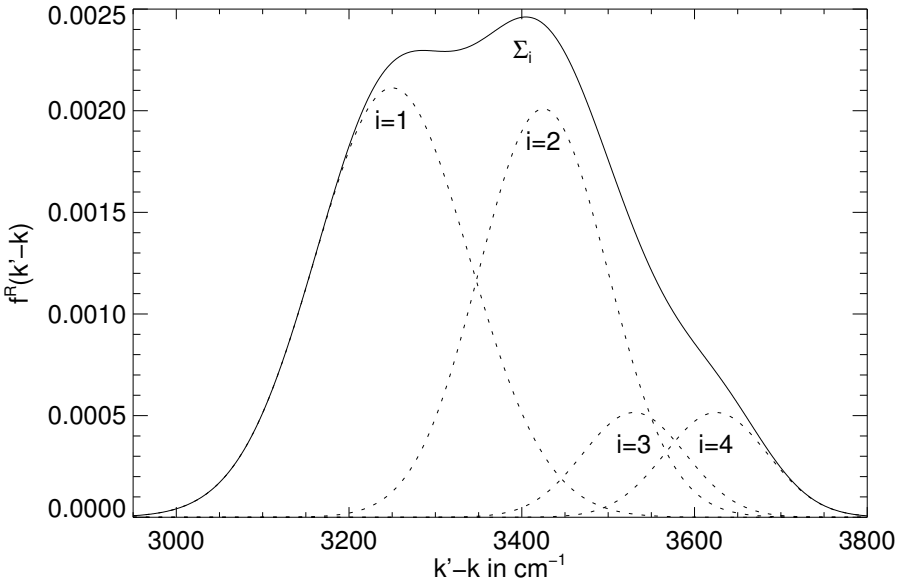

Figure 1.2: Spectral Raman shifts in wavenumbers $k' - k$ as determined by Walrafen [127] in water at 25°C and the Gaussian decomposition into four components (see table 1.1). The contour is given by $f^R(k', k) = (2\pi)^{-1/2} \left(\sum_{i=1}^{4} \alpha_i \sigma_i\right)^{-1} \sum_{i=1}^{4} \exp\left(k' - k - \delta\tilde{\nu}_i\right)^2 / 2\sigma_i^2\right)$ with the parameters from table 1.1.

Assuming that the spectra and spectral shifts are independent of the the excitational wavenumber k' throughout the spectral region of interest (UV/VIS/SWIR), the spectral response function transformed from wavenumbers ($[k] = cm^{-1}$) to wavelength dependence ($[\lambda] = nm$) has the following form, if the distribution parameters are supplied in the units as printed in table 1.1 [105]:

$$f^R(\lambda', \lambda) = \frac{10^7}{\lambda'^2} \frac{1}{(2\pi)^{1/2} \sum_{i=1}^{4} \alpha_i \sigma_i} \sum_{i=1}^{4} \exp\left(-\frac{(10^7(\lambda'^{-1} - \lambda^{-1}) - \delta\tilde{\nu}_i)^2}{2\sigma_i^2}\right) \tag{1.12}$$

for $\lambda' \leq \lambda$, and $f^R = 0$ otherwise. Function 1.12 satisfies the normalization condition $\int f^R(\lambda', \lambda) d\lambda' = 1$, and therefore can be seen as a weighting function, when spectrally integrating the Raman scattering contribution to a specific observation wavelength λ. The function broadens with decreasing peak values as λ' increases (see figure 2.3).

1.3.6 Integrated Raman Scattering Coefficient

The overall energy that is absorbed at the excitational wavelength and then re-emitted in a band centered at a longer wavelength is described by the Raman scattering coefficient b^R. Most published values of b^R are based on integrated measurements of the Raman band centered at $\Delta k = 3400 cm^{-1}$ which was excited with monochromatic radiation at $488nm$. A summary of the strong variation in the values retrieved from those measurements in the 1970's and 1980's can be found in Marshall & Smith[63]. The comparably low values obtained by Marshall & Smith ($2.6 \times 10^{-4} m^{-1}$ for computations in energy units) were later confirmed by the measurements of Bartlett *et al.*, which determined $b^R(\lambda'_0 = 488nm) = (2.7 \pm 0.2) \times 10^{-4} m^{-1}$ for pure water and seawater at room temperature [6]. However, a later publication has questioned these values by interpreting them as having been determined for photon count units rather than energy units, which would result in a slightly lower value of $2.4 \times 10^{-4} m^{-1}$ [20, 9]. To our knowledge all of the three latter values are in use in contemporary RT models. Bray et al. [9] have recently published measurements of an even lower integrated value of $b^R(\lambda'_0 = 532nm) = (1.84 \pm 0.03) \times 10^{-4} m^{-1}$ (for photon counts).

Some band based models simply allow to estimate Raman scattering effects by transferring the radiation fraction defined by b^R from a single excitation band to a single emission band, without regarding for the spectral shape f^R of the redistribution. Due to the width of f^R from about 10 to over $30nm$ in the visible (figure 2.3), this can only be recommended for applications were unweighted band averaging over similar ranges is sufficiently accurate. For these cases MOMO alternatively also allows this computation time efficient operation mode.

1.3.7 Spectral Dependence of the Raman Scattering Coefficient

The wavelength dependency of Raman absorption in water is assumed to follow a power law:

$$b^R(\lambda') = b^R(\lambda'_0) \left(\frac{\lambda'_0}{\lambda'} \right)^n . \tag{1.13}$$

While prior to the closer investigations of Bartlett *et al.*, theoretical considerations had lead to the use of both $n = 4$ (e.g. [132, 25]) and $n = 5$ (e.g. [33, 114]) values for the spectral dependency of the cross sections depending on either emission λ or incident wavelength λ', they empirically determined more precise exponent values of $n = 5.5 \pm 0.4$ for λ' and $n = 4.8 \pm 0.4$ for λ when normalized to energy units (rather than photon counts)[6].

1.3.8 Raman Scattering Entanglement with Water Absorption

The clear water absorption coefficients derived from the sea water extinction measurements of Smith & Baker (1981) [109] used to be popular as a basis for the ocean models in many RT models. These absorption coefficients can be assumed to also contain the fraction of

extinction by inelastic scattering because the measurements were carried out with a spectroradiometer at each observation wavelength. Therefore the effect of Raman scattering can be treated as a new source of radiation when the latter absorption coefficients are used (as e.g. done in Mobley et al. [73]). If using these coefficients in a model that treats only elastic scattering, effects of Raman scattering are partially (but not quantitatively) included in form of a "pseudo" absorber. For the more recent, and nowadays more popular absorption coefficients derived from ICAM (integrating cavity absorption meter) laboratory measurements by Pope & Fry (1997) [87], the situation is more complicated. In their setup a Xenon arc lamp and a monochromator is used to produce monochromatic input radiation whereas the radiation output of the water sample is measured with a broadband photomultiplier. The fraction of the Raman scattered radiation already included in the derived absorption coefficients may therefore also depend on the spectral properties of the involved components of the setup, especially on the difference in sensitivity of the photomultiplier (a *Burle 4840*) at the input and the shifted Raman emission wavelength. To our knowledge this issue has lead to different ways of treating Raman scattering in existing RT models, either as a new source of radiation, or as a scattering process, when using the coefficients of Pope & Fry, while the most accurate approach may be somewhere in between. This issue with the literature values of the water absorption coefficient (a_{lit}) can be summarized as follows:

$$a_{H_2O} \leq a_{lit} \leq a_{H_2O} + b^R \Leftrightarrow a_{lit} = a_{H_2O} + \gamma b^R \text{ with } 0 \leq \gamma \leq 1, \tag{1.14}$$

where the determination of the setup dependent factor γ is the remaining question. It must be pointed out that the differences in the output between the two mentioned model approaches mainly affects the spectral region around the minimum of the water absorption coefficients at approximately $420nm$, where the difference of the water absorption coefficient and the Raman scattering coefficient is smallest. Future absorption measurements with a comparable setup could avoid this ambiguity by detecting only output radiation of the input wavelength, e.g. by the use of an additional monochromator or a spectrometer. It shall be noted that phenomenological bio-optical models, as introduced in section 3.2.4, may as well be subject to an inclusion of effects of radiation redistributed by Raman scattering.

1.3.9 Polarization by Vibrational Raman Scattering

The negligence of the polarization state in scalar radiative transfer computations is known to be a source of inaccuracy, even when purely interested in the intensity values [44, 48]. The main scope of this thesis was the development, validation and application of a radiative transfer model including the effects of vibrational Raman scattering in the water on the basis of the existing scalar RT model MOMO. The term *scalar* is used to distinguish it from *vector* radiative transfer models, which compute a vector describing the intensity and the polarization of radiation rather than solely the scalar intensity. Nevertheless, due to the advanced and ongoing efforts in our research group to transfer the approach to the vector

version of the MOMO code implemented by Hollstein and Fischer [44] and to validate it, a brief introduction of the additional required information regarding the polarization properties of Raman scattering is given.

In vector radiative transfer it is popular to describe the state of radiation in terms of the Stokes parameters I, Q, U and V. While I resembles the scalar radiation intensity, Q, U and V determine the so called polarization ellipse. While Q and U are associated to the linear components of the polarization state, V contains information about the circular component. If combined into a vector, these parameters form the so called *Stokes vector* $\vec{S}$:

$$\vec{S} := \begin{pmatrix} I \\ Q \\ U \\ V \end{pmatrix}. \tag{1.15}$$

The alteration of incident radiation $\vec{S'}$ by interaction with an optical element can be described by the $4X4$ so called *Müller-Matrix* $\mathbf{M}$:

$$\vec{S} = \mathbf{M}\vec{S'}. \tag{1.16}$$

The discussion of the Raman depolarization ratio in section 1.3.4 implied that vibrational Raman scattering has an influence on the polarization state of the scattered radiation. The Raman scattering phase-function therefore has to be extended to a scattering matrix, being the Müller-Matrix of Raman scattering $\mathbf{M}^R$, when incorporating Raman scattering into a vector radiative transfer model. In analogy to the phase function, $\mathbf{M}^R$ depends on the molecular polarizability. From theoretical considerations (see e.g. Xu [131] and Bohren and Huffman [8] for details) the Raman phase matrix $\mathbf{M}^R = \tilde{a}\tilde{\mathbf{M}}^R$ can be derived from the polarizability tensor[2] and separated into a scattering angle independent prefactor $\tilde{a}$ and a scattering angle dependent Matrix $\tilde{\mathbf{M}}^R$ [131]:

$$\tilde{\mathbf{M}}^R = \begin{pmatrix} \frac{3+9\rho+3(1-\rho)\cos^2\theta_s}{6-8\rho} & \frac{3(1-\rho)}{6-8\rho}(\cos^2\theta_s - 1) & 0 & 0 \\ \frac{3(1-\rho)}{6-8\rho}(\cos^2\theta_s - 1) & \frac{3(1-\rho)}{6-8\rho}(\cos^2\theta_s + 1) & 0 & 0 \\ 0 & 0 & \frac{3(1-\rho)}{3-4\rho}\cos\theta_s & 0 \\ 0 & 0 & 0 & \frac{3(1-3\rho)}{3-4\rho}\cos\theta_s \end{pmatrix}, \tag{1.17}$$

where once again θ_s is the scattering angle and ρ the Raman depolarization ratio.

When implementing vector Raman scattering in an RT model, the applicability of the standard Raman spectral redistribution function discussed in 1.3.5 needs to be carefully evaluated. A model with a more explicit assignment of depolarization properties to each mode may be beneficial (also see discussion in section 1.3.4 and 1.3.5).

[2] More precisely, for vibrational Raman scattering the Phase matrix is derived from the so called *derived polarizability tensor*, which specifies the dependence of the tensor elements on the vibration frequency and phase [131].

1.4 Fluorescence in the Ocean

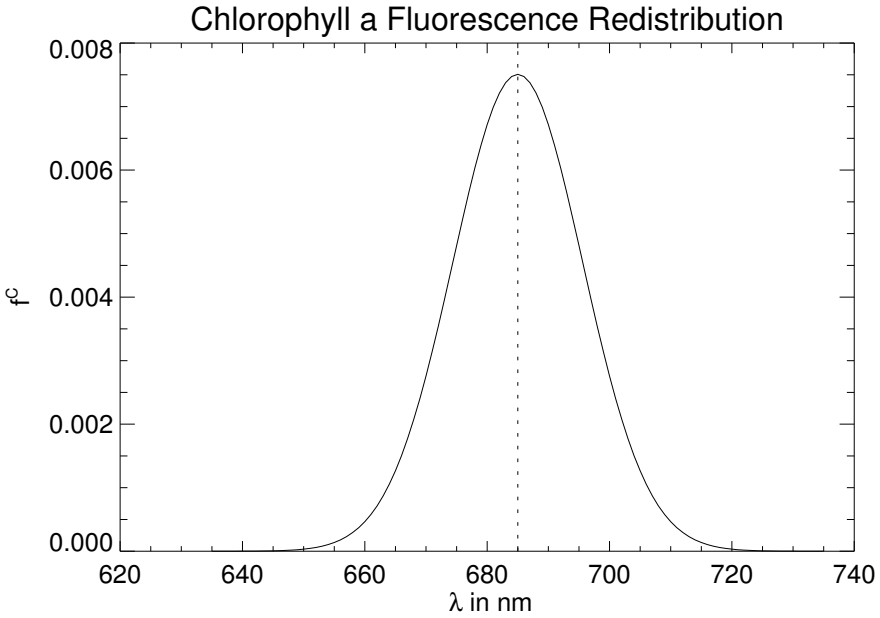

Figure 1.3: Spectral redistribution function of Chlorophyll *a* fluorescence f^C.

Another source of inelastic scattered radiation in the ocean is the fluorescence of chlorophyll and yellow substance, which shall therefore be introduced here briefly for the sake of completeness. In contrast to vibrational water Raman scattering the emission is limited to a fixed band which does not depend on the excitation wavelength. These sources are also a fraction of J^I (equation 1.6) in the water and thus may also be expressed as:

$$J^X(\mu,\varphi,\lambda) = \frac{1}{c(\lambda)} \int_{\Lambda'} \int_{\Omega'} \tilde{\beta}^X(\mu',\mu,\phi',\phi,\lambda',\lambda) L'(\mu',\phi',\lambda') d\Omega' d\lambda' \tag{1.18a}$$

$$+ \frac{1}{c(\lambda)} \int_{\Lambda'} \tilde{\beta}^X(\mu'^\circ,\mu,\phi'^\circ,\phi,\lambda',\lambda) E'^\circ(\mu'^\circ,\lambda') d\lambda'. \tag{1.18b}$$

where ^{X} may be replaced either by ^{C} for chlorophyll or ^{Y} for yellow substance. The optical properties of Fluorescence, however, allow to significantly simplify equation 1.18 and the components of $\tilde{\beta}^X$ in comparison to vibrational clear water Raman scattering (equation 1.8 and following).

Fluorescence of dissolved organic matter may be assumed to be isotropic. While in general the latter is not necessarily the case for fluorescence of particles [51], laboratory measurements with phytoplankton particles have proven this assumption to be sufficient for many applications [26, 72]. This leaves an angle independent phase function of:

$$P^X = (4\pi)^{-1}, \tag{1.19}$$

with $\left[P^X\right] = sr^{-1}$. Therefore $\tilde{\beta}^X$ is only wavelength and not angle dependent and the angular integration of the incident radiance in equation 1.18 can be replaced by the scalar irradiance E'_0, because:

$$E'_0 := \int_{\Omega'} L'(\mu', \phi', \lambda') d\Omega'. \tag{1.20}$$

If the sum of the diffuse scalar irradiance and the direct solar irradiance is defined to be $\tilde{E'}_0$, then equation 1.18 can be reduced to:

$$J^X(\lambda) = \frac{1}{4\pi c(\lambda)} \int_{\Lambda' X} \tilde{\beta}^X(\lambda', \lambda) \tilde{E'}_0(\lambda') d\lambda'. \tag{1.21}$$

The spectral properties of the fluorescence signal allow some additional simplifications in comparison to Raman scattering. In a similar approach as in equation 1.8, $\tilde{\beta}^X$ may be separated into a fluorescence scattering coefficient b^X and a spectral redistribution function f^X:

$$\tilde{\beta}^X(\lambda', \lambda) = b^X(\lambda', \lambda) f^X(\lambda). \tag{1.22}$$

The fluorescence scattering coefficient is the product of the absorption coefficient $a^X(\lambda')$ of the fluorescent matter and an efficiency function describing the fraction of available radiation that is inelastically scattered to the emission band. As for instance in Fell [26] as well as Schroeder et al. [105], the latter is often given as a quantum efficiency $\Phi^X(\lambda')$ in terms of photon counts, which needs to be corrected for by a factor of λ'/λ in an energy based frame of reference, leading to:

$$b^X(\lambda', \lambda) = a^X(\lambda') \Phi^X(\lambda') \frac{\lambda'}{\lambda}. \tag{1.23}$$

The determination of the dependence of $a^X(\lambda')$ on the concentration of yellow substance, phytoplankton etc. is a duty of a bio-optical model, as is described in section 3.2.4.

A short discussion of the evolution of measurements of the quantum efficiency values can be found e.g. in Schroeder et al. [105]. Summarizing the latter, an overview of Mobley [72] (based on the works of Hawes et al. [43], Kiefer and Reynolds [54] and Kiefer et al. [53]) concludes $\Phi^C \in [0.01, 0.1]$ and $\Phi^Y \in [0.005, 0.015]$, while Fischer et al. [29] and Doerffer and Fischer [21] found $\Phi^C \approx 0.03$ for the the North Sea. While the assumption of a wavelength independent quantum efficiency value for chlorophyll fluorescence throughout the contribution excitation band $\Lambda'^C = [370nm, 690nm]$ is generally considered to be valid, the consideration of a wavelength dependence for yellow substance fluorescence throughout the excitation band Λ'^Y in the UV may be required (see e.g.[105, 40, 18]).

The spectral redistribution function $f^X(\lambda)$ (with $[f^X] = nm^{-1}$) describing the emission spectrum, in contrast to to $f^R(\lambda', \lambda)$, depends only on the emission wavelength and follows the normalization condition:

$$\int_{\Lambda^X} f^X(\lambda) d\lambda = 1. \tag{1.24}$$

For chlorophyll a fluorescence, f^C can be approximated by a single mode Gaussian distribution function [26, 34]:

$$f^C(\lambda) = \frac{1}{4\pi\sigma^C} \exp\left(-\frac{(\lambda - \lambda_0^C)^2}{2(\sigma^X)^2}\right). \tag{1.25}$$

In contrast to clear water VRS, the radiation from the whole contributing wavelength range Λ^C is shifted to a fixed emission band centered at λ_0^X. For chlorophyll fluorescence this center is approximately at $\lambda^C = 685nm$ and the distribution width parameter is $\sigma^C = 10.6nm$ [26], -the according redistribution function is shown in figure 1.3. For spectral redistribution of yellow substance, it may be referred to e.g. Traganza [117].

It is common to separate the excitation and emission wavelength dependence in equation 1.21, which, under the assumption of a spectral independent Φ^X, yields [26, 105]:

$$J^X(\lambda) = \frac{f^X(\lambda)\Phi^X}{\lambda 4\pi c(\lambda)} A^X, \tag{1.26}$$

where A^X is given by:

$$A^X := \int_{\Lambda' X} a^X(\lambda')\lambda' E_0'(\lambda') d\lambda'. \tag{1.27}$$

1.5 Rotational Raman Scattering by Atmospheric Molecules

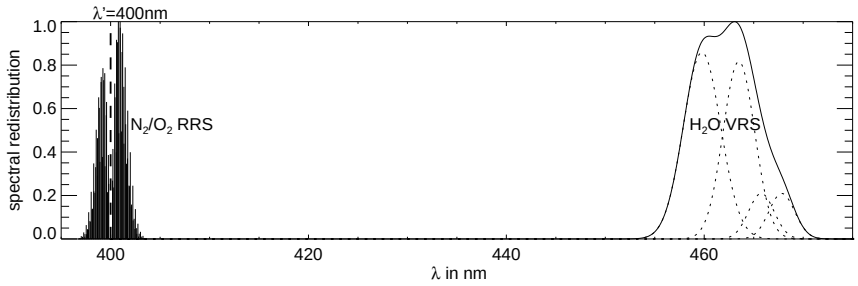

Figure 1.4: The rotational Raman cross sections of the airs Oxygen and Nitrogen molecules in comparison to the spectral redistribution function for vibrational liquid water Raman scattering for monochromatic excitation at $\lambda' = 400nm$. All three spectra have been normalized to their maximum.

While not reaching the maximum total magnitude of vibrational ocean Raman scattering in terms of Raman scattered radiation fraction owing, i.a., to the comparably limited spectral shifts, the consideration of the effect of rotational Raman scattering may be of significance for applications that rely on an accurate simulation of small scale spectral features. This i.a. includes the remote sensing of some atmospheric trace gases and vegetation fluorescence. While having chosen the contribution by ocean Raman scattering as the principal topic of this thesis, the RT model version developed within the thesis is

specifically designed to additionally allow the inclusion of other inelastic scattering sources. Therefore, we plan to provide an RT model that includes all major contributions of inelastic scattering in the near future. The initial efforts in terms of atmospheric contributions included the implementation of a preprocessor for the computation of the scattering cross sections of atmospheric rotational molecular Raman scattering by the author of this thesis. The latter is the basis for the rotational Raman source computation (equation 1.28) and model integration in the future. A brief overview of the steps involved will be given here for the sake of completeness.

The filling of solar spectral Fraunhofer lines and atmospheric absorption lines in observed radiances by atmospheric interaction is known as the Ring effect, named after one of its discoverers [38]. While a number of different inelastic atmospheric scattering processes have been identified as contributors (see e.g. [15], [133] and [50]), the contribution by rotational Raman scattering alone has proven to account for the bulk of the effect in the UV and visible spectral range [50]. The vibrational Raman spectrum of atmospheric molecules is generally not considered as part of the ring effect, due its greater spectral shifts and smaller cross sections. However, having been thought to be negligible for most applications, the magnitude of the effect of *Fraunhofer Ghost lines* (FGL) originating from the latter has recently been found to justify its consideration for the remote sensing of weak absorbers [59].

Rotational Raman scattering adds to the inelastic fraction in equation 1.6 and its source term can likewise be formulated as:

$$J^{rr}(\mu,\phi,\lambda) = \frac{1}{c(\lambda)} \int\int_{\Omega'} \tilde{\beta}^{rr}(\mu',\mu,\phi',\phi,\lambda',\lambda) L'(\mu',\phi',\lambda') d\Omega' d\lambda' \tag{1.28a}$$

$$+ \frac{1}{c(\lambda)} \int_{\Lambda'} \tilde{\beta}^{rr}(\mu'^{\circ},\mu,\phi'^{\circ},\phi,\lambda',\lambda) E'^{\circ}(\mu'^{\circ},\lambda') d\lambda'. \tag{1.28b}$$

$\tilde{\beta}^{rr}$ can be considered as the product of rotational Raman phase function P^{rr}, an altitude dependent molecule density N and the scattering cross section σ^{rr}:

$$\tilde{\beta}^{rr}(\mu',\mu,\phi',\phi,\lambda',\lambda,z) = P^{rr}(\mu',\mu,\phi',\phi) N(z) \sigma^{rr}(\lambda',\lambda). \tag{1.29}$$

Due to the dominance of molecular nitrogen ($\approx 78\ vol\%$) and oxygen ($\approx 21\ vol\%$) in the Earth's atmosphere, the approximation of β^{rr} for these two species is introduced in the following. Hereby the principals found in Kylling et al. [58], Landgraf et al. [60] and Chance and Spurr [15] are followed, with emphasis on the results rather then the details of molecular spectroscopy. Furthermore, the focus shall be on the position and intensity of all contributing modes while the actual linewidths and there temperature and pressure dependence will not be discussed here.

The Phase function has the same basic symmetry as the one for elastic Rayleigh scattering, but with a less pronounced angular dependence (see figure 1.1), and is given by [110]:

$$P^{rr}(\theta_s) = \frac{3}{40}(13 + \cos^2\theta_s), \tag{1.30}$$

where the prefactors depend on the chosen normalization condition. The scattering angle θ_s can be derived from μ', μ, ϕ' and ϕ with equation 1.10. The rotational Raman scattering cross section for a molecule, that can be approximated with sufficient accuracy to be linear, is given by [15, 110]:

$$\sigma^{rr}(\lambda_i, \lambda_s) = \frac{256\pi^5}{27} F_J(T)\gamma^2(\lambda_i)\frac{C_{J,J'}}{\lambda_s^4}. \tag{1.31}$$

Due to historical reasons and in contrast to the formalism of vibrational Raman scattering in this thesis, values of the final state and not the initial state are denoted with an apostrophe ($'$) in equation 1.31 and in the following description in this section. To not confuse the excitation and emission wavelengths, we therefore refer to the incident (excitation) wavelength as λ_i and the scattered (emission) wavelength as λ_s in equation 1.31 and the rest of this section.

The polarizability anisotropy of both molecules is given by [58, 15]:

$$\gamma_{O_2} = 7.149 \cdot 10^{-26} cm^3 + \frac{4.5936 \cdot 10^{-15} cm}{4.82716 \cdot 10^9 - k_i^2}, [k_i] = cm^{-1}, \tag{1.32a}$$

$$\gamma_{N_2} = 6.01466 \cdot 10^{-25} cm^3 + \frac{2.38557 \cdot 10^{-14} cm}{1.86099 \cdot 10^{10} - k_i^2}, [k_i] = cm^{-1}, \tag{1.32b}$$

where k_i is the wavenumber of λ_i.

The wavelength shifts for a transition from the angular quantum number J to J' are [110]:

$$\Delta\lambda_{J,J'} = \frac{\lambda}{1 + \lambda\frac{\Delta E_{J,J'}}{hc}}. \tag{1.33}$$

The shifts for rotational energy $\Delta E_{J,J'} = E_{J'} - E_J$ can be determined by [47]:

$$E_J = J(J+1)hcB_0, \tag{1.34}$$

where c is the speed of light, h is the Planck constant, $B_0(O_2) = 1.4378 cm^{-1}$ and $B_0(N_2) = 1.9897 cm^{-1}$.

The fraction of molecules that are in the initial state for a temperature T is approximated by [60]:

$$F_J(T) = \frac{g_{N,J}}{Z}(2J+1)\exp\left(-E_J/kT\right), \tag{1.35}$$

where the statistical weights are given by $g_N(O_2, J_{even}) = 0$, $g_N(O_2, J_{odd}) = 1$, $g_N(N_2, J_{even}) = 6$ and $g_N(N_2, J_{odd}) = 3$. The state sum Z can be determined by applying the normalization condition $\sum_J F_J = 1$.

The so called Placzek-Teller-Coefficients for a linear molecule with electronic spin $S = 0$ are [15]:

$$C_{J,J+2} = \frac{3(J+1)(J+2)}{2(2J+1)(2J+3)} \tag{1.36}$$

for the Stokes lines and:

$$C_{J,J-2} = \frac{3J(J-1)}{2(2J+1)(2J-1)} \tag{1.37}$$

for the anti-Stokes lines.

The latter are not strictly valid for oxygen with $S = 1$, are however often used [58]. A more precise treatment is discussed in [15].

Figure 1.4 shows the relative line strengths and distribution, computed with the method above, for monochromatic excitation at $400nm$. In comparison to the large shift introduced by liquid water VRS, the RRS spectrum features a great number of distinct lines on both sides of the excitation wavelength, though in a much smaller wavelength range.

When incorporating the cross sections computed with the method introduced above into the RRS source term, the spectral integrations in equation 1.28 can be replaced by a summation over all contributing lines [110].

Chapter 2

Raman Scattering in a Numeric Radiative Transfer Model

2.1 Introduction

Analytical solutions of the radiative transfer equation are only known for simple canonical problems and therefore numeric solution are required for its application to complex and realistic problems. With the rapid increase of available computation power for scientific applications in the second half of the twentieth century and in the past years a variety of numerical radiative transfer computation methods, which are based on concepts of radiative transfer theory developed in the first half of the century (e.g. by Schwarzschild [106] and Chandrasekhar [16]), have been implemented for the ocean-atmosphere system by different groups. To name just a few: Tanaka [115], Gordon et al. [36], Morel and Gentili [77], Mobley [70], Frank Fell and Jürgen Fischer [31], Zhai et al. [134] and Rozanov et al. [102]). A widespread method is the photon distribution tracking in *Monte Carlo* (MC) models, which are best suited for the simulation of optically thin media due to the manageable amount of photons required for accurate simulations of such cases (see e.g. Plass and Kattawar [84]). The ocean model of Mobley [67] featured in our validation efforts is based on the approach of so called *Invariant Embedding* and has in our trial runs proven to only become very slow in strongly absorbing optically thick media. *Successive Orders of Scattering* models on the other hand are fast only in strongly absorbing media were the consideration of a small amount of successive scattering events is sufficient. Another method popular for the atmosphere treatment is the *Discrete-ordinate* approach, based on the theoretical considerations of Chandrasekhar [16] (also see [111] and Spurr et al. [110]), while several approximation models of hydrologic optics feature the *two-stream* approach (see e.g. Haltrin and Kattawar [42], Khalturin [52] and Preisendorfer and Mobley [90]). Finally, the *Matrix-Operator* approach offers a very efficient way of performing radiative transfer computations in optically thick media (see e.g. Plass et al. [85]). All of the discussed approaches are based on the phenomenological description of inherent optical properties of the medium in form of e.g. absorption and volume scattering coefficients. While the

latter may generally be inferred from phenomenological or theoretical considerations, most commonly it is done from a mixture of both. In contrast to the latter, e.g. Acquista and Anderson [1] have presented a method to directly use quantum-electrodynamics theory as basis of for the radiative transfer computations.

More or less quantitative inclusions of the effect of water Raman scattering have been performed for radiative transfer models in the past decades. Among them are especially the MC models, but also some other approaches, including rough analytical approximations and an azimuthally averaged Matrix-Operator approach (see i.a. [73, 63, 132, 35, 104, 129, 105]). However, we have identified a lack of available models that combine a quantitative treatment of Raman scattering with all the other features that a multipurpose RT model for the field of Remote sensing could be expected to have. This "wish list" includes:

1. The quantitative and accurate simulation of daylight induced radiation fields of the combined atmosphere-ocean system in a high spectral and angular resolution,

2. the applicability of the model to real world cases including the effects of atmospheric absorption and the wind speed effect on the sea-surface,

3. the successful validation of the model output,

4. a sufficient execution speed for the use in forward models and for the generation of extensive lookup tables in optically thick and thin media,

5. an execution stability sufficient for the use in operational algorithms,

6. the possibility to account for polarization effects,

7. and an inclusion of ocean Raman- (and possibly other inelastic-) scattering effects in their full angular and spectral resolution in a computation time efficient manner.

Due to the rapid increase of available computation power, some of the previously existing limitations have become solvable in the past decade. While our existing RT model MOMO (see Frank Fell and Jürgen Fischer [31]) already satisfied the first five items, the sixth item had been addressed by Hollstein and Fischer [44] recently within our group. This thesis shall be about the successful efforts to add the capabilities mentioned in item seven to our model.

In the following we present our approach to quantitatively integrate vibrational Raman scattering sources, on the basis of the optical properties discussed in chapter 1, into a Matrix-Operator radiative transfer model of the coupled atmosphere-ocean system. This includes an efficient method developed for the determination of the excitation band contributions including the accurate spectral and azimuthal dependence and a new approach for the fast and accurate treatment of the depth dependency of the Raman source within homogeneous layers. While others in our research group have incorporated the effect of longwave emission into the featured RT model MOMO (see Doppler et al. [22]), this work focuses on the spectral region of daylight in the UV and visible spectral range.

2.2 The Matrix-Operator Model MOMO

The matrix-operator method is a very efficient approach to compute radiative transfer in plane parallel, but optically thick media. Based on the works of Hulst [46] and Twomey et al. [119], among others, a first extensive description of the method can be found in [85], although some of the principles had already been mentioned by Stokes [112] in the 19th century. MOMO (Matrix-Operator MOdel) is a Fortran-code package that has been developed and constantly improved and extended in it's capabilities in the past decades at our institute. The initial azimuthally dependent code for the atmosphere-ocean system was developed by Fischer and Grassl [28]. Later iterations of the code, additionally including the wind roughened sea surface [27], were presented by Fell [26] and Frank Fell and Jürgen Fischer [31]. Recently the code was upgraded to support polarization by Hollstein and Fischer [44] and longwave emission by Doppler et al. [22].

The upgraded MOMO code version that we discuss here allows to integrate arbitrary new radiation sources at any vertical position of the model, as for example the emission of Raman scattered light. The following sections describe the way this new algorithm, based on the existing matrix-operator model MOMO, accounts for water Raman scattering effects, accompanied by an overview of the essential underlying techniques. While all the mathematical details of the matrix-operator method in general can be found in [85], a description of the implementation in the prior MOMO version, excluding inelastic scattering effects, can be found in [31]. Therefore the description of the new algorithm (sections 2.6, 2.7, 2.9, 2.11 and 2.12) shall only be complemented by a summary of those steps and equations used in the underlying and pre-existing elastic scattering model version, following the principles from the latter mentioned publications, that are believed to be mandatory as basis for the understanding of the approach for the inclusion of inelastic scattering effects (sections 2.3 to 2.5, 2.8 and 2.10).

2.3 Radiation at the Model Layer Boundaries

In matrix-operator models, the propagating medium (in our case the atmosphere-ocean system) is represented by an appropriate number of distinct homogeneous layers, with the boundary positions (measured from the top of the uppermost layer) denoted as τ_n in optical depth units and z_n for the geometrical height. The so called interaction principle underlies the computation of the light-field at the layer boundaries. The latter linearly relates outward directed radiation at the layer boundaries to the incoming radiation at the boundaries and the radiation generated within the layer as initially described in the 1960s by Redheffer [96] and a.o. Grant and Hunt [39]. The linearity assumption is generally valid for the order of magnitude of the solar shortwave radiation reaching the earth and its terrestrial interactions. It is common to distinguish between downward (labeled with a "+") and upward (labeled with a "−") directed radiation and to express the proportionality constants of the relation in (e.g. the matrix-form of) so called reflection-($\mathbf{R}$) and transmission-operators ($\mathbf{T}$), following there function, and the offset describing the radia-

tion generated within the layer in the form of a so called source-operator ($\mathbf{J}$). For instance, the upward directed diffuse radiation at the upper boundary of an arbitrarily vertically structured layer (with its upper border at τ_0 and its lower border at τ_1) depends on the latter mentioned operators and the incoming radiation the following way:

$$\mathbf{L}_0^- = \mathbf{R}_{01}\mathbf{L}'^+_0 + \mathbf{T}_{10}\mathbf{L}'^-_1 + \mathbf{J}^-_{10}. \tag{2.1}$$

This example shall also illustrate our notation. The indices 0 and 1 denote the position of a layer boundary, starting with zero at the uppermost boundary. Therefore every matrix operator of a distinct layer between two boundaries requires two of these indexes. If an operator describes a feature that is not necessarily symmetric regarding the up- and down-direction, the sequence of the two indexes is not arbitrary, which is shown by an extra sign label (+ or −), as e.g. for the source operator $\mathbf{J}^-_{10}$. The indexing of incoming radiation with an $'$ is not strictly required to visualize these principles when no inelastic scattering processes are involved, will however be kept in this chapter in consistence with the notation introduced in chapter 1.

We use the matrix-operator method to compute the propagation of diffuse radiation through the atmosphere and ocean layers. The fraction of direct sunlight can easily be derived separately from the optical depth at a given vertical position using Lambert-Beers law. Single scattered solar radiation is then introduced in the form of a source operator for each model layer. For simplicity the latter can be combined with all other sources in that layer, as for example Raman emission, to form a general source operator, by element-wise adding of the different source operators. The equations to compute the diffuse radiation at internal layer boundaries then have the following form, if no diffuse radiation enters the system from the top at τ_0 (which can be assumed for the atmosphere during daytime, where direct sunlight is by far the most dominant radiation source entering from above):

$$\mathbf{L}_1^- = (\mathbb{1} - \mathbf{R}_{12}\mathbf{R}_{10})^{-1}\left(\mathbf{T}_{21}\mathbf{L}'^-_2 + \mathbf{R}_{12}\mathbf{J}^+_{01} + \mathbf{J}^-_{21}\right), \tag{2.2a}$$

$$\mathbf{L}_1^+ = (\mathbb{1} - \mathbf{R}_{10}\mathbf{R}_{12})^{-1}\left(\mathbf{R}_{10}\mathbf{T}_{21}\mathbf{L}'^-_2 + \mathbf{R}_{10}\mathbf{J}^-_{21} + \mathbf{J}^+_{01}\right), \tag{2.2b}$$

where $\mathbb{1}$ is the identity matrix and the internal boundary position has the index 1 while the outer boundaries are located at 0 and 2. A description of how equations 2.2 can be inferred from 2.1 in a few steps can be found in Plass et al. [85]. For a medium represented by a number of layers, radiances obviously have to be computed starting at the bottom, since knowledge of the upwelling input radiance entering the system at τ_2 from below ($\mathbf{L}'^-_2$) is required to compute the radiation at the subsequent higher boundary at τ_1. The land surface and the bottom of the ocean are treated as non-transmitting layers, whereas the land-sea interface in MOMO allows to either model a flat surface featuring Fresnel-reflection and -transmission or to simulate a wind roughened surface based on Cox & Munks wind speed dependent Sun glitter statistics [19, 31].

The equations above show how to compute the resulting light-field from operators representing the properties of the model layers. In the following sections we will show how

these operators are accurately derived from the basic optical properties (IOPs) that are required as input to define each model layer in MOMO.

2.4 Elimination of the Azimuth Dependence

Due to symmetries in the azimuthal radiation distribution by most of the occurring scattering processes, a Fourier decomposition of the azimuthal dependence of the phase function, as is done on MOMO, can improve the computation speed. In general, the separation of azimuth- and zenith-dependence is a common approach within the matrix-operator method, however with varying types of decompositions. The RTE then splits up into a set of independent equations that depend on the solar- and observation-zenith-angle. The Fourier coefficients P_m of a scattering phase function P are given by:

$$P_m(\mu', \mu) = \nu_m^{-1} \int_{-\pi}^{\pi} P(\cos\theta_s) \cos m(\phi - \phi') d(\phi - \phi'). \tag{2.3}$$

In case of the Raman scattering phase function only three expansion coefficients need to be computed, whereas strongly peaked phase functions (e.g. of large aerosols, droplets and oceanic scatterers) may need up to over a hundred to be accurately sampled [1]. In all cases of radiation scattering in an isotropic medium, cosine coefficients are sufficient for the expansion due to the azimuthal symmetry of radiation relative to the incoming radiation. The Fourier index dependent prefactor is 2π for the index 0 and π for $m > 0$ here:

$$\nu_m = (1 + \delta_{0m})\pi, \tag{2.4}$$

following a popular normalization condition for phase functions[2]:

$$\int_0^{2\pi} \int_{-1}^{1} P^R(\cos\theta_s)\, \mathrm{d}\mu \mathrm{d}\phi = 1 \Rightarrow \int_{-1}^{1} P_0^R(\mu', \mu)\, \mathrm{d}\mu = (2\pi)^{-1}. \tag{2.5}$$

After solving the separated RTEs subsequently the resulting radiances in MOMO are being back transformed to azimuthal and zenith angle dependence in the end before they are written to the output file using:

$$L(\mu, \phi) = \sum_{m=0}^{M} L_m(\mu) \cos m\phi + \Delta(M), \tag{2.6}$$

[1] To limit the necessary amount of Fourier coefficients and therefore the computation time when strongly peaked phase functions are involved, MOMO allows to replace the narrow section of the forward scattering peak by a second order polynomial while adding the truncated fraction of energy to the direct and therefore unscattered radiation while ensuring energy conservation[31]. The underlying principle is based on the works of Potter [89].

[2] Due to historic reasons the internal normalization condition in MOMO is $\int_{-1}^{1} P_0^R(\mu', \mu)\mathrm{d}\mu = 1$ and therefore, e.g. the right side of the equations (2.13), (2.15) and (2.19) to determine the elementary source operators would have to be multiplied with ν^{-1} to reflect the actual implementation of the Raman source matrix calculation in the code.

where M is the number of expansion coefficients used and Δ is the error caused by the limitation of M. Analog, any operator with a Fourier index m in the following sections can be back transformed similarly, so for instance the back transformation of the Raman source operator J_m^R and the Radiances L^m from Fourier space to azimuthal dependence is given by:

$$J^R(\mu,\phi) = \sum_{m=0}^{3} J_m^R(\mu)\cos m\phi, \tag{2.7a}$$

$$L(\mu,\phi) = \sum_{m=0}^{M} L_m(\mu)\cos m\phi. \tag{2.7b}$$

2.5 Discretization of the Zenith Dependence

The zenith dependence is discretized in MOMO using the Gauss-Lobatto quadrature scheme [113], which allows to generate the positions μ_i and the relative weights c_i (with $\sum_{i=0}^{N} c_i = 1$) of the desired number N of (irregular) zenith grid points, while always containing the position $\mu_0 = 1$. The weights c_i allow to integrate the hemispherical diffuse vector-(E) and scalar(E_0)- irradiances from the radiances $L(\mu_i)$ by a simple summation:

$$E = \sum_{i=0}^{N} L(\mu_i) c_i \mu_i, \tag{2.8a}$$

$$E_0 = \sum_{i=0}^{N} L(\mu_i) c_i. \tag{2.8b}$$

$L(\mu_i)$ may be replaced by by the azimuthal average $L_0(\mu_i)$ in the latter formulas without changing the result, as long as the normalization of the Fourier coefficient is correctly taken into account. As is popular for radiances, the hemispherical vector irradiances may be labeled upwelling (E^-) or downwelling (E^+), corresponding to the propagation direction of the radiances, which is likewise indicated by upward- (μ_i^-) and downward-(μ_i^+) oriented zenith directions. The scalar irradiance E_0 is often considered to be the integral over the complete sphere, equaling the sum of the upwelling and downwelling hemispherical fractions.

Due to refraction at the water surface, the hemispherical radiation distribution entering the water body from the atmosphere is narrowed down to a cone. An adapted quadrature scheme is used in MOMO for the computation of the refracted zenith angles in the ocean as well as the grid of additional zenith angles to cover the areas outside the mentioned cone, that are not accessible by atmospheric radiation without scattering within the ocean [31, 49]. Where necessary, we will highlight the difference between atmospheric and oceanic zenith angles $\mu_i^{(atm)}$ and $\mu_i^{(oce)}$ and the corresponding weights $c_i^{(atm)}$ and $c_i^{(oce)}$ by the use of the flags *atm* and *oce*.

The mentioned elimination of the azimuthal dependence and the discretization of the zenith dependence allows for a matrix representation of the operators and light fields, where the rows (index i) discriminate between the zenith angles of the outgoing radiation and the columns (index j) discriminate between the zenith angles of the incident light. The phase function, for instance, can then be represented by two matrices, distinguishing between forward (labeled **T** for transmission) and backward (labeled **R** for reflection) scattering, due to the identity of the angular distances between incoming and scattered radiation:

$$\mathbf{P}_m^{\mathbf{R}} = [P_m(\mu'^{+}_j, \mu_i^{-})] = [P_m(\mu'^{-}_j, \mu_i^{+})], \tag{2.9a}$$
$$\mathbf{P}_m^{\mathbf{T}} = [P_m(\mu'^{+}_j, \mu_i^{+})] = [P_m(\mu'^{-}_j, \mu_i^{-})]. \tag{2.9b}$$

In the matrix forms of the radiation fields and the source operators, the incident radiation angle represents the solar zenith angle μ_j°:

$$\mathbf{L}_m^{-} = [L_m(\mu_j^{\circ}, \mu_i^{-})], \tag{2.10a}$$
$$\mathbf{L}_m^{+} = [L_m(\mu_j^{\circ}, \mu_i^{+})], \tag{2.10b}$$
$$\mathbf{J}_m^{-} = [J_m(\mu_j^{\circ}, \mu_i^{-})], \tag{2.10c}$$
$$\mathbf{J}_m^{+} = [J_m(\mu_j^{\circ}, \mu_i^{+})]. \tag{2.10d}$$

2.6 Discretization of the Spectral Dependence of Raman Scattering

Due to the trans-spectral nature of the Raman scattering process, some words need to be said to the technical integration of such a process into a radiative transfer model that is designed to solve monochromatic radiative transfer equations. As mentioned in section 1.2, Raman scattering can be treated as a new radiation source at the (monochromatic) observation wavelength. However, to infer the Raman source operator at λ observation wavelength, the spectral integral of the product of the volume scattering function and the excitational radiation (in equation 1.7) has to be computed over the whole contribution wavelength range of λ'. If the threshold of the spectral redistribution function f^R for the cutoff of the integration is set to e.g. $f^R(\lambda') \leq 10^{-5}$, a λ' band of approximately $10nm$ (at $\lambda = 400nm$) to $30nm$ (at $\lambda = 700nm$) width (blue-shifted by about $60nm$ at $400nm$ up to over $200nm$ at $700nm$) needs to be taken into account. For the spectral sampling of this input band, a balance between accuracy and time efficiency needed to be found, since the amount of distinct input wavelengths linearly effects the computation time. As a default we have set a (changeable) grid spacing of $1nm$ for λ'. This is sufficient for the sampling

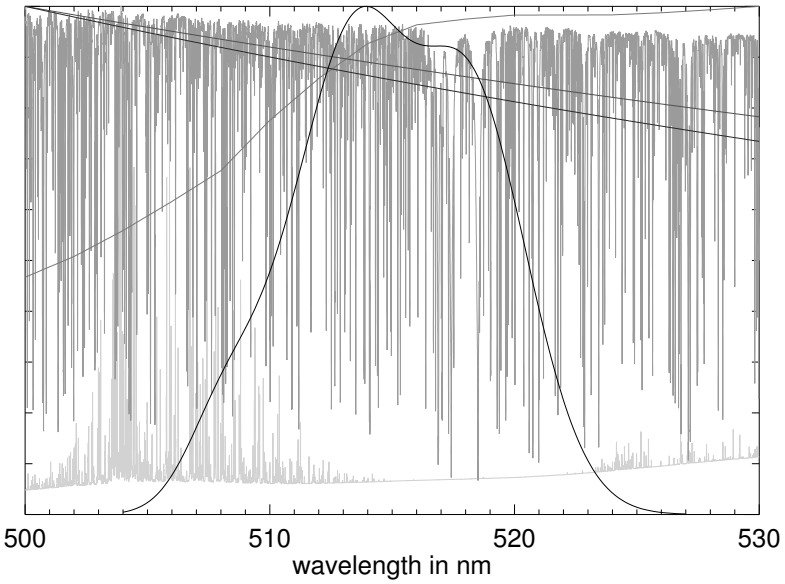

Figure 2.1: A qualitative comparison of the spectral scale of the Raman excitation band emitting at $623nm$ to other spectral model input parameters in their generic resolution. In shades of gray from dark to light and normalized to the upper plot limit: (1) $f^R(\lambda = 623nm)$ as determined by Walrafen [127]. (2) Spectral dependence of the Raman scattering coefficient (as determined by Bartlett et al. [6]). (3) Clear water scattering coefficient for $15°C$ and $35PSU$ salinity (based on [136]). (4) Clear water absorption coefficient for $15°C$ and $35PSU$ salinity (see [101]). (5) The solar spectrum by Kurucz et al. [57], (6) The absorption optical depth of atmospheric gases (the fine scale structure is mainly owed to water vapor and the offset to O_3 and NO_2 absorption) inferred from the HITRAN database ([99]) for a standard atmosphere.

of the absorption and scattering spectra of the water constituents and also of atmospheric aerosols and Rayleigh scattering. The fine scale structure of atmospheric absorption by the atmospheric gases in every $1nm$ interval is treated in a separate module in MOMO, which uses a modified version efficient k-distribution method rather than a line-by-line calculation to accurately derive the absorption coefficients (using the HITRAN spectral line database [99] and the solar spectra from R.L. Kurucz [57]) for each band under consideration of the provided atmospheric composition and the pressure and temperature profiles (see Doppler et al. [23] and Bennartz and Fischer [7]). The Raman spectral redistribution function (1.12) is also sampled with a sufficient spacing for each $1nm$ section (a comparison of the different spectral scales involved in the model input can be found in figure 2.1). Input as well as output quantities with a λ' or λ index in the following sections therefore represent values averaged over a 1nm spectral width. If necessary for an application, spectral filter functions of actual sensors can be applied to the spectral MOMO output to derive synthetic instrument specific measurements. In the cases were a continuous output spectrum shall be computed rather than only an output for single observation wavelength λ, the computation

time per generated output decreases rapidly, since the computed input radiation for a single λ' value then contributes to a whole range of output wavelengths λ.

2.7 Convergence of Raman Scattering Orders

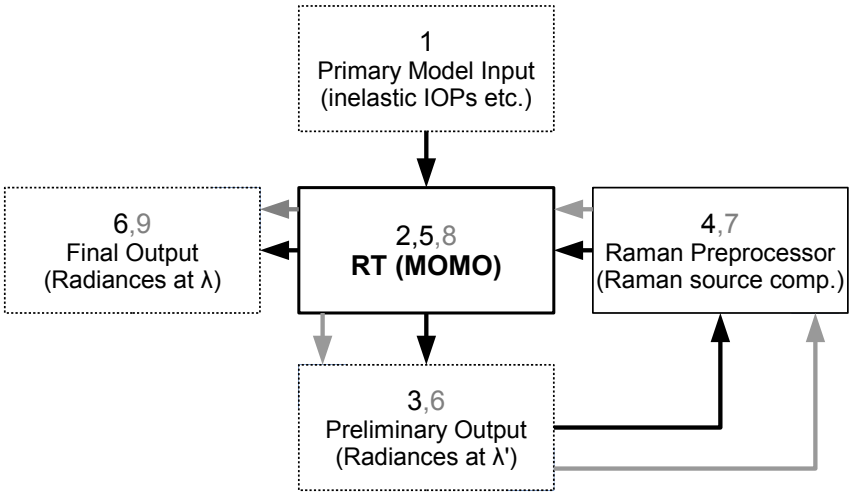

Figure 2.2: A simplified visualization of the steps involved in the computation of radiances including Raman scattering of first order (black arrows and numbering) and second order (gray arrows and numbering).

Since the computation of the Raman source term (1.7) requires the knowledge of the radiation distribution $L'(\lambda')$ in the excitation band, it needs to be discussed how these are retrieved. A monochromatic model run that only allows for elastic scattering (with a $1nm$ spacing for λ'), and therefore treats Raman scattered radiation as absorbed light, provides "zeroth Raman order" radiance values $L'^{(0)}_{\lambda'}$ to obtain a 'first order' source operator:

$$J^{R(1)}_{\lambda}\left(L'^{(0)}_{\lambda'}\right), \tag{2.11}$$

where $^{(1)}$ and $^{(0)}$ stand for the order of Raman scattering included. From $J^{R(1)}_{\lambda}$ the first order output radiance $L^{R(1)}_{\lambda}$ can be computed in a single model run (also see visualizations in figures 2.2 and 2.3), as will be illustrated in the following sections. Since $L'^{(0)}_{\lambda'}$ does not yet include Raman scattering effects, $J^{R(1)}_{\lambda}$ and $L^{R(1)}_{\lambda}$ do not yet include the small fraction of radiation, which is Raman scattered from even shorter wavelengths to λ' and then again Raman scattered from λ' to λ. Previous investigations by Satyendranath & Platt in 1998 had already shown that higher orders of Raman scattering contribute orders of magnitude

less to the radiation field compared to the first order contribution [104]. Nevertheless, MOMO allows to set the number of orders s after which to cut-off.

The output radiation $L^{R(1)}$ at an emission wavelength may be used as excitation radiation $L'^{R(1)}$ emitting at an even longer wavelength, and enable the definition of the more precise source term $J^{R(1)}$ for this longer wavelength. In our model these steps are iteratively repeated until the desired order s is reached, with the dependence on the results of the previous iteration step being:

$$J_{\lambda}^{R(s+1)}\left(L'^{(s)}_{\lambda'^{(s+1)}}\left(J^{R(s)}_{\lambda'^{(s+1)}}\right)\right). \tag{2.12}$$

For a given observation wavelength λ, the excitation wavelength range, that needs to be included in the iteration steps, depends on the maximum order to be computed. For example, if the contribution to an output wavelength $\lambda = 500nm$ is to be computed, the first order contribution comes from the wavelength range $\lambda' = 420nm - 436nm$, the second order contribution originates from $\lambda'^{(2)} = 362nm - 387nm$ and the third order contribution from $\lambda'^{(3)} = 318nm - 348nm$ (two further examples can be found in figure 2.3). The limited availability of accurate IOPs of the water body in the UV spectral region below 300nm, which could serve as input for the model, practically limits the amount of orders for observation wavelengths in the blue or green to two or three. Due to the negative effect on the computation time and the minor contribution of higher inelastic scattering orders, as mentioned before, the first order is considered sufficient for most applications. It also should be pointed out, that even if the iteration is stopped after the first cycle, all elastic (multiple-) scattering events and their combination with a potential inelastic scattering event are accounted for correctly in the doubling algorithm used in MOMO, as will be shown in section (2.10).

2.8 Matrix Operators for Elastic Scattering

The input of our radiative transfer model consists of atmospheric optical properties and the ocean IOPs at each model layer boundary, some of which may be pre-generated from more accessible quantities in external program modules (For example, the phase function and single scattering albedo of aerosols and clouds can be computed from the microphysical particle properties using Mie theory and the absorption coefficients of the atmospheric gases are computed from provided vertical concentration profiles using the k-distribution method [23]). The input IOPs allow to directly compute the reflection- and transmission-operators at every layer boundary position for a very thin vertical layer (with the thickness $\Delta\tau^{ele}/\mu \ll 1$), called an elementary layer, within which entering radiation is highly unlikely

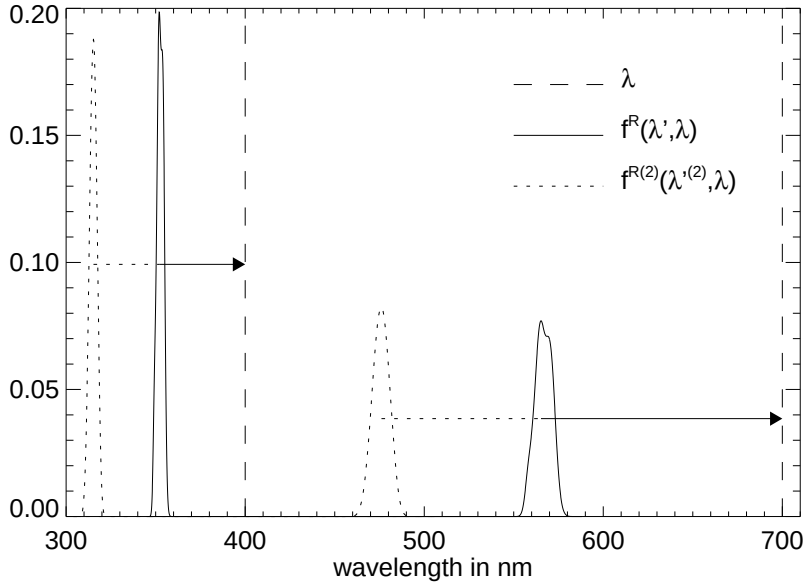

Figure 2.3: Relative spectral Raman contribution functions of first and second order for the emission wavelengths $400nm$ and $700nm$ at $25°C$. While the first order contribution $f^R(\lambda', \lambda)$ is described by equation 1.12, the second order function $f^{R(2)}(\lambda'^{(2)}, \lambda)$ is the convolution $\int f^R(\lambda', \lambda) f^R(\lambda'^{(2)}, \lambda') d\lambda'$.

to undergo more than one scattering process [16, 31]:

$$\mathbf{T}_m^{ele} = \left[\exp\left(-\Delta\tau^{ele}/\mu_i\right)\delta_{ij}\right] + \nu_m\omega_0\Delta\tau^{ele}\mathbf{M^{-1}}\mathbf{P}_m^{\mathbf{T}}\mathbf{C}, \tag{2.13a}$$

$$\mathbf{R}_m^{ele} = \nu_m\omega_0\Delta\tau^{ele}\mathbf{M^{-1}}\mathbf{P}_m^{\mathbf{R}}\mathbf{C}, \tag{2.13b}$$

$$\tag{2.13c}$$

where ω_0 is the single scattering albedo, ν_m is the Fourier index dependent normalization factor of the phase-matrices $\mathbf{P}_m^{\mathbf{R}}$ and $\mathbf{P}_m^{\mathbf{T}}$ and $\mathbf{M}$ and $\mathbf{C}$ are diagonal matrices containing the zenith positions μ_i and the corresponding weights c_i:

$$\mathbf{M}^{-1} = [(\mu_i)^{-1}\delta_{ij}], \tag{2.14a}$$

$$\mathbf{C} = [c_i\delta_{ij}], \tag{2.14b}$$

$$\nu_m = (1 + \delta_{0m})\pi. \tag{2.14c}$$

The square brackets in $\mathbf{M}^{-1}$, $\mathbf{C}$ and the expression $\left[\exp\left(-\Delta\tau^{ele}/\mu_i\right)\delta_{ij}\right]$, that describes the extinction within the thin elementary layer with the Beer-Lambert law, again denote the matrix assembled from the elements within the brackets. δ here represents the Kronecker symbol. As mentioned before, the Beer-Lambert law also allows to directly derive the beam attenuation of the direct solar irradiance at any position τ_n from the extraterrestrial solar

irradiance S'° as in equation 1.4. Therefore, the elementary source operator for elastically scattered direct solar radiation may also be derived straight forward [31]:

$$\mathbf{J}_m^{\circ+ele} = \omega_0 \Delta\tau^{ele} S'^{\circ} \mathbf{M^{-1}} \mathbf{P}_m^{\mathbf{T}} \left[\exp\left(-\tau_n/\mu'^{\circ}_j\right) \delta_{ij}\right], \tag{2.15a}$$

$$\mathbf{J}_m^{\circ-ele} = \omega_0 \Delta\tau^{ele} S'^{\circ} \mathbf{M^{-1}} \mathbf{P}_m^{\mathbf{R}} \left[\exp\left(-\tau_n/\mu'^{\circ}_j\right) \delta_{ij}\right]. \tag{2.15b}$$

Note that, when applying the latter to direct solar fractions of radiation that have reached the water body, the refraction at the surface needs to be taken into account, similar to equation 2.17 and 2.18.

2.9 Matrix Operators for Raman Scattering

Due to its dependence on the incoming radiation at the layer boundaries, the elementary water Raman source term can not directly be inferred from the model input parameters. We have used the general formalism described in sections 1.2 and 1.3 as a basis to create a computation time efficient matrix-operator algorithm that solves the integrals in equation 1.7 in two steps.

To retrieve $\mathbf{J}_m^{Rele}$ for the emission wavelength λ, the spectral integration over all contributing λ' is carried out by an element-wise summing up of the product of the diffuse Fourier radiance operators $\mathbf{L'}_m$ from the excitation band and the other spectral dependent functions in the first step:

$$\overline{\mathbf{L'}_m} = \sum_{\lambda'} \mathbf{L'}^*_{\lambda' m}, \tag{2.16a}$$

$$\mathbf{L'}^*_{\lambda' m} = \mathbf{L'}_{\lambda' m} b^R_{\lambda'} f^R_{\lambda'}. \tag{2.16b}$$

Note that for spectral grid spacings other than the default $1nm$ (when the solar Irradiance is given in Wm^2nm^{-1}), the step width needs to be taken into account by weighting factors in equations 2.16, 2.17 and 2.21. When treating the atmosphere-ocean interface with the wind-speed dependent Cox-Munk model, only diffuse radiation enters the water body. However, in the cases where a flat Fresnel atmosphere-ocean interface model is used, if the solar zenith angle is below the angle of total reflection ($\approx 48.6°$), a fraction of unscattered solar irradiance E'° is transmitted into the water body and may therefore also be Raman scattered. The spectral integration of this separately treated direct solar irradiance contribution reveals the following diagonal matrix as interim result:

$$\overline{\mathbf{E'}^{\circ}} = \sum_{\lambda'} \mathbf{E'}^{\circ *}_{\lambda'}, \tag{2.17a}$$

$$\mathbf{E'}^{\circ *}_{\lambda'} = \left[E'^{\circ}_{\lambda' j} b^R_{\lambda'} f^R_{\lambda'} (\mu'^{\circ(oce)}_j)^{-1} \delta_{ij}\right], \tag{2.17b}$$

where j again is the index of the solar zenith angle and $E'^{\circ}_{\lambda' j}$ at the optical depth position τ_n within the water body is given by:

$$E'^{\circ}_{\lambda' j} = S'^{\circ}_{\lambda'} \exp\left(\frac{\tau^{(atm)} - \tau_n}{\mu'^{\circ(oce)}_j} - \frac{\tau^{(atm)}}{\mu'^{\circ(atm)}_j}\right) \mu'^{\circ(atm)}_j \left(1 - r^F(\mu'^{\circ(atm)}_j)\right). \tag{2.18}$$

Here τ^{atm} is the total optical thickness of the atmosphere and r^F is the solar zenith angle dependent Fresnel reflection coefficient ($0 \leq r^F \leq 1$) described in section 3.2.6 (defined in equation 3.9).

In a second step, the process of the angular integration in equation 1.7 is carried out by the execution of the following matrix multiplications:

$$\mathbf{J}^{R+ele}_m = c^{-1}\Delta\tau^{ele}\nu_m \mathbf{M}^{-1}(\mathbf{P}^{R\mathbf{T}}_m \mathbf{C}\overline{\mathbf{L}'^{+}_m} + \mathbf{P}^{R\mathbf{R}}_m \mathbf{C}\overline{\mathbf{L}'^{-}_m} + \nu_m^{-1}\mathbf{P}^{R\mathbf{T}}_m \overline{\mathbf{E}'^{\circ}}), \tag{2.19a}$$

$$\mathbf{J}^{R-ele}_m = c^{-1}\Delta\tau^{ele}\nu_m \mathbf{M}^{-1}(\mathbf{P}^{R\mathbf{T}}_m \mathbf{C}\overline{\mathbf{L}'^{-}_m} + \mathbf{P}^{R\mathbf{R}}_m \mathbf{C}\overline{\mathbf{L}'^{+}_m} + \nu_m^{-1}\mathbf{P}^{R\mathbf{R}}_m \overline{\mathbf{E}'^{\circ}}), \tag{2.19b}$$

where $\mathbf{M}^{-1} = [(\mu_i^{(oce)})^{-1}\delta_{ij}]$ and $\mathbf{C} = [c_i^{(oce)}\delta_{ij}]$. The extinction coefficient c can be computed from the known optical- ($\Delta\tau$) and geometrical (Δz) thickness of the homogeneous model layer within which the elementary layer is positioned: $c^{-1} = \Delta z/\Delta\tau$. Due to the dependence of $\mu_i^{(oce)}$ and $c_i^{(oce)}$ on the refraction at the air-sea interface, the angles and weights may vary slightly throughout the excitation band if the spectral dependence of the refractive index is strong in that region. If the inaccuracy introduced by the element-wise summing of the radiances at the slightly differing angular positions in equation 2.16 needs to be addressed, an interpolation of all the angular grid points to those at the emission wavelength has to be performed prior to the spectral integration. However, to avoid modifications of the given weights from the Gauss-Lobatto quadrature scheme, this interpolation should best be performed after the matrix multiplication with $\mathbf{M}^{-1}$ in equation 2.19. To accomplish this, the order of the spectral- and the angular integration mentioned above needs to be reversed. The interim results for the initial angular integration then are:

$$\mathbf{L}'^{+**}_{\lambda' m} = \nu_m \mathbf{M}^{-1}(\mathbf{P}^{R\mathbf{T}}_m \mathbf{C}\mathbf{L}'^{*+}_{\lambda' m} + \mathbf{P}^{R\mathbf{R}}_m \mathbf{C}\mathbf{L}'^{*-}_{\lambda' m} + \nu_m^{-1}\mathbf{P}^{R\mathbf{T}}_m \mathbf{E}'^{\circ *}_{\lambda'}), \tag{2.20a}$$

$$\mathbf{L}'^{-**}_{\lambda' m} = \nu_m \mathbf{M}^{-1}(\mathbf{P}^{R\mathbf{T}}_m \mathbf{C}\mathbf{L}'^{*-}_{\lambda' m} + \mathbf{P}^{R\mathbf{R}}_m \mathbf{C}\mathbf{L}'^{*+}_{\lambda' m} + \nu_m^{-1}\mathbf{P}^{R\mathbf{R}}_m \mathbf{E}'^{\circ *}_{\lambda'}). \tag{2.20b}$$

Now the angular interpolation to the grid points μ_i^{oce} at the emission wavelength needs to be carried out for $\mathbf{L}'^{+**}_{\lambda' m}$ and $\mathbf{L}'^{-**}_{\lambda' m}$ for every contributing λ'. Hereafter the spectral integration can be performed by element-wise summing of the matrices $\mathbf{L}'^{+**}_{\lambda' m}$ and $\mathbf{L}'^{-**}_{\lambda' m}$ whose angular sampling points are now aligned:

$$\mathbf{J}^{R+ele}_m = c^{-1}\Delta\tau^{ele} \sum_{\lambda'} \mathbf{L}'^{+**}_{\lambda' m}, \tag{2.21a}$$

$$\mathbf{J}^{R-ele}_m = c^{-1}\Delta\tau^{ele} \sum_{\lambda'} \mathbf{L}'^{-**}_{\lambda' m}. \tag{2.21b}$$

In terms of computational speed the latter algorithm (equations (2.20) and (2.21)) is clearly outperformed by the initial algorithm (equations 2.16 to 2.19), since the matrix multiplications in equation 2.20 have to be performed for every single λ' in the excitation band whereas they only have to be performed once in 2.19. Furthermore the accurate interpolation of the angular grid points requires a sufficiently dense grid of zenith angles. The number of zenith grid points, however, effects the computation speed approximately quadratic. For these reasons the algorithm described by equations 2.16 to 2.19 was chosen as default for MOMO Raman.

Due to the symmetry of the phase function for Raman scattering, the absolute values of the upward and downward Raman source operator elements are generally equal, although the signs for the second Fourier index are opposite. Nevertheless, if necessary MOMO may manipulate diagonal elements of the forward scattering phase matrix by a post normalization process to force a strict energy conservation, especially when only a small amount of zenith angles are used for the sampling of the phase function, which can lead to minor differences in the values. Furthermore, using the same principal scheme discussed here our model also enables to simulate other additional radiation sources that may not underlie the symmetry mentioned above. Therefore, we will continue to distinguish between the upward and the downward source operators.

2.10 Doubling and Adding

To be able to compute radiances at the model boundaries with the equations 2.2, we first need to derive the matrix operators for the model-atmosphere and -ocean from the elementary source operators discussed in the previous section, under inclusion of all occurring (multiple-) scattering events. The general procedure for the latter is the *doubling and adding* method, deduced from the interaction principle and discussed in more detail e.g. in Grant and Hunt [39] and Plass et al. [85]. The resulting equations for the combination of the operators of two adjacent layers, the so called *adding*, are:

$$\mathbf{T}_{20} = \mathbf{T}_{10}(\mathbb{1} - \mathbf{R}_{12}\mathbf{R}_{10})^{-1}\mathbf{T}_{21}, \tag{2.22a}$$
$$\mathbf{T}_{02} = \mathbf{T}_{12}(\mathbb{1} - \mathbf{R}_{10}\mathbf{R}_{12})^{-1}\mathbf{T}_{01}, \tag{2.22b}$$
$$\mathbf{R}_{20} = \mathbf{R}_{21} + \mathbf{T}_{12}(\mathbb{1} - \mathbf{R}_{10}\mathbf{R}_{12})^{-1}\mathbf{R}_{10}\mathbf{T}_{21}, \tag{2.22c}$$
$$\mathbf{R}_{02} = \mathbf{R}_{01} + \mathbf{T}_{10}(\mathbb{1} - \mathbf{R}_{12}\mathbf{R}_{10})^{-1}\mathbf{R}_{12}\mathbf{T}_{01}, \tag{2.22d}$$
$$\mathbf{J}^-_{20} = \mathbf{J}^-_{10} + \mathbf{T}_{10}(\mathbb{1} - \mathbf{R}_{12}\mathbf{R}_{10})^{-1}(\mathbf{R}_{12}\mathbf{J}^+_{01} + \mathbf{J}^-_{21}), \tag{2.22e}$$
$$\mathbf{J}^+_{02} = \mathbf{J}^+_{12} + \mathbf{T}_{12}(\mathbb{1} - \mathbf{R}_{10}\mathbf{R}_{12})^{-1}(\mathbf{R}_{10}\mathbf{J}^-_{21} + \mathbf{J}^+_{01}). \tag{2.22f}$$

If the operators of two adjacent layers with identical properties are to be combined, the identity of upward and downward reflection as well as transmission operators in both

layers leads to the simpler equations of the so called *doubling*:

$$\mathbf{T}_{02} = \mathbf{T}_{20} = \mathbf{T}(\mathbb{1} - \mathbf{RR})^{-1}\mathbf{T}, \tag{2.23a}$$
$$\mathbf{R}_{02} = \mathbf{R}_{20} = \mathbf{R} + \mathbf{T}(\mathbb{1} - \mathbf{RR})^{-1}\mathbf{RT}, \tag{2.23b}$$

where $\mathbf{T}$ and $\mathbf{R}$ are the operators of the initial layer that is being doubled. Starting from the operators for an elementary source layer, the doubling is iteratively repeated until the model layer thickness is reached. Due to the exponential growth of the achieved optical thickness with the number of iteration steps, this is an extremely efficient method to compute the optical properties even of optically thick homogenous model layers.

2.11 Doubling of Raman Sources

Due to the dependence of the Raman source operators on the excitational radiation, which in general follows a gradient within a homogeneous layer, they are not identical in two adjacent homogeneous layers ($\mathbf{J}^R_{01} \neq \mathbf{J}^R_{12}$ and $\mathbf{J}^R_{21} \neq \mathbf{J}^R_{10}$), in contrast to $\mathbf{T}$ and $\mathbf{R}$. Therefore, the equations for the Raman source doubling are:

$$\mathbf{J}^-_{20} = \mathbf{J}^-_{10} + \mathbf{T}(\mathbb{1} - \mathbf{RR})^{-1}(\mathbf{RJ}^+_{01} + \mathbf{J}^-_{21}), \tag{2.24a}$$
$$\mathbf{J}^+_{02} = \mathbf{J}^+_{12} + \mathbf{T}(\mathbb{1} - \mathbf{RR})^{-1}(\mathbf{RJ}^-_{21} + \mathbf{J}^+_{01}). \tag{2.24b}$$

In contrast to the depth dependency of the source operator for the single scattering of direct solar radiation, which can be computed using the Beer-Lambert law (see equation 2.18), the gradient of the Raman source operator within a homogeneous model layer is not directly accessible. Therefore, a method to accurately approximate $\mathbf{J}_{12}$ and $\mathbf{J}_{21}$ from the known initial source operators $\mathbf{J}_{01}$ and $\mathbf{J}_{10}$, the latter being $\mathbf{J}^{+ele}$ and $\mathbf{J}^{-ele}$ in the first iteration, had to be found. The simplest approaches that come to mind are either to omit the *doubling* algorithm in favor of *adding* of the elementary operators, which would be very inefficient for thick layers, or to assume that $\mathbf{J}^R_{01} = \mathbf{J}^R_{12}$ and $\mathbf{J}^R_{21} = \mathbf{J}^R_{10}$, which would be efficient but not accurate for thick homogenous layers. In the latter method, the user can buy an arbitrary increase of accuracy for the price of a corresponding rise in computation speed by increasing the number of layers in the model input. Schroeder et al. [105] suggested an algorithm based on the reasonable assumption that the ratio of the source operators of two adjacent model layers with similar optical properties equals the ratio of the sources of two elementary layers situated at the upper borders of these two

layers, which can be summarized as:

$$\mathbf{J}_{12}^{+} = \left[J_{01ij}^{+} \frac{J_{ij}^{+ele}(\tau_l^*)}{J_{ij}^{+ele}(\tau_n)} \right], \tag{2.25a}$$

$$\mathbf{J}_{21}^{-} = \left[J_{10ij}^{-} \frac{J_{ij}^{-ele}(\tau_l^*)}{J_{ij}^{-ele}(\tau_n)} \right], \tag{2.25b}$$

where τ_n is the upper boundary position of the layer of $\mathbf{J}_{01}^{+}$ and τ_l^* the lower boundary position of the latter as well as the upper boundary position of the layer of $\mathbf{J}_{12}^{+}$. The square brackets again denote the matrix formed by the elements within. Within the doubling procedure, the doubling iteration index l (with $l = 1, ..., L$) and $\Delta\tau^{ele}$ define the vertical position $\tau_l^* = \tau_n + 2^{l-1}\Delta\tau^{ele}$. The minimum value L of necessary iterations to reach the optical layer thickness $\Delta\tau$ is specified by the demand to keep $\Delta\tau^{ele}$ beneath the threshold where the single scattering approximation is valid. It therefore defines the elementary layer thickness $\Delta\tau^{ele} = \Delta\tau/2^L$. While the mentioned approach (equation 2.25) introduces a gain in speed compared to the approach of repeatedly applying the adding algorithm, it nevertheless requires to compute the radiation field at τ_l^* after every iteration step to determine $\mathbf{J}^{\pm ele}(\tau_1(l))$. Since the latter would still considerably increase the computation time in comparison to a real doubling algorithm, where $\mathbf{J}^{\pm ele}$ only needs to be known at the model layer boundary positions τ_n, we have decided to implement an algorithm that benefits from the same assumption the latter algorithm is based on, however interpolates $\mathbf{J}^{\pm ele}$ between the known values at τ_n and τ_{n+1}. Rather than a plane linear fit, we have decided for an exponential interpolation that has shown to approximate the depth dependency of the Raman source operator rather accurately even in thick model layers:

$$\mathbf{J}_{12}^{R+} \approx \left[J_{01ij}^{R+} \left(\frac{J_{ij}^{R+ele}(\tau_{n+1})}{J_{ij}^{R+ele}(\tau_n)} \right)^{2^{l-1-L}} \right], \tag{2.26a}$$

$$\mathbf{J}_{21}^{R-} \approx \left[J_{10ij}^{R-} \left(\frac{J_{ij}^{R-ele}(\tau_{n+1})}{J_{ij}^{R-ele}(\tau_n)} \right)^{2^{l-1-L}} \right]. \tag{2.26b}$$

If this approach should not be sufficiently accurate for an application when sampling the ocean with a single homogeneous layer, the model output accuracy can be increased arbitrarily by dividing thick homogeneous model layers into sub-layers. A discussion of the achievable accuracies can be found in section 6.2.5.

After having computed the source operator (in our case $\mathbf{J} = \mathbf{J}^{\circ} + \mathbf{J}^{R}$) as well as $\mathbf{R}$ and $\mathbf{T}$ for each homogeneous model layer with the doubling algorithm, the adding algorithm 2.22 and the equations 2.2)based on the interaction principle reveal the radiation fields $\mathbf{L}_m$ at the model layer boundaries, which then are back transformed (equation 2.7b) to the azimuthal dependent radiances $L(\theta, \phi)$ in a final step.

2.12 Algorithm Overview

This section shall summarize the steps discussed in this chapter starting from the RT model input and leading to the terrestrial light field including Raman contributions. In a simplified manner, the involved steps are given by:

1. Define the model layer positions and their basic optical properties on a spectral grid containing the excitation band λ' with the help of preprocessors which e.g. compute the atmospheric gas transmittance from a given vertical profile or the scattering matrix of particles from their microphysical properties (see section 2.6).

2. Transform the azimuthal dependence of the phase function into Fourier space to enable solving of the RTE with zenith dependence only (see section 2.4).

3. Use the optical properties from the model input to derive matrix operators describing the reflection and transmission properties of infinitesimal layers of the medium at the model layer boundaries for all λ' (see section 2.8).

4. From the latter, compute the reflection and transmission operators of all homogeneous layers for all λ' using the *doubling* algorithm (see section 2.10).

5. Compute the reflection and transmission operators of the whole system for all λ' by combining the operators of the different model layers with the *adding* algorithm (see section 2.10).

6. Solve equations 2.2 with the inserted operators to retrieve the radiances at λ', with the azimuthal dependence still Fourier transformed (see section 2.3).

7. Use the latter to compute the Raman source operator at the emission wavelength λ of an infinitesimal layer at every model layer boundary (see section 2.8).

8. From the latter, compute the reflection and transmission operators at λ using the *doubling* algorithm while using a modified version of the algorithm to compute the Raman source operators of all homogeneous layers (see section 2.10).

9. Compute the reflection, transmission and source operators of the whole system at λ, again by combining the operators with the *adding* algorithm (see section 2.10).

10. Solve equations 2.2 with the inserted operators to retrieve the radiances at λ, now including contributions of VRS (Raman scattering) (see section 2.3).

11. If the desired order of Raman scattering is not yet reached, start over with step 7 (hereby treating the prior emission band λ as new excitation band λ'), else move on (see section 2.6).

12. Perform a Fourier back transformation of the radiances to regain the azimuthal dependence and write the resulting radiances for λ at every model layer boundary to an output file (see sections 2.4 and 2.10).

Any further steps, such as the computation of reflectances or Raman fractions, are subject to postprocessors that generate their output on the basis of the MOMO Raman output radiances and irradiances.

Chapter 3

Model Input

3.1 Introduction

This chapter discusses the models and approaches that result in the optical properties required as input for the radiative transfer model described in chapter 2. Since the main work of this thesis focused on the implementation of a water Raman scattering model and the study of its effect on radiation fields available for remote sensing, the water model will be described in detail whereas the atmospheric model will only be introduced briefly. The Raman preprocessor, the preprocessors for the absorption coefficient and elastic scattering coefficient of clear water, and the bio-optical models have been implemented within this thesis by the author, whereas the remaining preprocessors have been existing previously and are introduced for the sake of completeness.

Some further, pre-existing general preprocessors have been used as tools within this thesis and are therefore mentioned here briefly. This includes a Mie-scattering code to compute optical properties of spherical scattering particles given their microphysical properties (complex refractive index and size distribution) based on a numeric approach of Bohren and Huffman [8]. Another MOMO preprocessor takes care of the assignment of vertical extinction profiles of aerosols, clouds and suspended and dissolved matter in the ocean to the grid of the chosen model layers.

3.2 Preprocessors for Water IOPs

The requirements from a user point of view for the ocean part of our radiative transfer model are to enable the simulation of real world water bodies as realistic as possible in the shortest possible computation time. While the *doubling* method featured in our RT model generally enables quick computations of resulting radiances even in optically dense and geometrically thick media, as e.g. a turbid thick water body in the infrared spectral region, the accuracy to which the simulations reproduce a real world case strongly depends on the inherent optical properties (IOPs) of the water body, that need to be provided by the user as input for the RT model. In the following, the input format and a number of

preprocessors, designed to generate IOPs from more accessible input variables as e.g. the water temperature and the concentration of scattering or absorbing particles suspended or dissolved in water, are introduced.

In contrast to the previous MOMO code versions, that featured a fixed water model integrated in the code, the MOMO Raman code allows for the input of spectral dependent values of the absorption coefficient $a(\lambda)$, the elastic volume scattering function $\beta(\lambda)$ and the real part of the refractive index $n(\lambda)$. The MOMO Raman code package includes an optional preprocessor to compute these values for a given temperature, salinity and wavelength. The computation follows a scheme designed within the framework of the the ESA *WaterRadiance* project by Röttgers et al. [101][100, 103]. The details can be found in section 3.2.1. Figure 3.1 shows maps of global mean values of temperature and salinity at the ocean surface from the *NOAA World Ocean Atlas 2009* ([61, 2]). As default values for the computations in the preprocessors a water temperature of $T = 15°C$ and a salinity of $S = 35PSU$ is set. The salinity value of $35PSU$ represents an average value for many applications sufficiently representing the oceans of midlatitudes. Significantly lower values are in place in regions with strong freshwater intake (e.g. by rivers or melting ice) and especially in inland waters. The chosen default temperature of $T_0 = 15°C$ represents a temperature median rather than a globally valid approximation, due to the strong increase from subzero temperatures at the poles to $0°C$ in the tropics, and the seasonal variation.

Optical output from bio-optical models for Case 1 and Case 2 waters in form of extinction coefficients, single scattering albedos and scattering phase functions are accepted as input by the RT model. Vertical profiles can be set by defining different sets of the latter input variables and assigning them to the model layers with weighting functions generated by the preprocessors mentioned at the beginning of this chapter.

The routine that computes the Raman source operators accepts the value and spectral exponent of the Raman scattering function b^R. If not set, default values of $b^R = 2.7 \cdot 10^{-4} m^{-1}$ and $n = 5.5$ are used (see section 1.3.6 and 1.3.7 for details).

In the following, the preprocessors that generate the optical input mentioned above to simulate a realistic water body with the new MOMO-Raman code, are introduced. The preprocessors for clear water absorption and elastic scattering as well as the the bio-optical models were implemented along with the work on the main RT program, because they were a requirement for the sensitivity studies introduced in chapter 6.

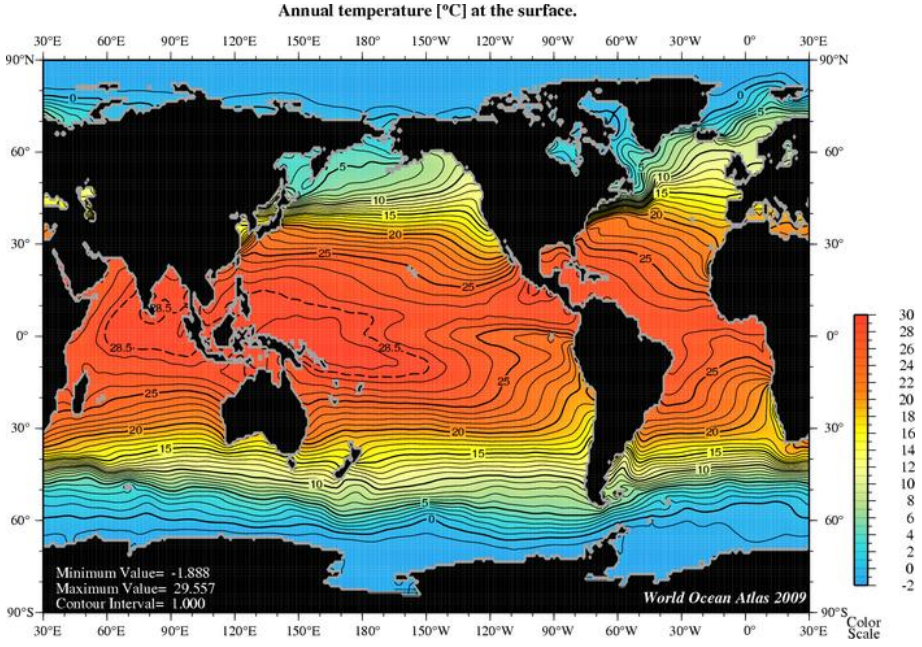

(a)

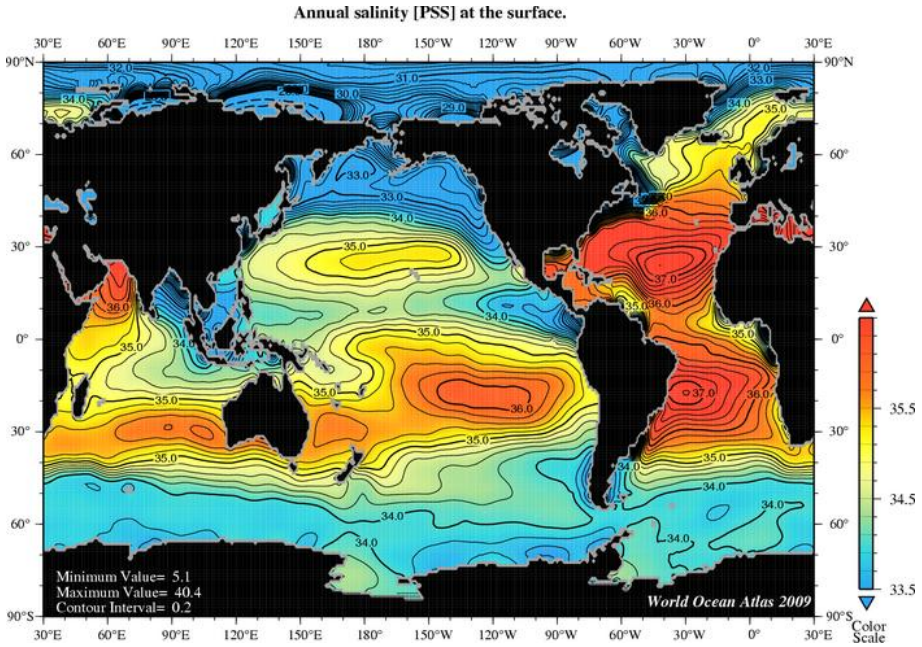

(b)

Figure 3.1: Climatology of the global annual temperature and salinity of the ocean at the sea surface (Reproduced from: *NOAA World Ocean Atlas 2009*, [61, 2]).

3.2.1 Clear Water Absorption

The clear water absorption coefficient is computed from spectra merged from the published values of Pope and Fry [87], Lu [62], Wang [128], Segelstein [107] and Wieliczka et al. [130]. Missing data and the relative temperature and salinity dependence of the coefficient were determined by Röttgers et al. [100] using a point source integrating cuvette absorption meter (PSICAM), combined with temperature and salinity dependence data of Max and Chapados [64]. The water model consists of the tabled spectra of the clear water absorption coefficient a at $T_0 = 20°C$ and $S_0 = 0PSU$, as well as the spectra of the relative temperature coefficient Ψ_T and the salinity coefficient Ψ_S. With the assumption of a linear salinity and temperature dependence, as is supported by the underlying measurements, the absorption coefficient is given by:

$$a(\lambda, T, S) = a(\lambda, T_0, S_0) + \Psi_T(\lambda)(T - T_0) + \Psi_s(\lambda)(S - S_0). \tag{3.1}$$

The preprocessor accepts wavelength, temperature and salinity as input and returns interpolated values of a as output. Figure 3.2 shows the absolute and the relative effect of temperature and salinity on the clear water absorption coefficient as well as the relative salinity and temperature coefficient spectra, which vary over several magnitudes between 400 and $800nm$. The coefficients imply that for most wavelengths the global sea temperature variations have a far greater impact on clear water absorption than the mean salinity variations.

It shall be pointed out again that the water IOPs in the UV spectral range are of importance for the determination of Raman emission in the visible spectral range. However, the measurement of the clear water absorption coefficients in this spectral region are challenging, to to the strong impact of any sample contamination. The variation in the values between widely used coefficients , e.g. Quickenden and Irvin [93], Pope and Fry [87] (extrapolated) and Smith and Baker [109], is nearly one order of magnitude [120], with the respective impact on the derived Raman emission.

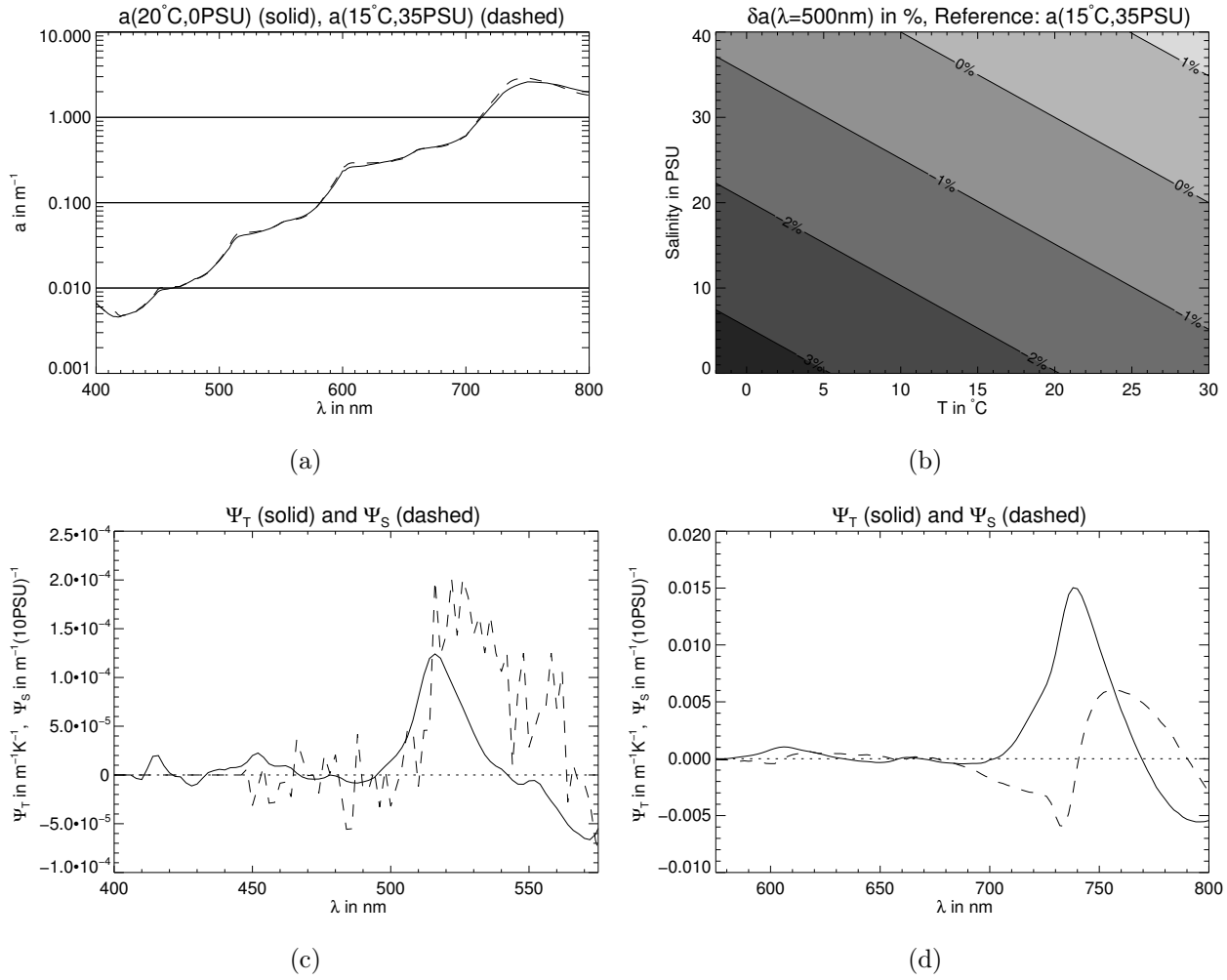

Figure 3.2: (a): Clear water absorption coefficient a for reference conditions ($20°C, 0PSU$, solid line) and standard conditions ($15°C, 35PSU$, dashed line).(b): Relative dependence of the clear water absorption coefficient on temperature and salinity. The reference value of a is for $T = 15°C$ and $S = 35PSU$. (c) and (d): The relative temperature- (solid lines) and salinity- (dashed lines) coefficients from formula 3.1. The temperature is given per change of one Kelvin whereas the salinity coefficient is given in a change per $10PSU$.

3.2.2 Clear Water Elastic Scattering

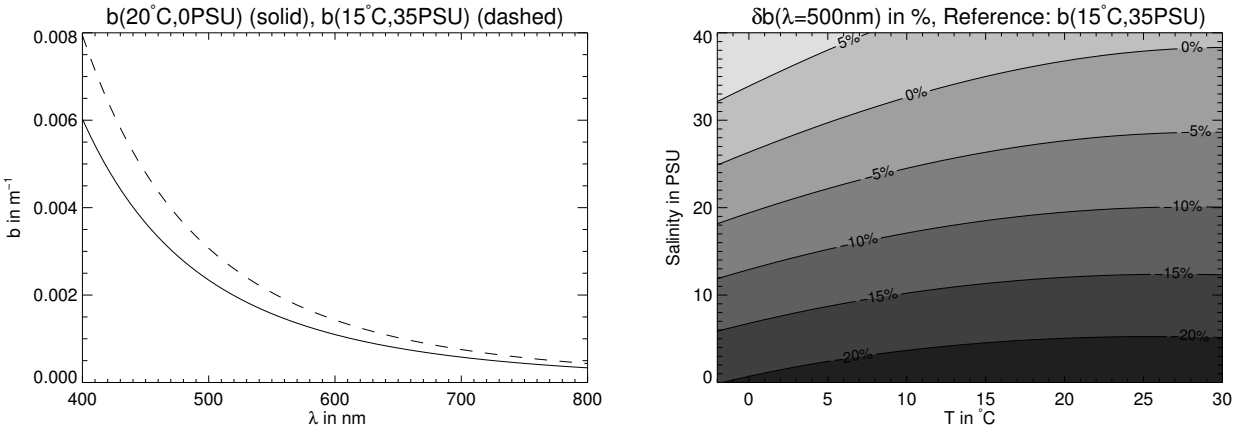

(a) (b)

Figure 3.3: (a): clear water scattering coefficient for reference conditions $(20°C, 0PSU)$ and standard conditions $(15°C, 35PSU)$.(b): Relative dependence of the clear water elastic scattering coefficient on temperature and salinity with respect to $b(T = 15°C, S = 35PSU)$.

The computation of the scattering coefficient b of clear water is based on the physical description of scattering as a result of changes of the refractive index due to fluctuations of the molecule number density by Zhang et al. [136], taking the temperature and salinity dependence into account. The underlying general principles are described by the Einstein-Smoluchowski theory. For the computation of the real part of the refractive index, an empirical theory of Quan and Fry [92] based on measurements of Austin and Halikas [4] is used [103].

The phase function of elastic clear water scattering in the ocean (shown in figure 1.1) is an inherent component of the MOMO code, though it can be chosen if a depolarization ratio dependent or independent formulation shall be used.

Figure 3.3(b) shows the relative dependence of the scattering coefficient for the global temperature and salinity value range of the ocean at $\lambda = 500nm$. Apparently salinity variations in this range have a stronger impact on the real part of the refractive index than temperature changes, resulting in an increase of the scattering coefficient of over 20% (at $T = 15°C$) when moving from fresh water to ocean water with a salinity of $35PSU$.

Alternatively, a comparably simple model for b based on the measurements and computations of Morel [74] is available within the MOMO code.

3.2.3 Clear Water Raman Scattering

The computation of the elementary Raman source operators $\mathbf{J}_m^{ele}$ for a very thin layer at every model layer boundary, as described in section 2.9, is realized by a preprocessor that

requires radiances from the excitation band with a Fourier decomposed azimuth dependence as input. An exception is the multiplication with the prefactor $c^{-1}\Delta\tau^{ele}$ in equation 2.19, which is performed within the main RT Program to minimize I/O, rather than within the preprocessor. The output of the preprocessor is temporarily stored in a file which serves as input for the main RT program. Optional inputs for the Raman preprocessor are the value and the exponent of the Raman scattering coefficient and the Raman phase function (e.g. if isotopic scattering shall be assumed).

The *doubling* of the latter elementary source operators to retrieve the Source Operators of the model layers, as described in section 2.11, is a component of the RT program, due to its dependence on (multiple) elastic scattering and absorption within the water body.

3.2.4 Bio-Optical Models

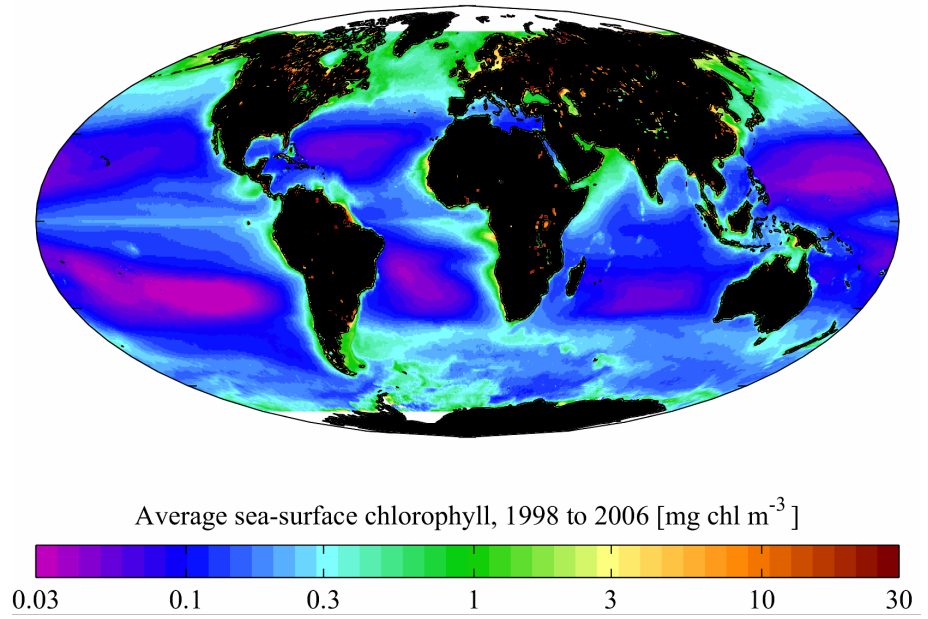

Figure 3.4: Global average chlorophyll associated to phytoplankton at the sea surface measured by SeaWIFS 1998-2006 (Image source: [86])

A bio-optical model describes the relation of the concentration of organic marine particles and the according IOPs of the water body. Due to the great variety of possible models and the dependence of a suitable model on the type of application and the region, within this thesis bio-optical models were implemented with respect to there usability for the applications presented in chapter 6. Hereby a distinction between two rather different types of approaches is made and described in the following. While the focus in the first model is on the qualitative simulation of Case 1 type waters representative for the open ocean, where the ocean color is dominated by organic particles and there pigments, the second model allows a quantitative adaption to any type of waters, including i.a. coastal

Case 2 waters with a significant amount of inorganic suspended particles. The models will be referred to as *model 1* and *model 2* in the following chapters.

Model 1: Single Parameter Model for Qualitative Studies

The actual spectral IOPs depend on the vertical concentration profiles not only of phytoplankton, but also on the amount of non-living organic fragments caused i.a. by decay of the latter, called detritus, leading to dissolved organic matter whose optically measurable component is referred to as yellow substance. A bio-optical model with a single variable, referred to for instance as chlorophyll or pigment concentration, may however still be useful for sensitivity studies of the effect of the variation of system parameters other than the oceanic constituents. A general study of the impact of water Raman scattering on radiances measured by a satellite based sensor for a range of average conditions is such a case. Furthermore, the concentration of yellow substance is generally related to that of chlorophyll, though in a non-linear way due to the decrease of the detrital matter fraction with increasing phytoplankton concentration. An exception of the latter is a weak background component in some regions and a chlorophyll concentration independent fluctuation of the yellow substance absorption a_{ys} [10].

In simple bio optical models chlorophyll, or more specific chlorophyll a absorption, is often used as an easily measurable and quantifiable (but imprecise) proxy for phytoplankton biomass and it's photosynthetic activity. We adopt the approach of Morel and Gentili [77], which requires a tabled chlorophyll spectrum and a concentration value C_{chl} given in $\frac{mg}{m^3}$ as input. Our phytoplankton chlorophyll reference absorption coefficients $\tilde{a}_{chl}(\lambda)$ are normalized to 440nm and originate from Morel [76]. The original table only contains data from 350-700nm, values beyond this range are extrapolated. Alternatively, values recently provided by A. Bricaud in 2010 through personal communication are available for the preprocessor (references include [11],[12], and for particulate absorption [13]). The concentration dependency of the reference coefficients $\tilde{a}_{chl}$ is approximated by:

$$a_{chl}(\lambda) = 0.06 \cdot \tilde{a}_{chl}(\lambda) \cdot (C_{chl})^{0.65}, [C] = \frac{mg}{m^3}. \tag{3.2}$$

The absorption by associated yellow substance (also called *gelbstoff* or colored dissolved organic matter, *CDOM*) is assumed to be:

$$a_{ys}(\lambda) = 0.012 \cdot (C_{chl})^{0.65} \cdot \exp\left[-0.014(\lambda - 440)\right], [\lambda] = nm, [C] = \frac{mg}{m^3}, \tag{3.3}$$

where the spectral coefficient 0.014 is an approximative mean for a value range determined by Bricaud et al. [10]. Nevertheless, a value of 0.011 has been adopted in some other bio-optical models. Both the featured spectral dependencies of a_{chl} and a_{ys} have already been reported by Prieur and Sathyendranath [91].

The scattering coefficient b_{ass} associated to phytoplankton and detrital matter is derived from an empirically determined relationship of the total water scattering coefficient b_T at $550nm$ to the pigment concentration in Case 1 waters by Morel [75]. He found that:

$$b_T(550nm) = \tilde{b}_T(C_{chl})^{0.62}, \tag{3.4}$$

with $\tilde{b}_T$ varying between 0.12 and $0.45m^{-1}$ and a mean value of 0.3. Since total scattering by pure sea water is much weaker than the total particulate scattering (see figure 6.1(b)), the latter may also be used for $b_{ass}(550nm)$. With the assumption of a λ^{-1} wavelength dependence, which according to observations is a good approximation at least for low concentrations ($C < 0.1mg/m^3$) [37], b_{ass} is given by:

$$b_{ass}(\lambda) = \frac{550}{\lambda} \cdot 0.3 \cdot (C_{chl})^{0.62}, [\lambda] = nm, [C] = \frac{mg}{m^3}. \tag{3.5}$$

All coefficients have the unit m^{-1}. For the angular distribution of the scattered light, the phase function of Petzold [83] based on his measurements in the San Diego harbor area is used [83]. Due to the concentration independent phase function of the bio-optical model, Gordon [35] suggested that backscatter events may be overrepresented for growing concentrations (Also see discussion at the end of section 3.2.4, where this issue is addressed again). A more detailed coverage of bio-optical model preprocessors used with in our group with MOMO, especially for specific regional conditions, can be found e.g. in Ebert [24]. It shall also be reminded that, owing to the general measurement principals, a partial inclusion of Raman scattering and fluorescence effects in form of "pseudo" absorption in the featured coefficients can not be ruled out.

Figure 3.4 shows a global climatology mean of chlorophyll associated to phytoplankton at the sea surface, derived from a satellite based imaging spectrometer. Apart from the displayed SeaWIFS data, i.a. the ESA instruments MERIS on Envisat (2002-2012) and OLCI on the upcoming Sentinel-3 mission provide global coverage of the latter data.

Model 2: Flexible Multi Parameter Model for Quantitative Scene Simulation and Retrievals

Applications that require detailed simulated spectra of water leaving radiances for Case 2 water bodies have to feature a bio-optical model that enables to set the concentrations of different oceanic organic and inorganic components. The implemented approach was initially developed by R. Doerffer at *HZG* and *Brockmann Consult* within the *ESA Water-Radiance* and *CoastColour* projects [14]. Rather than to define the IOPs dependence on the microphysical properties of the different species, it is based directly on optical parameters with the option to regionally specify the IOP to constituent concentration relationship. The model is based on the experience, that the bulk of possible spectra can be reproduced by a very limited number of IOPs.

While the pigment absorption is based on measurements like in Model 1, the absorption by yellow substance and detritus as well as the scattering by suspended particles are represented by the mixture of 2 absorption and 2 scattering spectral exponents, each marking the extremes of the possible spectral variations, accompanied by the realistic ranges of possible extinction coefficients for each. Assumptions regarding the yellow substance and detritus absorption spectra are therefore avoided. The exponents are listed in tabular 3.1.

While the default source for pigment absorption is the same as in model 1, others in our research group have been using an alternative data set from Bricaud et al. (see e.g. Bricaud

Description	λ_0	Spectral Model Exponent
pigment absorption	440nm	tabled data
detritus absorption	440nm	0.01
yellow substance absorption	440nm	0.02
white scatterers (big)	550nm	0
blue scatterers (small)	550nm	1

Table 3.1: The five optical components of bio-optical model 2, the reference wavelength for which the extinction coefficient needs to be provided, and the exponent describing the spectral decrease.

et al. [11, 12, 13]). By default the angular dependence of the scattering is simulated using the phase function of Petzold [83] based on his measurements in the San Diego harbor area is used [83]. However, in agreement with suggestion by Zhang et al. [135], others in our institute have been using a phase function with a less pronounced back-scattering peak [44].

3.2.5 Chlorophyll and Yellow Substance Fluorescence

In addition to the absorption and elastic scattering by organic water constituents, treated by the bio-optical models presented in section 3.2.4, some of the constituents may also inelastically scatter a significant amount of the incident radiation into certain spectral bands.

Following the fundamentals of isotropic chlorophyll *a* and yellow substance fluorescence discussed in section 1.4, the matrix representations of the according elementary source operators of fluorescence can be defined from equation 1.26 (for more details, also see [26, 105]). If a column vector $\mathbf{A}^X = [A^X(\mu_i'^{\circ})]$ is defined, the elementary source operator of fluorescence for an optically thin layer with the optical depth $\Delta\tau^{ele}$ at the layer boundary position τ_n, is given by:

$$\mathbf{J}_0^{Xele} = c^{-1}\Delta\tau^{ele}\Phi^X\lambda^{-1}(4\pi)^{-1}\mathbf{M}^{-1}\mathbf{A}^X, \tag{3.6}$$

where $\mathbf{M}^{-1} = [(\mu_i^{(oce)})^{-1}\delta_{ij}]$ again, and

$$\mathbf{J}_{m>0}^{Xele} = 0. \tag{3.7}$$

In comparison to the elementary matrix operators for clear water Raman scattering in section 2.9, the computation of $\mathbf{A}^X$ does not require the knowledge of radiances at the model layer boundaries, but only of the diffuse scalar and direct irradiances (see section 1.4). $\mathbf{J}^{Xele}$ only depends on the position τ_n and the solar zenith angle, not on the azimuth and zenith observation angle.

If the output ($\mathbf{J}_0^{Xele}$) is written to a file, following the format and conventions mentioned in section 3.2.3 for the VRS preprocessor output, the MOMO Raman RT program can use this file as input to simulate the fluorescence effect.

The heritage of chlorophyll fluorescence simulations with MOMO reaches back to the works of Fischer et al. [29]. While based on the same physics, a future re-implementation will enable to synergistically use the new MOMO Raman infrastructure to get rid of some limitations of this initial approach that are discussed in section 4.6.

3.2.6 The Sea Surface

The bottom of the sea is assumed to be a Lambertian reflector whose reflectivity ρ_s can be set (with $\rho_s \in [0, 1]$). The sea surface, on the other hand, is treated as an infinitesimal layer located between the atmosphere and the ocean.

While the simulation of a flat water surface is the default setting and the computation of the respective transmission and reflection matrix operators are a part of the main MOMO program, the simulation of a rough air-sea interface requires the use of preprocessor to determine the latter operators. Both routines have been part of the MOMO code prior to the MOMO Raman development and in general had not needed to be changed, with an exception being the possibility to turn off diffuse and direct surface reflections for radiation coming from above to enable the computation of water leaving radiances. Therefore only a short overview of the underlying principles shall be given here, among others based on the more detailed descriptions in [26, 31].

The Flat Fresnel Surface

The operators for a flat water surface can be derived from Snellius' law of refraction and the Fresnel formulas. Snellius' law gives the direction change of a ray passing through the boarder between two dielectric media:

$$n_1 \sin\theta_1 = n_2 \sin\theta_2, \tag{3.8}$$

where n_1 is the refractive index of one medium (e.g. $n_1 \approx 1$ for air) and n_2 the one of the other (e.g. $n_2 \approx 1.34$ for water) and θ_1 and θ_2 are the zenith angles of the light propagation direction in the corresponding media. Equation 3.8 is therefore also an essential part of the calculation of the zenith angle grid in the ocean with the modified Gauss-Lobatto quadrature scheme.

The Fresnel formulas relate the relative intensity of the reflected perpendicular and parallel polarized electric field components at the dielectric interface to the the refractive indices of the media. Different forms can be found in literature, while a convenient one for use in an RT model is a form that depends only on the cosine (μ) and not the sinus of the incident angle (as e.g. displayed in [32, 26]). The mean of the squared parallel and perpendicular components is the scalar Fresnel reflection coefficient for radiances, being

the fraction of the incident radiation that is reflected at the interface:

$$r_x^F(\mu, \tilde{n}_x) = \frac{1}{2}\left[\underbrace{\left(\frac{\mu - \sqrt{\tilde{n}_x^2 - 1 + \mu^2}}{\mu + \sqrt{\tilde{n}_x^2 - 1 + \mu^2}}\right)^2}_{\perp} + \underbrace{\left(\frac{-\tilde{n}_x^2\mu + \sqrt{\tilde{n}_x^2 + 1 + \mu^2}}{\tilde{n}_x^2\mu + \sqrt{\tilde{n}_x^2 + 1 + \mu^2}}\right)^2}_{||}\right], \tag{3.9}$$

were $x = 1$ and $\tilde{n}_1 := n_2/n_1$ in medium 1 and $x = 2$ and $\tilde{n}_2 := n_1/n_2$ in medium 2. The coefficient for the optically denser medium 2 (e.g. the ocean) reaches a value of 1 for zenith angles that are equal or greater than the critical angle of $\theta_t = \arcsin(n_2/n_1)$. This means that radiation reaching the water surface from below under a zenith angle of roughly 49° or more is subject to total reflection. This, as can also easily be seen from equation 3.8, also implies that radiation transmitted through the interface coming from the atmosphere is diffracted into a cone within the water body. The resulting increase of radiation per solid angle in the ocean, when considering the fraction of radiation entering the interface without being reflected to be $t_1^F := (1 - r_1^F)$, requires to be corrected for with a factor $\tilde{n}_x^2$ [31], which ensures energy conservation. The corrected Fresnel transmission coefficient for radiances is therefore given by:

$$\tilde{t}_x^F(\mu, \tilde{n}_x) = \left(1 - r_x^F(\mu, \tilde{n}_x)\right)\tilde{n}_x^2. \tag{3.10}$$

The reflection and transmission matrix operators ($\mathbf{R}^{F\pm}$ and $\mathbf{T}^{F\pm}$) of the flat interface can be inferred directly from the Fresnel coefficients and are equal for all Fourier indexes m. The reflection operator for the atmosphere side is an $N^{(atm)} \times N^{(atm)}$ diagonal matrix with the elements of $r_{(atm)}^F(\mu_i^{(atm)}, \tilde{n}_{(atm)})$ on the main diagonal ($i = j$). The reflection operator for the ocean side is an $N^{(oce)} \times N^{(oce)}$ diagonal matrix with the elements of $r_{(oce)}^F(\mu_i^{(oce)}, \tilde{n}_{(oce)})$ on the main diagonal for $i \leq N^{(atm)}$ and 1 for the remaining main diagonal elements, due to total reflection. In order to convert the dimensions of the lightfield from $N^{(atm)} \times N^{(atm)}$ in the atmosphere to $N^{(oce)} \times N^{(oce)}$ in the ocean, the transmission operators of the interface are not square matrices. The transmission operator from the atmosphere to the ocean has the dimensions $N^{(atm)} \times N^{(oce)}$ and has the values $t_{(atm)}^F(\mu_i^{(atm)}, \tilde{n}_{(atm)})$ on the main diagonal for $i \leq N^{(atm)}$ and 0 elsewhere. The transmission operator from the ocean to the atmosphere has the dimensions $N^{(oce)} \times N^{(atm)}$ and has the values $t_{(oce)}^F(\mu_i^{(oce)}, \tilde{n}_{(oce)})$ on the main diagonal for $i \leq N^{(atm)}$ and 0 elsewhere. The Fresnel case of a flat interface distributes all incident radiation by diffraction at the flat surface. Due to the symmetry of the flat surface the direct solar radiation coming from $\mu'^{\circ(atm)}$ can be described in terms of a reflected direct fraction (direction μ'° but azimuth shifted by 180°) and a transmitted direct fraction in the direction $\mu'^{\circ(oce)}$. Therefore no sources of diffuse radiation (as e.g. from scattering processes) need to be taken into account within the flat interface layer ($\mathbf{J}^{F\circ} = 0$)).

The Rough Sea Surface

The simulation of the effect of a rough sea surface on the reflectance, due to wind driven surface waves, is available in form of a preprocessor with a wind speed dependent input parametrization. The process was originally implemented and described by Fell [26] for the MOMO model. The chosen approximative approach has shown to provide sufficiently accurate results for the low and medium zenith angle range and does not include the effect of the wind direction, which would i.a. require to additionally include the sinus coefficients in the azimuth dependence decomposition described in section 2.4. The simulation of tiny planar facets with different orientations, each of which can be treated as a flat surface with the Fresnel formulas discussed in section 3.2.6, provide the basis of the wave model. COX and MUNK [19] provided an empiric linear model that relates the wind speed at a height of $10m$ in m/s to a width parameter of an assumed Gaussian distribution of the facets by the evaluation of sun glint photographs. The reflected light field for a given wind speed may then be computed by summing up of the components of all orientations, if shadowing effects are neglected. The angular distribution and azimuth dependence of the effect, in contrast to the flat Fresnel surface, leads to a redistribution of direct solar irradiances into diffuse radiances, and therefore leads to a source operator $\mathbf{J}^{\circ} \neq 0$. A detailed description of the method is provided by Nakajima and Tanaka [80]. A description of the implementation in the scalar MOMO version, which adopts the transmission operator type from the flat Fresnel surface to avoid the difficulties related to the Fourier expansion of the azimuth dependency of the strongly peaked downwelling radiance distributions, can be found in Frank Fell and Jürgen Fischer [31]. Nevertheless, the interface implemented in the newer vector MOMO code that includes polarization effects also accounts for the wind speed effect on the transmitted radiation [44], given the increased computing power which had become available in the meantime.

The effect of whitecaps, which have an impact on measured reflectivities for higher wind speeds ($10 - 15m/s$), can be simulated by adding a layer of water including white scatterers just below the surface. Yet higher wind speeds are only rarely observed in clear sky conditions, which are generally required for satellite based ocean color remote sensing applications.

3.3 Atmospheric Preprocessors

Atmospheric preprocessors were inherited unchanged from the previous MOMO model version, but a brief overview of the underlying techniques shall be given. While the elastic scattering by air molecules is accounted for within the main RT program run with respect to the provided pressure profile of the atmosphere, the small scale spectral structure of absorption by atmospheric gases requires a separate treatment in a preprocessor. The preprocessor uses an efficient modified k-distribution approach (of [7]), which derives relative weights for bins, sorted by extinction magnitude rather than wavelength, and allows to reduce the amount of data for a required accuracy level in significantly. The absorption

line data is extracted from the HITRAN[99] spectral line database and the temperature, pressure and gas concentration profiles are taken into account. The method allows to define broader spectral bands for the actual RT model runs. The structure of MOMO provides a direct interface for the processing of the k-bin values. A detailed description of the method can be found in Doppler et al. [23] and Bennartz and Fischer [7].

A preprocessor for the computation of rotational Raman scattering sources, based on the theoretical approach described in section 1.5, is in a development and testing stage by the author of this thesis.

Chapter 4

Model Versions

4.1 Introduction

Chapter 2 described the implementation of the latest program code version 2.1. However, the development and validation of the MOMO Raman code followed an iterative process. Therefore, if code versions other than 2.1 were used to produce results in the following chapters, it will be pointed out. The process of the code development shall be shown in this chapter by the introduction of the subsequent code iterations in the following.

4.2 MOMO Raman 1.0

Within the ESA funded *support to science* project *WaterRadiance*, the initial code version 1.0 was developed and validated via a model intercomparison to the commercial ocean Radiative transfer model HydroLight 5.0 [65], which optionally included Raman scattering effects (though with a simplified treatment of the angular dependence). This MOMO code version featured a loop based execution of the spectral and angular integrations in equation 1.7 for the Raman source operator determination, rather than the Matrix Operator approach displayed in equations 2.19. Furthermore, the source operators of two adjacent numerical layers within one model layer were assumed to be equal, which simplifies equations 2.26, as discussed in section 2.10, to:

$$\mathbf{J}_{12}^{R+} \approx \mathbf{J}_{01}^{R+}, \tag{4.1a}$$

$$\mathbf{J}_{21}^{R-} \approx \mathbf{J}_{10}^{R-}. \tag{4.1b}$$

Due to the neglect of a possible depth dependency of the excitational energy within a single homogeneous model layer, it was required to choose the model layer thickness according to the desired accuracy of the computed Raman fraction. The latter was done by a preprocessor which determined the vertical positions of the ocean model layers with a focus on accurate water leaving radiances, meaning that that the layers in greater depths, which contribute less to the upwelling radiation field above the water surface, were chosen to be thicker to save computation time.

4.3 MOMO Raman 1.1

The HydroLight software, which had served as a basis for the validation of MOMO Raman Code version 1.0, was later subject to bug fixes and changes in the code section treating Raman scattering, thus leading to differences in the output regarding Raman fractions in the new code version HydroLight 5.1.4. The new HydroLight version was accompanied by a technical note that gave insight in some of the models settings regarding Raman scattering [69]. Likewise, consistency checks of all contributing subroutines in the MOMO Raman code, including tests to assure energy conservation in every step etc., were performed. In this effort, a bug in the weighting of the fraction of elastically scattered radiation which is subsequently Raman scattered, which led to underestimation of 1-3% of the Raman fraction of the water leaving irradiances (and to higher differences at very low solar altitudes), was identified and removed. Also, the possibility to compute Raman sources for the case of a spectral dependent refractive index of the water was added. Finally, the memory saving assumption of a forward/backward symmetry of the Raman phase function and the source operators was given up in an effort to generalize the Raman input structure in MOMO for a possible future use with more complex radiation sources, but also to enable asymmetric manipulations of the scattering matrix elements for the purpose of energy conservation enforcement, if desired.

4.4 MOMO Raman 2.0

While the focus of code versions 1.0 and 1.1 had been to enable the computation of accurate water Raman contributions to the radiation fields in the ocean-atmosphere system, the following development focused on the execution speed of the model. New projects, that required to compute large numbers of cases due to a high dimensional parameter space (e.g. the five separate parameters in the bio-optical model featured in the SIOCS project introduced in section 6.4), were the main reason for these efforts.

The transition from the debugging friendly loop based approach for the source operator computation in code versions 1.0 and 1.1. to the matrix operator approach (equations 2.19) and a more efficient spectral averaging (equations 2.16 and 2.17) significantly improved the computation time. Code version 2.0 produces identical results in terms of radiances and irradiances as version 1.1.

4.5 MOMO Raman 2.1

In code version 2.1 the option for exponential interpolation of the depth dependency of the Raman source within one homogenous model layer was added (equations 2.26), enabling accurate results in terms of Raman fractions even when sampling the ocean only with a small number of layers, which again decreased the execution time of a model run significantly. Validation efforts of this code version included the successful model intercomparison for the Raman case defined in Mobley et al. [73].

4.6 Further Developments

An implementation of a chlorophyll fluorescence preprocessor based on the approach showed in section 3.2.5 had been performed in an early version of the MOMO code by Fischer et al. [29]. A description can be found in [26]. This model version was based on the assumption that $\mathbf{J}_{12}^{C+} = \mathbf{J}_{01}^{C+} = \mathbf{J}_{21}^{C-} = \mathbf{J}_{10}^{C-}$ within the doubling algorithm and therefore required to determine an average value of $\mathbf{J}^{Cele}$ which was representative for a whole model layer, comparable to the *doubling* approach for Raman scattering in the initial version of MOMO Raman (1.0). It was therefore necessary to increase the number of model layers in the ocean to get accurate results. The fluorescence code was furthermore limited to the input of isotropic sources. The new MOMO Raman code in the version 2.1 now allows to include isotropic as well as angular dependent fluorescence sources. Furthermore, the new implemented approach for the source *doubling* described in section 2.11 will allow to decrease computation time and increase accuracy for fluorescence computations and to combine fluorescence and Raman scattering effects in one model run.

Based on code version 2.1, subroutines to compute the scattering cross sections of atmospheric rotational Raman scattering (RRS) by nitrogen and oxygen molecules have been developed, following the method in section 1.5. The number density of the molecules, computed from the pressure in each atmospheric model layer, allows to derive the corresponding RRS volume scattering functions which are a necessary input for the RRS source term generation. An integration of the latter into MOMO Raman is an ongoing project.

Furthermore, an integration of polarization resolved ocean Raman scattering effects by members of our research group into the vector Radiative transfer code of Hollstein and Fischer [44], following the algorithm of MOMO Raman 2.1, is in the testing stage.

Chapter 5

Model Validation

5.1 Introduction

Different general approaches exist to verify the correctness of the radiometric quantities predicted by a numeric radiative transfer model. The validation by the proof that the model predicts the correct values for a quantity directly measurable for a variety of scenes would surely be a generally accepted verification method. Unfortunately, since an accurate and complete data set of the optical properties of the atmosphere and ocean for every scene is required as model input for such an approach, this type of validation is rarely accomplished with a satisfying accuracy given the existing technical limitations for the measurement of the necessary data sets. Furthermore, the residuals between a model prediction and the measurement may to some unknown extent originate from uncertainties of the model input data. Nevertheless, this type of approach is e.g. helpful for qualitative studies of the behavior of a model in its entirety, including all preprocessors that generate the input for the radiative transfer model, and may become more significant in the future as the available technology for the IOP measurements advances. Another method for validation is the comparison of the model output analytical solutions of the radiative transfer problem. While this method enables conclusions on the correct function of the model for this specific simple case (e.g. a purely Rayleigh scattering atmosphere), it does not enable to state the correctness of those functions of a model that were not required for this specific output generation. This explains why certain functions and the general behavior of the scalar MOMO model could be validated with the latter approach, whereas the correct treatment of inelastic scattering processes in the MOMO Raman code version could not have been tested the same way due to the lack of accurate analytical solutions. Finally, model comparisons can be performed for well defined test cases.

A stepwise strategy was applied to ensure the proper operation of the MOMO Raman model. During the development process, in addition to a careful debugging of every new or altered model routine, sanity checks including the assurance of the independence of the radiometric output on internal model parameters, such as the angular or the vertical model resolution. Energy conservation tests were also considered for simple cases. For realistic

Raman spectra however, due to trans-spectral nature of the process resulting in changes of energy in both the excitation and the emission band, the latter is challenging. In addition, the numeric compliance of the model output for elastic scattering cases with the previously validated scalar MOMO model [26] was ensured after every change to the core routines of the code.

After completion of the code, the validation efforts were based on the application of the model to different problems and comparing the output to the output of other existing models. Due to the lack of generally available reference models that featured a coupled ocean-atmosphere system and included Raman scattering in a quantitative manner, including the azimuthal dependence and all spectral features, our model settings were adapted to correspond to the capabilities of the available reference models. The initial MOMO Raman 1.0 version was compared to the commercial ocean radiative transfer model HydroLight 5.3.1 model with promising results, presented in section 5.3. After the new versions of both MOMO Raman (2.1) and HydroLight (5.4) had previously undergone further debugging efforts that also affected the model outputs (see section 4.3), a new model intercomparison was undertaken. In this case we compared the output of MOMO Raman 2.1, for a canonical test case which includes Raman scattering, to the output values of four Monte Carlo radiative transfer models (listed in Mobley et al. [73]) with excellent agreement. Details are presented in section 5.3. A generally very good agreement to other published values (e.g. in [35]) for more realistic cases was also found. Very recently, further validation efforts were undertaken with Vladimir Rozanov and Tilman Dinter of IUP Bremen with a new version of there radiative transfer model SCIATRAN that includes Raman scattering, i.a. showing a very good agreement for the test cases defined in [73] and [132], which will be included in an upcoming publication.

The latter efforts, together with a qualitatively very good agreement to the behavior expected in terms of depth-, angular- and turbidity- dependence of the Raman scattered radiance fraction (presented in chapter 6), lead to the certainty that with MOMO Raman in the version 2.1 we have a fast model that quantitatively correctly accounts for the effects of vibrational Raman scattering of liquid water in the ocean-atmosphere system. Driven by the good first experiences made with the MOMO Raman model regarding the retrieval of oceanic constituents from satellite images, as discussed in section 6.4, future plans for validation include efforts based directly on ocean color measurements at reference sites, including parameters from databases such as MERMAID [5].

5.2 Model Intercomparison of MOMO Raman 2.1

A collection of seven well defined canonical problems as a basis for the comparison of seven different ocean radiative transfer models and a discussion of the results has been released by Mobley et al. [73] in 1993. The latter has i.a. been a basis for the validation of the initial scalar MOMO model [26]. Four of the featured Monte Carlo (MC) RT models were able to account for Raman scattering then. Canonical *Problem 7* in the publication is the only case which includes inelastic scattering and therefore was used for the MOMO Raman

Depth (m)	Gordon	Kattawar	MOMO Raman	Morel & Gentili	Stavn
E_d :					
0	0.01875	0.01874	0.01877	0.01739	0.01873
50	0.02489	0.02488	0.02492	0.02470	0.02490
100	0.01136	0.01136	0.01139	0.01123	0.01138
E_u :					
0	0.03532	0.03512	0.03518	0.03478	0.03523
50	0.01034	0.01042	0.01039	0.01027	0.01039
100	0.00287	0.00296	0.00298	0.00292	0.00296

Table 5.1: Upwelling and downwelling vector irradiances for a canonical test case ("Problem 7" from Mobley et al. [73]) for four MC models and MOMO. Units are those of the featured solar irradiance, which is set to 1.

output comparison.

Some adaptions of the MOMO default settings were necessary to resemble the simple test case. The excitation wavelength is set to $\lambda' = 417nm$ and the emission wavelength is $\lambda = 486nm$. Instead of the actual spectral redistribution, all Raman scattered radiation is shifted from λ' to λ. No atmospheric extinction is present. The solar vector irradiance is set to 1 at λ' and to 0 at λ and the solar zenith angle is 60°. The water absorption and elastic scattering coefficients are taken from Smith and Baker [109]:

$$\begin{aligned} a(417nm) &= 0.0156m^{-1}, \\ b(417nm) &= 0.0063m^{-1}, \\ a(486nm) &= 0.0188m^{-1}, \\ b(486nm) &= 0.0032m^{-1}. \end{aligned}$$

Due to the reasons discussed in section 1.3.8, the absorption coefficients are assumed to already include the absorption due to Raman scattering. The air-sea interface is assumed to be flat. The ocean in the MC models was set to be infinitely deep. Due to the required assumption of a finite ocean depth in MOMO, it was set to $500m$ there.

The four Monte Carlo models whose outputs are documented in [73] and therefore available for comparison are:

1. The model of H. R. Gordon based on the principals found in [36, 33],
2. The model of G. Kattawar [132],
3. The model of A. Morel and B. Gentili (See [73] for a description and e.g. [36] for a similar approach),

4. The model of H. Stavn (See [73] for a description and e.g. [36] for a similar approach).

The results in terms of upwelling and downwelling vector irradiances at different depths are displayed in tabular 5.1. Clearly there is an excellent agreement between all MC models and MOMO. Differences between the model outputs can mostly only be found from the third or even fourth significant digit onward, including the MOMO results. An exception is the Morel & Gentili model, which exhibits slightly lower values than the other models. While the three MC models with nearly similar results (models 1., 3. and 4.) are based on the same principles for the solution of the radiative transfer equation and were executed with similar settings in terms of angular resolution etc., the good agreement of the MOMO Raman results to the latter can not be attributed to the model similarity, due to its fundamentally different matrix-operator approach.

5.3 Model Intercomparison of MOMO Raman 1.0

In the following, the efforts for the validation of the initial MOMO Raman 1.0 version by comparison of the output for test cases to the commercial ocean radiative transfer model HydroLight are discussed. These efforts were performed by the author of this thesis within the framework of the ESA funded *support to science* project WaterRadiance and the following sections about the model comparison are a slightly edited version of the original project report (von Bismarck and Fischer [124]) and have been accompanied with a few new remarks in square brackets here.

5.3.1 Introduction

MOMO is a computer code, based on the matrix-operator method, to calculate the light field in the stratified atmosphere-ocean system which was developed at the Institute for Space Science of the Freie Universität Berlin. Within the framework of the ESA WATERRADIANCE Project, two new versions of the code have been developed to enable polarization resolved simulations, and the incorporation of water Raman scattering effects. The following sections describe the validation efforts of the results computed with the latter version of the new MOMO code.

With the exception of approximative estimation formulas for the maximum Raman contribution to water leaving irradiances (i.a. [129]), no complete analytical solutions of the radiative transfer equation are available for a realistic water body including Raman scattering effects. Therefore the commercial water-body radiative transfer code HydroLight is supposed to serve as a validation reference, since the code is also a basis for the remote sensing algorithm development within the project framework.

5.3.2 MOMO-Raman

MOMO is a computer code based on the matrix-operator method, designed to calculate the light field in the stratified atmosphere-ocean system. It has been developed at the Institute

for Space Sciences of the Freie Universität Berlin and provides the full polarization state (in the newest version described in [45]) and an air-sea interface accounting for radiative effects of the wind roughened water surface. The detailed description of the implementation and validation of the original scalar model version can be found in [31] and [26].

The inclusion of Raman scattering effects in a new code version required to establish a new processing scheme, since the radiance due to Raman scattering emitted at a single wavelength depends on the light field at all the contributing excitation wavelengths. Therefore multiple model runs are necessary for a single output. This is accomplished by a processing module, that starts a primary MOMO program run with a high spectral resolution, to calculate the radiative energy available for inelastic scattering at each model layer boundary. The processing module then calculates the first order Raman source-terms for every observation wavelength at every layer boundary, accounting for the non-isotropicity (and by default including the azimuthal dependence) of the Raman phase function, the spectral redistribution, and the spectral dependence of the Raman scattering coefficient. These elementary source-terms then serve as input for the second program run, which then calculates the source-terms of all model layers, using the doubling-adding method, and the resulting radiance field. Higher orders of the Raman contribution can be computed with additional program runs on demand. Apart from the Raman source, the MOMO program structure allows the inclusion of other elastic and inelastic sources, e.g. fluorescence. A detailed description of the physical background and the implementation of the algorithm can be found in [45].

5.3.3 The Reference Model HydroLight 5.3

HydroLight is a radiative transfer code package for the computation of radiance distributions of stratified natural water bodies [65]. The radiative transfer equation is solved by the use of invariant imbedding techniques described in [73]. As MOMO, the code also includes a module for the treatment of the wind roughened water surface.

Since the radiative transfer is not performed for the atmosphere, incoming irradiances at the sea surface may be calculated by the integrated atmospheric extinction model RADTRAN-X [71], if desired. To account for the angular distribution of the sky radiance, a simple integrated semi-empirical sky model is available within HydroLight. The newest version of HydroLight, 5.3.1, which was used within this validation process, offers the possibility to provide incoming irradiances at the sea surface, and to define the fractions of direct and diffuse radiation in a text file.

Raman scattering and other inelastic scattering effects can optionally be included in HydroLight model runs. The appropriate exciting bands (as well as the appropriate band spacing) then have to be included manually. Although an azimuthal averaged Raman scattering phase function is discussed in [67], a more simple approach, with the main focus on accurate results for irradiances, seems to have been implemented to limit computation time (see section 5.3.7 for details) in the present version.

5.3.4 Case Definition for the Model Intercomparison

The biggest difference between the input of MOMO and the reference Model is a consequence of the missing of an atmosphere in HydroLight: Since in MOMO the intensity, the spectrum, and the angular distribution of the light field entering the ocean depend on the propagation of Sun light from the top of the atmosphere through the atmosphere, the only way for an exact model comparison was to set scattering and absorption within the atmospheric layers to zero.

The computations were carried out from 330nm to 700nm in a 1nm grid. Due to the spectral shift in Raman scattering, this leads to usable output values between 400nm and 700nm. For simplicity the incoming solar irradiance in both models was set to one for the whole spectral range covered by the computations.

The clear water IOP were provided by the standard model used in Hydrolight 5.3.1 on a 5nm grid and linearly interpolated to the 1nm grid in both models, -no further constituents were added. A flat surface was assumed, and the refractive index of the water was set to 1.34. The number of zenith angles in MOMO was set to 27 within the water body.

Since MOMO calculates the Raman excitation energy for each distinct model layer, the accuracy of the resulting light field with respect to Raman scattering can depend on the thickness of the layers. In spectral regions with very strong absorption, as in the red and NIR, thin model layers are therefore required to achieve accurate values for water leaving radiances. For the validation, a thickness of 1cm was chosen for the first 10cm, a grid of 10cm for the following 90cm, a grid of 1m for the following 9m and a grid of 10m for the following 90m. The bottom was set to a depth of 100m with a reflectance of 0. *[The latter limitations only apply to code version previous code versions, the present MOMO Raman code version 2.1 does not require the consideration of several homogeneous layers to produce accurate results in terms of the in-water light field (see chapter 4 and results in section 6.2.5).]*

MOMO uses a Raman scattering phase function with a depolarization ratio of $\rho = 0.17$ by default:

$$P^R(\theta) = \frac{3}{16\pi}\frac{1+3\rho}{1+2\rho}\left(1+\frac{1-\rho}{1+3\rho}\cos^2\theta\right). \tag{5.2}$$

In MOMO, the azimuthal dependence of the phase functions is Fourier decomposed and the RTE is then solved in Fourier space. Generally, the Fourier decomposition of the azimuthal dependent Rayleigh and Raman phase functions require 3 terms. Since HydroLight does not account for the azimuthal dependence of Raman scattering, the second and third Fourier term of the Raman scattering function in MOMO were set to zero for validation purposes, resulting in azimuthal averaging of the Raman source. For comparison to the HydroLight radiances, the MOMO computations were additionally carried out with an isotropic Raman phase function, as well as a Raman phase function similar to the one for elastic (Rayleigh) scattering in the water.

The Raman absorption coefficient follows a power law:

$$\beta^R_{abs}(\lambda') = a^R_0(\lambda'_0)\left(\frac{\lambda'_0}{\lambda'}\right)^n. \tag{5.3}$$

Values for a^R_0 in the Equation 5.3 for the Raman absorption coefficient in literature show big variations in older publications. Measurements in the past two decades, however, show a much better accordance[105, 67]. For this validation, the MOMO computations ran with the values $a^R_0(\lambda'_0 = 488nm) = 2.4 \cdot 10^{-4} m^{-1}$, as in HydroLight, and $n = 4.8$.

The main quantities of interest, computed by a radiative transfer model of the ocean for remote sensing applications, are water leaving irradiances and radiances. The validation of the MOMO-Raman results in this report is based on the comparison of light fields within the water body computed with the two models. In the treated case, with a flat interface between ocean and atmosphere, the upwelling radiation in the uppermost layer is proportional to the water leaving radiance.

5.3.5 Conventions and Definitions

Throughout the validation report, the same plot symbols and line-styles were used (see Figure 5.1) to distinguish results of the two different models, with or without Raman scattering, and results for the different Raman phase functions shown in some plots. If values of differences between both models are plotted, the line-style/symbols of HydroLight are used.

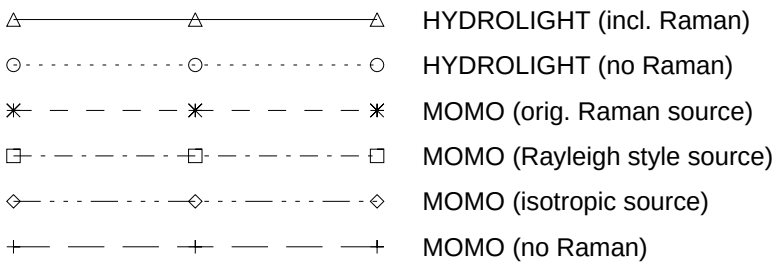

Figure 5.1: Legend with symbols and line-styles valid throughout the validation report.

When analyzing the sensitivity of measurements to Raman scattering effects, the Raman fraction of a radiation quantity often is of interest. Throughout this report the Raman fraction of a quantity is defined as the difference of the model results from runs with and without included Raman scattering effects, divided by the model result including Raman scattering effects.

5.3.6 Validation of MOMO with Elastic Scattering Only

The validation of the scalar version of MOMO, which was the basis for the new code that includes Raman scattering effects, is discussed in detail in [26] and [31]. Back then, the compliance of the results with analytical solutions for a Rayleigh scattering case was positively tested, and a model intercomparison for canonical test cases for water radiative transfer models published in [73] was successfully performed. The new MOMO-Raman code produces the same results as the originally validated code version, if Raman scattering is turned off. Therefore a detailed discussion of the validation of the results for the elastic scattering case can be omitted in this document, although in some plots in the following sections, results of the elastic scattering model runs are shown together with the results including Raman scattering for completeness.

5.3.7 Intercomparison of MOMO and HydroLight with Raman Scattering

Irradiances

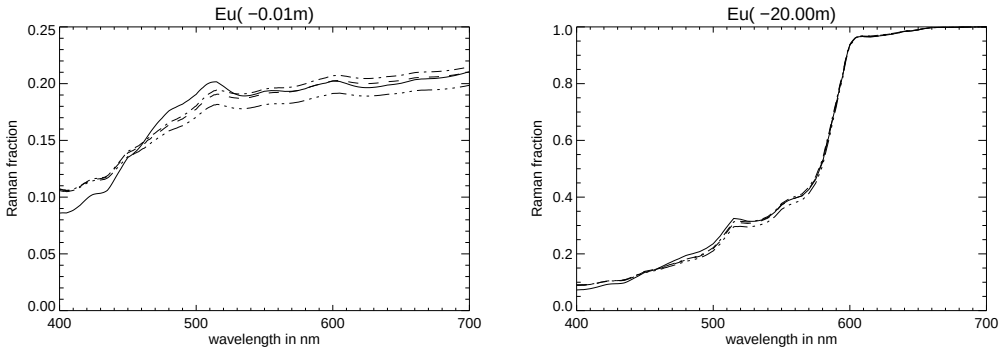

(a) (b)

Figure 5.2: Raman fraction in the upwelling irradiance at two different geometrical water depths. The solid line stands for the HydroLight results and the dashed line for the MOMO results. The mixed dashed and dotted lines stand for MOMO results with different Raman scattering phase functions (see legend in figure 5.1).

In this section the results of the model intercomparison for upwelling irradiances are discussed. Figure 5.2 shows the overall good agreement of the Raman fractions computed by HydroLight and by MOMO. Small scale spectral features present in the emission wavelength have a slightly stronger impact on the HydroLight results (for instance the hump in figure 5.2 (b) at 510nm). This difference may be due to the way, the spectral redistribution of Raman scattered light is implemented in the models. In MOMO, the light from a single emission wavelength is not scattered to a single wavelength, but spread out using the spectral redistribution function defined in [126, 127, 42], leading to a spectral smoothing of

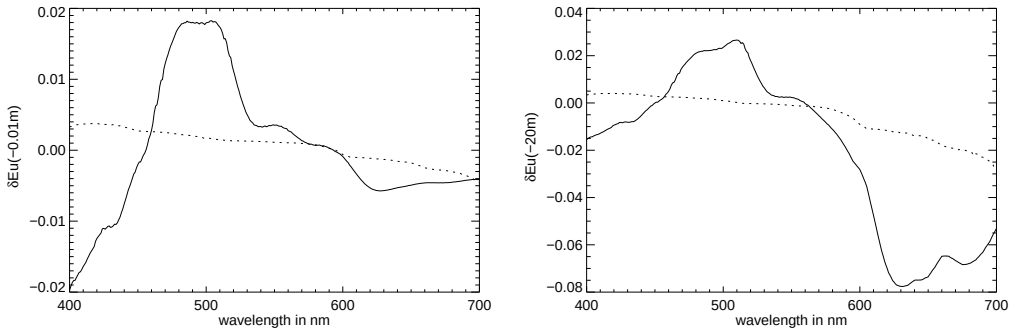

(a) (b)

Figure 5.3: The relative difference of upwelling irradiances between the models including Raman scattering (dotted line) and without Raman scattering (solid line).)

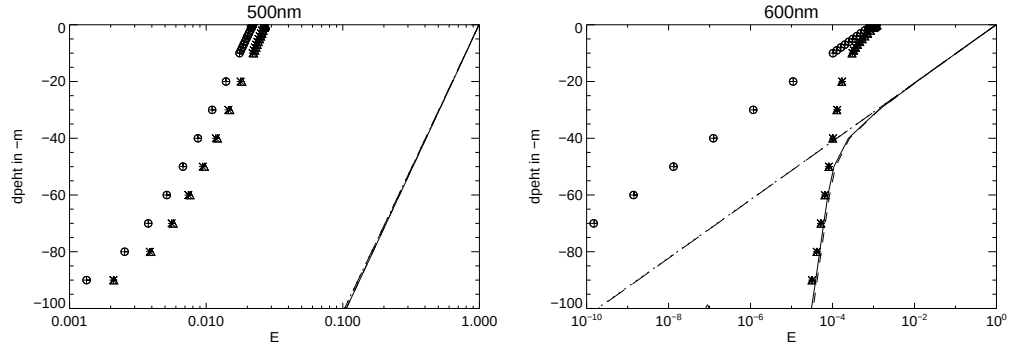

(a) (b)

Figure 5.4: The geometrical depth dependency of the Raman fraction in the irradiances. The lines stand for downwelling-, the symbols for upwelling irradiances. The legend can be found in figure 5.1.

features in the emission spectra. This might also bee the reason for the slightly higher values of MOMO at 400nm. The best accordance between the models is reached in the red, if MOMO uses the actual Raman phase function (dashed lines). An isotropic Raman source produces lower values than HydroLight, and a Raman source using the elastic Rayleigh scattering function leads to slightly higher values than HydroLight in the red. In figure 5.3, the relative difference of the upwelling irradiances of both models is plotted. Directly beneath the surface, the maximum difference with included Raman scattering is about 2%. At a water depth of 20m the differences in the red reach values of nearly 8%. In this water depth rather thick model layers (10m) were defined for the MOMO computations, in favor of a fast computation time and a good depth resolution directly below the surface (0.01m), where the influence on the water leaving irradiance is higher. This leads to a decrease of accuracy of the MOMO-Raman results with depth in strongly absorbing spectral regions, due to reasons discussed in section 5.3.4. The overall still good agreement of both models

for the whole depth range, also for downwelling radiances, can be seen in figure 5.4 exemplary for 500 and 600nm. In the red, where water absorption is strong, Raman scattering is the main light source in big water depths.

The depth dependency of the absolute differences of the Raman fraction of E_u in the visible range from values between 0 and 0.03 at the surface (positive values indicating higher MOMO values) and between 0 and -0.03 at a depth of 60m (figure 5.5). In most regions, however, the difference is smaller than 0.01 (1%). At depths, where the model layer thickness gets bigger, a step in the differences can be observed (for instance at 10m depth) due to the model layer thickness dependent accuracy in MOMO.

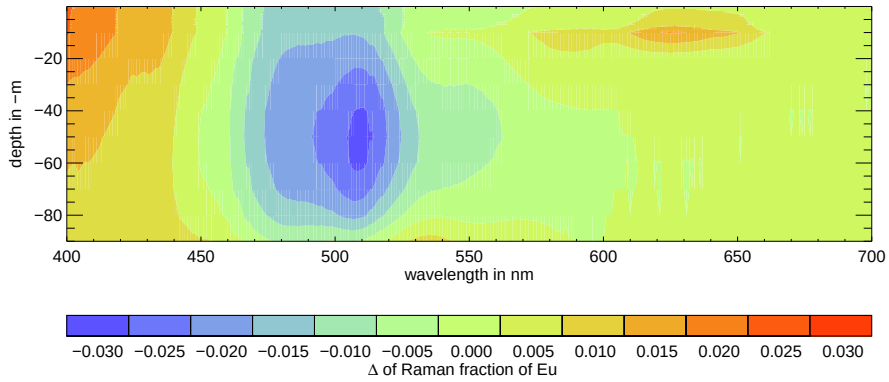

Figure 5.5: Geometrical depth dependency of the model deviation in units of Raman fraction.

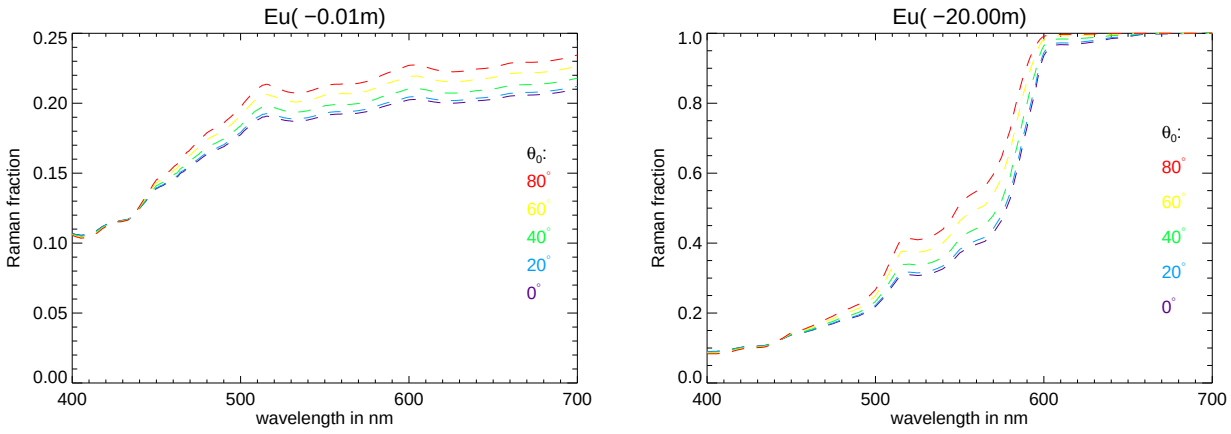

(a) (b)

Figure 5.6: MOMO Raman fraction in the upwelling irradiance for different solar zenith angles at two different geometrical water depths.

As can be seen in figure 5.6, the Raman fractions of the upwelling irradiances have only a weak dependency on the solar zenith angle. In the green and red spectral region, the

fractions decrease with the rising sun, whereas they grow in the blue. These trends in the MOMO values are in accordance to computation results of other models published by K. J. Waters and H. R. Gordon [35, 129].

Radiances

This section discusses the differences in angular dependence of the radiances computed by the models. Radiance at an angle of 0° in the plots in this section is heading directly down into the water, whereas radiance at an angle of 180° is heading directly upward.

For the elastic scattering case, both models agree very well (plus signs and circles in figures 5.7 (a)-(f)). In the case with Raman scattering inclusion, however, a perfect agreement of the MOMO and the HydroLight results in terms of angular dependence can not be expected, due to a computation time efficient approach implemented in HydroLight, in favor of an exact modeling of the angular redistribution[68].

The angular distribution of the HydroLight-Raman radiances is generally more pronounced than the one of the MOMO radiances. However, the trends are similar, with the maximum Raman contribution lowest at the 90° angle, and local contribution maxima at 0° and 180° with tho global maximum being at 0°. From the three different Raman phase function tested in MOMO, the Rayleigh type phase function shows the strongest angular dependency, whereas the isotropic phase function shows the least angular dependency. The actual Raman phase function, which is less peaked than the Rayleigh phase function, leads to values in between the ones computed with the isotropic and the Rayleigh phase function, as was expected. Raman fractions of water leaving irradiances and water leaving zenith radiances are similar in the MOMO results and also in results published in [35], whereas HydroLight computes bigger Raman fractions for the zenith radiance.

The discontinuity of the MOMO values at 90° that can be seen in figure 5.7, plot (f), is a result of the big model layer thickness chosen in big depths to limit computation time for the model runs (see section 5.3.4, where the reason for this sampling phenomenon is discussed). *[The discontinuities are not present in results of MOMO Raman 2.1, due to a more sophisticated depth dependence treatment (see section 2.11 and chapter 4).]* The gap between the excitation energy, which is determined at every upper model layer boundary for the adjacent layer, is not negligible between two neighboring layers in this case. Since the weaker Raman source term of the lower layer has a strong influence on the upwelling light field at the boarder between the layers and vice versa, the resulting radiance, which is put together from separate matrices for the up- and downwelling radiances, has a gap at the 90° joint. This loss of accuracy with depth was implemented on purpose in favor of computational efficiency and highly accurate results near the surface and for water leaving radiances [1].

[1] If highly accurate simulations in the red and SWIR should be required for big depths, the model layer thickness can simply be decreased.

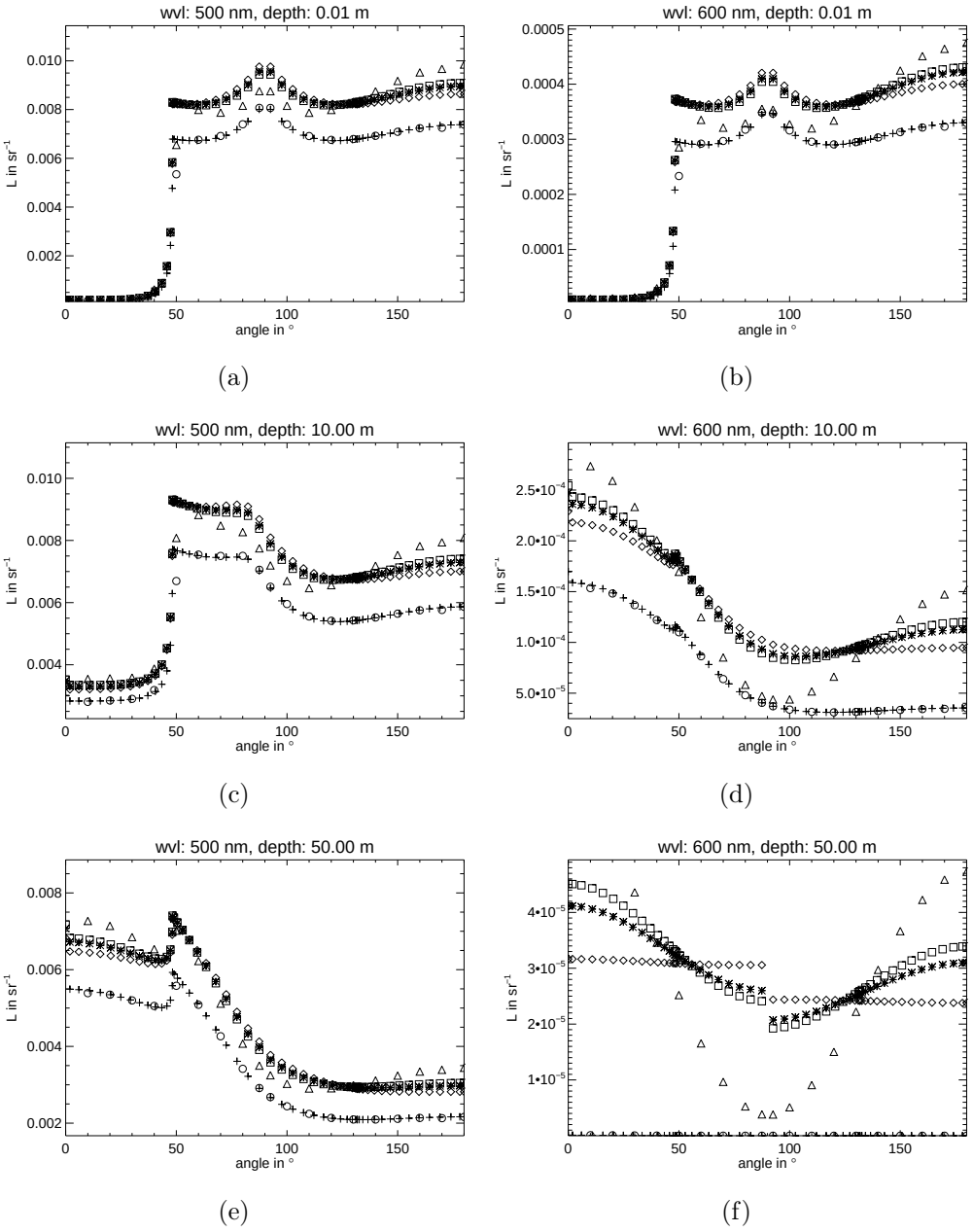

Figure 5.7: Angular dependency of the radiances at three different geometrical depths. 0° stands for the forward direction, 90° sideways scattered light, and 180° backward scattered light. The azimuth angle is set to 0°. The stars denote the MOMO results with Raman scattering, the pluses without. Diamonds denote MOMO results with an isotropic Raman phase function, boxes stand for a Rayleigh style Raman phase function. Triangles denote the HydroLight results with Raman scattering, and circles without. (See text for further descriptions.)

5.3.8 Conclusions

[These are the conclusions of the MOMO Raman 1.0 and HydroLight model comparisons. General conclusions of the MOMO Raman validation process, also of MOMO Raman 2.1, can be found at the beginning of this chapter.] The intercomparison of MOMO and HydroLight showed a very good agreement for the elastic scattering case, and also an overall good agreement for irradiances due to Raman scattering. Although both models showed the same trends in the angular dependency of the Raman fraction of the in-water radiances, the angular dependency is more pronounced in the HydroLight results. Due to the good agreement of the MOMO results with our expectations of the angular distribution of Raman scattered light, these differences should arise from the more accurate modeling of the Raman phase function in MOMO.

Chapter 6

Applications

6.1 Introduction

After the previous chapters described our approach to quantitatively incorporate the effect of water Raman scattering in a previously monochromatic radiative transfer model, this chapter shall introduce a number of applications that featured the new model, and discuss the results. An emphasis will be given on the effect of neglecting Raman scattering, with the idea of providing a general basis for the prediction for which type of remote sensing applications accurate Raman scattering effects are of significance, and were a simplified treatment of the latter or even the total neglect of the effect is appropriate, to save computation time.

A selection of sensitivity studies, as well as an ocean constituent retrieval processor which feature the new MOMO Raman RT model, will be introduced. The results of a general study of the effect of Raman scattering on the spectral terrestrial shortwave radiation distribution can be found in section 6.2. A separate study of the impact of Raman scattering effects on the signals measured by the ESA MERIS and the upcoming OLCI satellite imaging spectrometers is introduced in section 6.3. For quantitative computations of the radiation field for the diversity of global Case 1 and Case 2 waters and there application to an ocean constituent retrieval processor, it shall be referred to section 6.4 about the *SIOCS* project. Furthermore, for a very specific study about the errors induced when the azimuthal dependence of Raman scattering is neglected, our article in the IRS proceedings 2012, featuring the realistic bio-optical model 2 described in section 3.2.4, is recommended (von Bismarck and Fischer [121]).

6.2 Influence of Water Raman Scattering on the Terrestrial Light Field

This section shall demonstrate the capabilities of the previously introduced radiative transfer code regarding the quantitative inclusion of water Raman scattering effects. Further-

more it will point out the significance of water Raman scattering effects and their possible impact on remote sensing applications. The simulations were carried out with the newest code version 2.1. Rather than spectrally averaging the output and/or input to the actual bands of a satellite sensor, the simulations were carried out with a $1nm$ spacing for the complete visible spectral range to give a general and sensor independent overview. Furthermore, the impact of some optional performance enhancing simplifications in the treatment of Raman scattering to the model output will be discussed.

6.2.1 Definition of Radiation Quantities and Apparent Optical Properties

A focus in the results displayed in the following sections is on the so called Raman fraction of upwelling irradiances and radiances. The Raman fraction of a radiometric quantity X under consideration of s Raman scattering orders is hereby defined as :

$$\text{Raman Fraction } (X^{(s)}) := \frac{X^{(s)} - X^{(0)}}{X^{(s)}}, \tag{6.1}$$

where $X^{(0)}$ is the radiation when only elastic scattering is considered and therefore Raman scattering only contributes to the absorption in the water body, following the notation introduced in section 2.7. If not stated otherwise in the following study, then $s = 1$. If the Raman offset of a radiometric quantity X is shown, the absolute difference between the elastic and the Raman including case is meant:

$$\text{Raman Offset } (X^{(s)}) := X^{(s)} - X^{(0)}. \tag{6.2}$$

It shall be noted that the Raman offset may as well be computed by a model run at the emission wavelength with the solar irradiance set to 0, and which therefore exclusively accounts for the propagation of Raman scattered radiation determined from the Raman source term. In that case the model output $X^{(s)}$ is identical to the Raman offset above.

In contrast to the Inherent Optical Properties (IOPs) of the water body introduced in chapter 3, the so called apparent optical properties (AOPs) are *those properties that (1) depend both on the medium (the IOPs) and on the geometric (directional) structure of the radiance distribution, and that (2) display enough regular features and stability to be useful descriptors of a water body*[66]. AOPs should therefore not strongly depend on short scale temporal changes in the atmospheric composition, which excludes i.e. the downwelling irradiances and radiances from the list of possible AOPs, since they may be significantly influenced by passing clouds.

An AOP popular among the ocean color remote sensing community is the remote sensing reflectance, defined as the upwelling nadir water-leaving radiance $L_{wl}(\theta = 0°)$ divided by the downwelling vector irradiance $E_d(+0m)$ reaching the sea surface. The water leaving radiance L_{wl} (and irradiance E_{wl}) is defined as the upwelling radiance (or irradiance, respectively) just above the sea surface, minus the radiation reflected at the sea surface. Due to the coupling of ocean and atmosphere in MOMO, a separation of radiances

at a certain vertical position by there origin is not a standard output. To generate an output of water leaving radiances with MOMO two approximative approaches are implemented. Either the reflection at the sea surface is set to zero, which neglects the fact that a small fraction of radiation may have been reflected and then scattered back into the water body and out again. Or the upwelling radiance for a black ocean case is subtracted from the upwelling radiance above the ocean, where the small fraction of radiation that has been scattered at least once within the water body before reaching the surface from above by successive scattering events in the atmosphere still remains in the result. When keeping the zenith angle change due to refraction at the interface in mind, for a flat Fresnel surface the water-leaving radiance can also easily be derived from the subsurface upwelling radiance with $L_{wl} = L_u(-0m)t^F/n^2$, where t^F is the Fresnel transmittance (discussed in section 3.2.6) and n is the refractive index of water. Due to the approximative, though rather accurate, character of the water leaving-radiances computed by MOMO, in this general study we are mainly showing the Raman fractions of the upwelling irradiances $E_u(-0m)$ and radiances $L_u(-0m)$ (often referred to simply as E_u and L_u in literature) just below the sea surface, which resemble the errors introduced to E_u (and also L_u) if Raman scattering is neglected, and differ only slightly from the Raman fractions of E_{wl}. The use of a subsurface upwelling radiation quantity also minimizes the effects introduced by differing possible treatments of the air-sea interface, for the sake of comparability to the outputs of other RT models. The latter especially addresses the fact that, in contrast to the MOMO model of the coupled atmosphere-ocean system, some existing Rt models that include ocean Raman scattering are limited to the simulation of the radiative transfer within the water body, thus depending on a-priori assumptions of the radiation $L_d(-0m)$ reaching the water body from above and neglecting multiple scattering between the water body and the atmosphere.

In addition to the *irradiance reflectance* R or *hemispherical reflectance*, an AOP that is defined by:

$$R := E_u/E_d, \tag{6.3}$$

we also show the actual values of E and L, since they reflect the amount of radiation available fore remote sensing and, in case the values are given at the top of the atmosphere, the signal strength at the satellite sensor. Therefore we give these values in SI units rather then normalized to the spectral solar irradiance, as is popular for monochromatic RT model runs by setting the irradiance input at the top of the atmosphere (TOA) to 1. This shall also reflect that a solar irradiance spectrum is needed to compute the effects of Raman scattering, due to the differences of solar irradiance in the excitation and the emission band.

6.2.2 Test Case

Since the purpose of this study was a general overview of the effect of the model capabilities and the effect of water Raman scattering on the light field available for remote sensing, standard and average values reflecting typical rather than specific conditions were used as

input. In the following the specific input values for the model preprocessors and the RT model for the cases reviewed in this study are discussed.

Ocean Settings

The MOMO pre-processor described in 3.2.1 was used to determine the clear water absorption and scattering coefficients based on the methods described in Röttgers et al. [101] and Zhang et al. [136]. If not stated otherwise, a default temperature setting of $15°C$ and a salinity of $35PSU$ was chosen. While the salinity value can be seen exemplarily for open ocean cases with the exception of in land waters and arctic regions, the temperature value has been chosen simply as approximate mean global and seasonal value, although temperatures for specific regions and dates may differ up to $15°C$ from this mean. Absorption of radiation at a specific wavelength due to Raman scattering was, if not stated otherwise, considered to be included in the clear water absorption coefficients (also see discussion in section 1.3.8 and results in section 6.2.8). The ocean depth as default was set to 999m with model layer boundaries at depths of 0, 1, 5, 10, 50, 100, 500 and 999m, if not stated otherwise. Nevertheless, the complete water body was assumed to be homogeneous. The ocean bottom was simulated to be absolute absorbing.

As a default, the sea surface was simulated to be flat, with the model described in section 3.2.6. For the cases where a rough sea surface based on the model described in section 3.2.6 was used, the wind speed is highlighted. The refractive index of the ocean for the determination of the refraction at the sea surface was assumed to be 1.34.

For the qualitative simulation of average Case 1 water type conditions, the bio-optical model type 1 introduced in section 3.2.4, which depends solely on the chlorophyll concentration, was used, if a concentration of chlorophyll (a) is stated in a plot. For the Case 1 water simulations the chlorophyll a concentration was assumed to be valid throughout the bulk of the water body, with no depth dependence simulated. However, to emphasize on the maximum impact of Raman scattering, which is strongest in clear waters without absorbing components, the default water type in the following sections features no components other than pure salt water.

For the Raman scattering coefficient and the spectral exponent of it's decrease, the values published by Bartlett et al. [6] including error margins, as discussed in section 1.3.6 and 1.3.7, are used ($b^R(\lambda'_0 = 488nm) = (2.7 \pm 0.2) \times 10^{-4}m^{-1}$ and $n = 5.5 \pm 0.4$). As was discussed in the latter sections, a couple of recent publications position the Raman scattering coefficient rather close to the minimum of the error margins of the values published by Bartlett et. al., or even below. However, to give qualitative overview of the maximum impact of the Raman scattering effects on the upwelling radiation and due to the widespread use of the Bartlett et al. values we have decided to use them as default setting for this sensitivity study.

An overview of the absorption and scattering coefficients of the components associated to the water model settings is shown in figure 6.1.

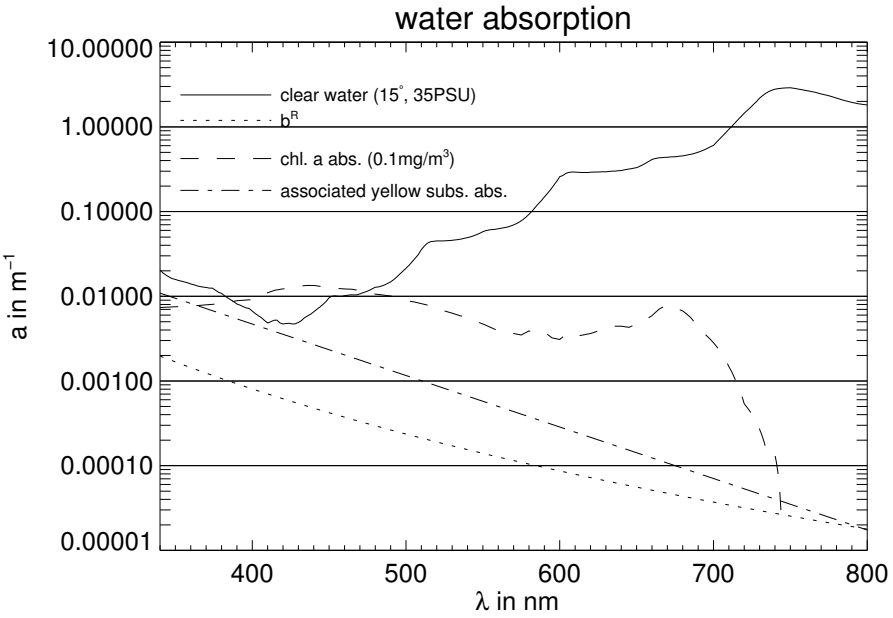

(a)

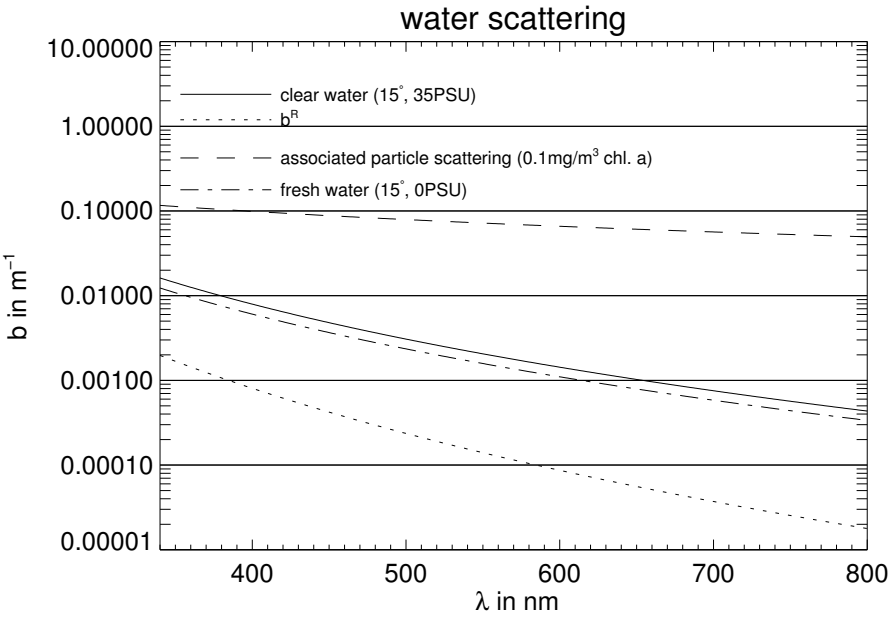

(b)

Figure 6.1: Absorption and Scattering coefficients of clear water at $15°C$ and $35PSU$ salinity, and the absorption and scattering components of the featured bio-optical model 1 for the approximate global average concentration in Case 1 waters of $0.1mg/m^3$. Furthermore the Raman scattering coefficient is displayed. The underlying model settings and the data sources can be found in the text of this section (6.2.2).

Atmospheric and General Settings

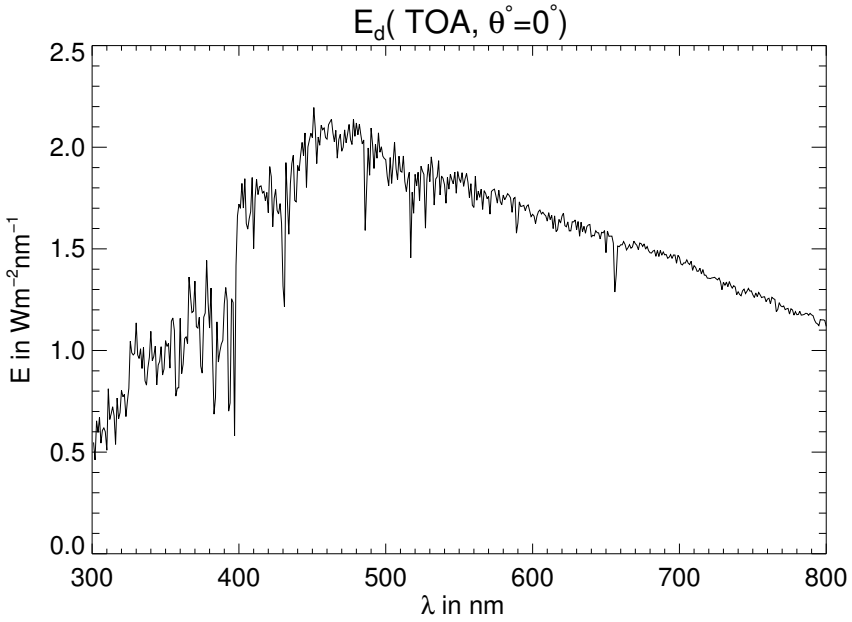

(a)

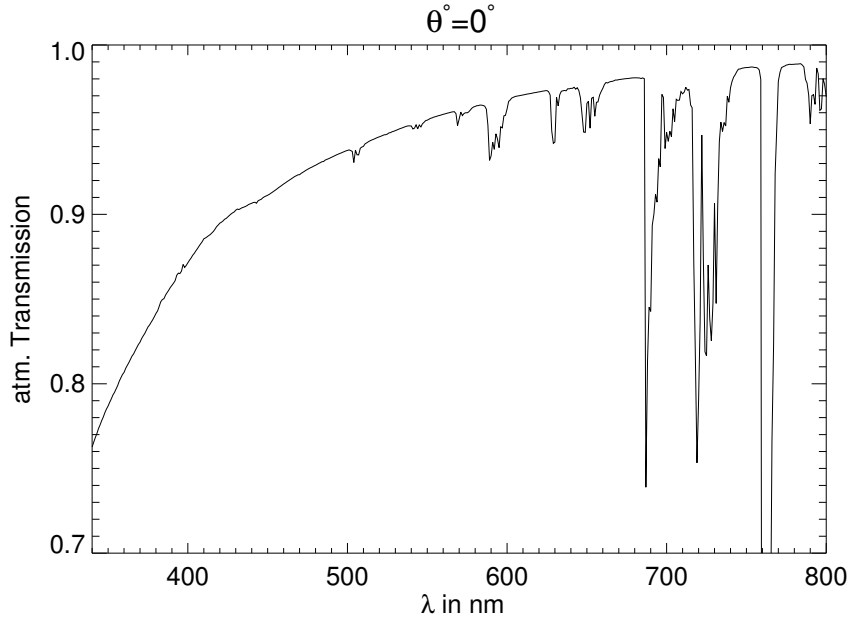

(b)

Figure 6.2: The atmospheric transmittance (b) and the extraterrestrial solar irradiance (a) used for the simulations.

Due to the dependence of the radiation at an observation wavelength on the available

radiation in the excitation band when Raman scattering is involved, the input of solar irradiance at the top of the atmosphere (TOA) can not be normalized to 1, as is often done in studies with monochromatic model runs. Therefore the high resolution solar spectrum of R. L. Kurucz [56], pre-averaged to the rectangular band shape of the used $1nm$ grid, was used (see figure 6.2(a)). No correction for the diurnal solar irradiance variations due to the earths orbital eccentricity for a specific date was undertaken.

Scattering and absorption in the atmosphere was simulated using temperature, pressure and water vapor profiles based on the U.S. Standard atmosphere [3]. The sky was assumed to be cloud and aerosol free. The absorption by atmospheric gases and trace gases in each $1nm$ band was computed with high accuracy using the k-distribution method [23] (see figure 6.2(b)). Rayleigh scattering was computed according to the pressure profile of the U.S. Standard atmosphere.

The radiative transfer computations were carried out with a sufficiently high number of zenith grid points for each application, meaning approximately 15-30 for the computation of irradiances and mostly 50-80 for the computation of radiances. The higher numbers of angles were used within the water body to fill the gaps produced by the refraction of downwelling radiation into the Fresnel cone. Rather than interpolating to integer values, the results are displayed at actual native grid point positions in terms of solar zenith angle θ° and observation zenith angle θ. If not stated otherwise, results for a solar zenith angle of 44.21° are displayed, representing an approximate median value of the solar elevation. Fourier decomposition of the azimuthal dependence was carried out with the first three coefficients in clear waters, but up to 100 coefficients in turbid waters to enable accurate sampling of the peaked particle scattering phase function.

The spectral output grid was set to a $1nm$ spacing from $330 - 800nm$. However, due to the spectral shifts introduced by each Raman scattering event, some output variables will only be displayed starting from a wavelength of $400nm$ or even larger.

6.2.3 Raman Scattered Fraction of the Upwelling Radiance and Irradiance

The Raman scattered fraction of the upwelling irradiance in clear sea water is a good qualitative measure for the upper threshold of the error introduced to a simulated signal, if the effect of Raman scattering is neglected. Figure 6.3(a) shows the Raman fraction of E_u and the error margins introduced by the assumed uncertainties of the used Raman scattering coefficient. Even though carried out with a slightly different Raman model, a generally very good agreement with the spectrally lower resolved values in Gordon [35] (Fig. 4.) can be observed, although the latter Monte Carlo model did not account for atmospheric absorption and therefore missed some of the fine structured spectral features. The earlier Monte Carlo results of Waters [129] show values which are a few percent lower, with some slightly different spectral features which may to some extent originate from his simpler Raman spectral redistribution model with static shifts of $3400cm^{-1}$, and possibly spectral averaging.

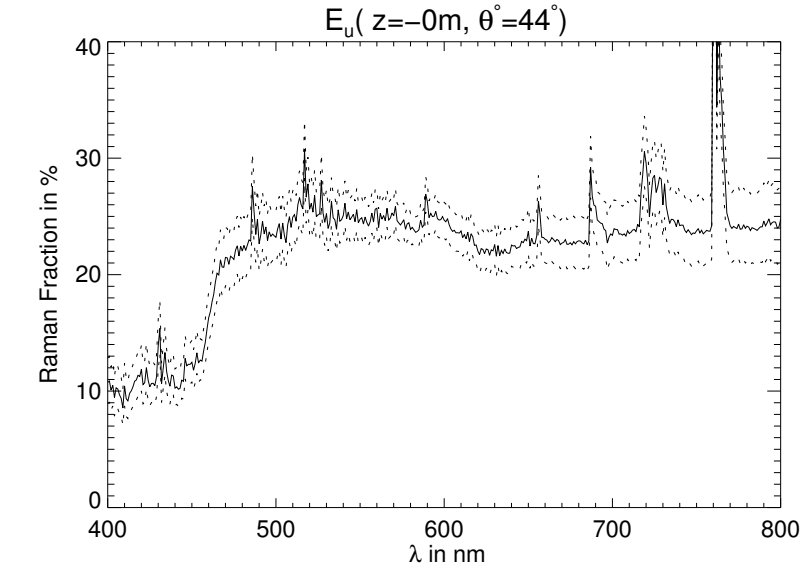

(a)

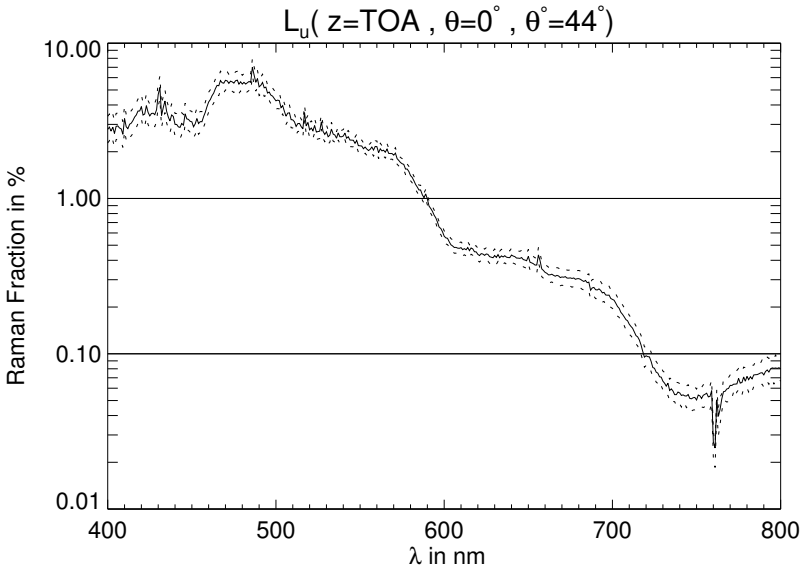

(b)

Figure 6.3: Clear sea water Raman fractions of the upwelling irradiance E_u just below the sea surface and the upwelling radiance L_u in zenith direction at the top of the atmosphere. The dotted lines mark the error margins of the underlying Raman scattering coefficient and spectral exponent. The solar zenith angle is 44.21°.

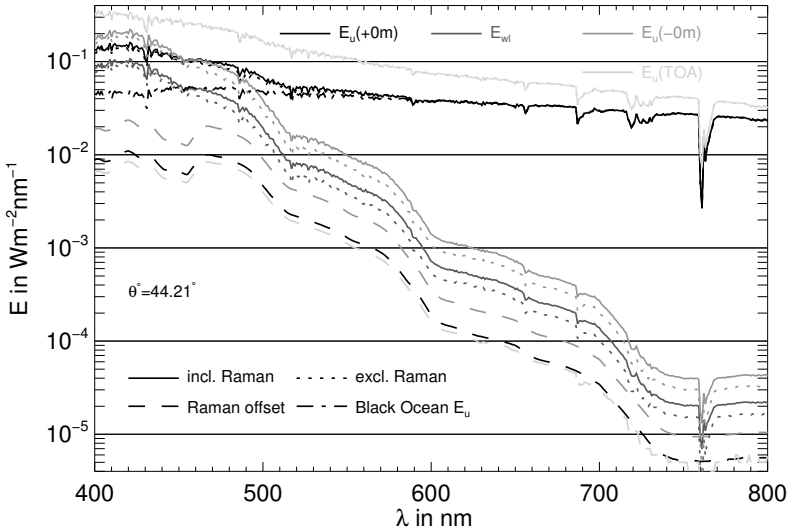

(a)

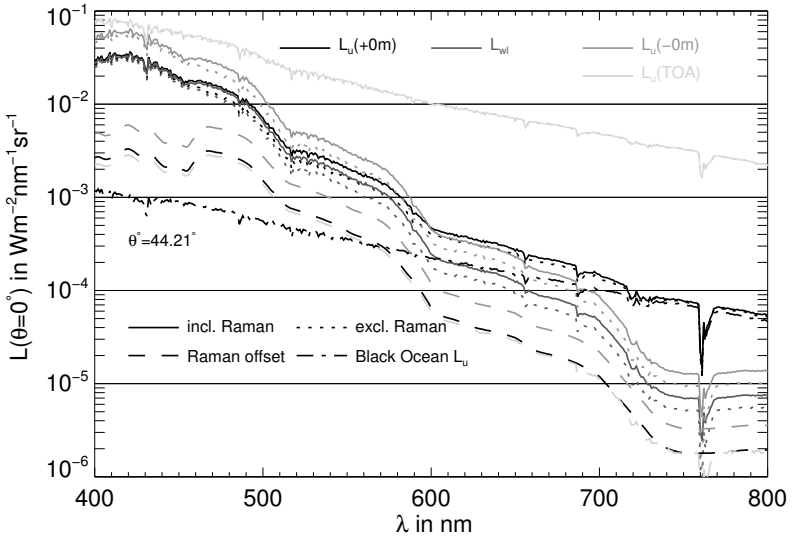

(b)

Figure 6.4: Upwelling irradiance (a) and nadir radiance (b) at the top of the atmosphere and just below the sea surface as well as the water leaving irradiance and radiance for a solar zenith angle of 44.21° for pure sea water. The quantities are shown including Raman scattering effects and excluding the effect. Furthermore the difference between the latter two values is shown (Raman offset). The results for a black ocean are shown to illustrate the amount of radiation that has not interacted with the water body, excluding the reflection at its surface.

While average values start at around 10% in the blue spectral region and stay at a high value of approx. 25% from the green throughout the rest of the visible spectral range, spikes of up to over 80% are present due to line filling effects in atmospheric absorption bands with the highest peak in the considered spectral region in the O_2 A-band. However, the error margins clearly demonstrate the necessity of precise measurements of the Raman scattering coefficient for the accurate simulation of the ocean color, since with the underlying coefficients absolute errors of up to 5% seem possible.

Due to atmospheric backscattering and absorption, at the top of the atmosphere the overall signal fraction coming from the ocean is roughly an order of magnitude lower than the atmospheric fraction in the visible spectral range (decreasing with growing wavelength). Therefore the Raman impact is also less strong at the top of the atmosphere (figure 6.3(b)). Here, the spectral. behavior is the other way around. Raman fractions of over 2%, with a maximum of about 6% in the radiances in zenith direction, are only reached in the blue and green spectral region. This is mainly due to the fact, that so little radiation leaves the water body due to the increasingly strong absorption of water throughout the red spectral region. However, this still means that up to 6% of the signal in spectral regions of interest for satellite ocean remote sensing has been Raman scattered. It shall be noted that no solar light reflected directly by the surface has been taken into account in the plot, since the ocean was simulated to be flat and therefore the emergent zenith angle of the reflected radiation equals the solar zenith angle, hence no radiation is reflected in zenith direction.

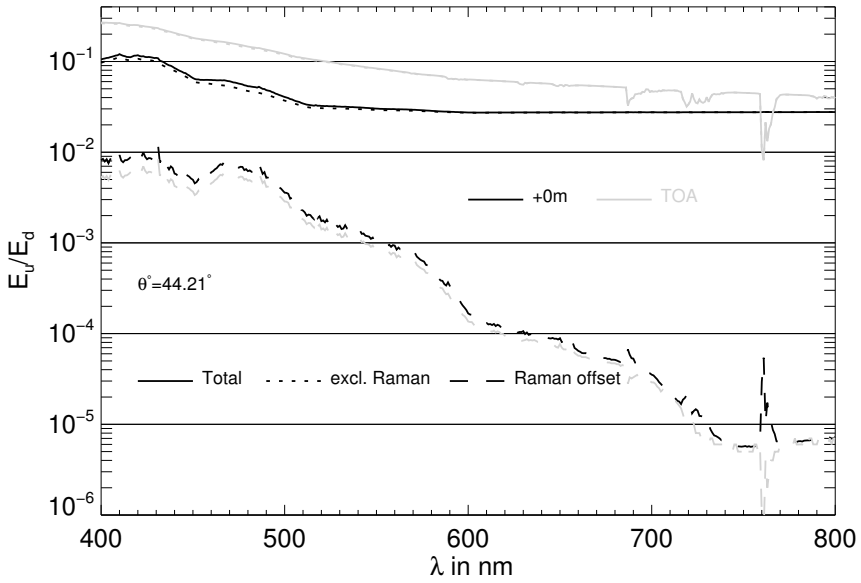

Figure 6.5: The irradiance reflectance and irradiance reflectance Raman offset of pure sea water, just above the sea surface and at the top of the atmosphere.

Figures 6.4(a) and 6.4(b) show the absolute impact in terms of hypothetical sensor signal strength due to Raman scattering effects in SI units, again for pure sea water. The

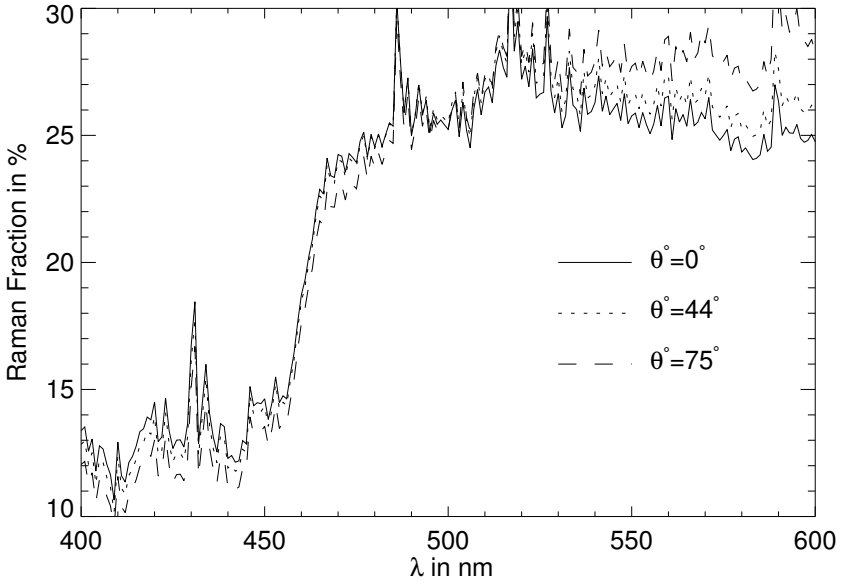

Figure 6.6: The Raman fraction of $E_u(-0m)$ in clear sea water, for three different solar zenith angles.

effect both at the sea surface and at the top of the atmosphere is strongest between 400 and $500nm$ and then decreases steadily for longer wavelengths. The offset between the water leaving radiation and the total upwelling radiation, qualitatively being the amount of radiation that is reflected by the surface, is approximately displayed as *Black Ocean* $E_u(+0m)$ and $L_u(+0m)$. For the displayed solar zenith angle of 44.21°, the nadir Raman radiance at the top of the atmosphere is stronger than the radiation reflected from the sea surface up to about $570nm$. However, the offset between the total upwelling vector irradiance above the surface $E_u(+0m)$ and the water leaving irradiance E_{wl} is much greater than the offset between the upward nadir radiance above the surface $L_u(\theta = 0°, +0m)$ and the water leaving nadir irradiance $L_{wl}(\theta = 0°)$, because the fraction of direct solar radiation that is reflected at the sea surface is present only in $E_u(+0m)$. L_u) on the other hand contains no direct solar reflected radiation, due the Fresnel type flat surface, independently of the solar zenith angle.

The irradiance reflectance Raman offset displayed in figure 6.5 shows a comparable spectral decrease. Here the atmospheric absorption line filling effects due to Raman scattering in the water above the sea surface are apparent (e.g. in the O_2A-Band at about $762nm$). At the top of the atmosphere, however, the signal is again weakened by the atmosphere and the line filling effect, and hence replaced by a dent in the Raman signal. Figures 6.17 and 6.16(b) show the same quantities as 6.4(a) and 6.5 for a Case 1 water body with a chlorophyll concentration of $0.1mg/m^3$. The values for a black ocean in the figures give the approximate fraction of radiation that has not interacted with the water body, but only with the sea surface and the atmosphere, and hence does not contribute to

the ocean color signal fraction observed at a sensor.

The solar zenith dependence of the Raman fraction of $E_u(-0m)$ is rather weak. In figure 6.6, the Raman fraction is shown for solar zenith angles of 0°, 44.21° and 75°. While there is a pivotal point at $\sim 495nm$, where all functions have the same value, the values are decreasing for growing zenith angles when moving to shorter wavelengths and increasing when moving to longer wavelengths, in comparison to the values for the sun in the zenith. The maximum absolute difference between the values for 0° and 44.21° are only about 1%. It shall be noted that solar zenith positions are given in atmospheric angles rather than their ocean counterparts which differ from the latter due to refraction at the sea surface. The solar zenith dependence is in agreement with the trends of Gordon [35] and Waters [129].

6.2.4 Multiple Raman scattering

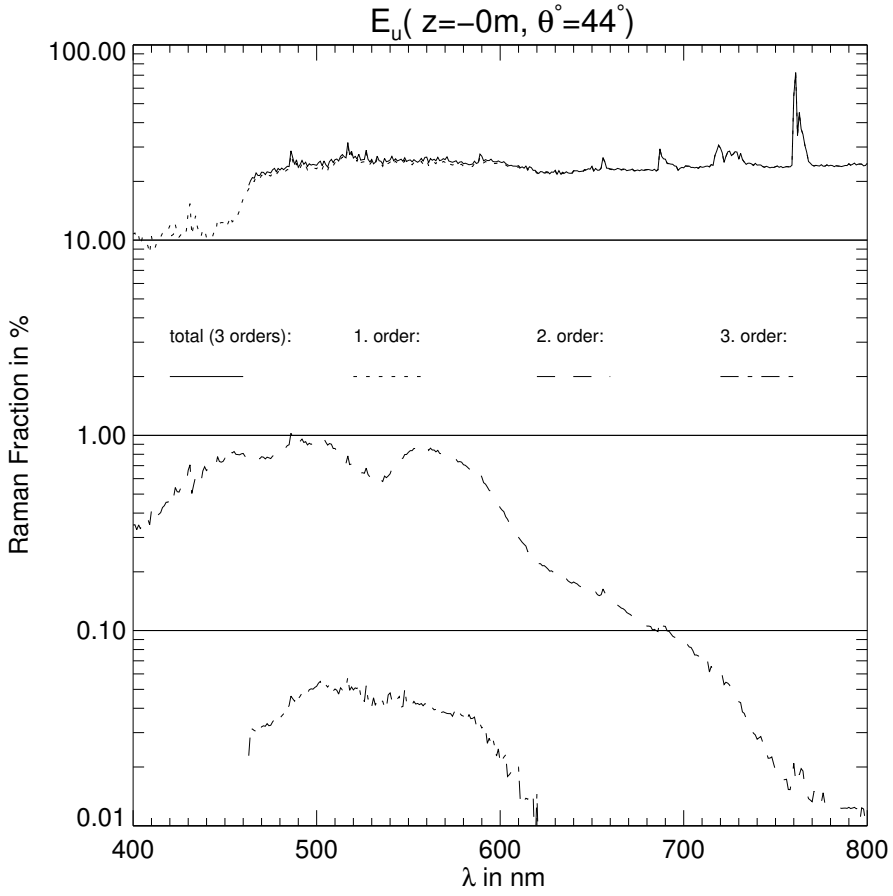

Figure 6.7: Water Raman fractions of $E_u(+0m)$ of first order, second order, third order and the total of the all three, following the definitions in section 2.7, for a solar zenith angle of 44.21°.

Here we want to justify why we have accounted only for the first order of Raman

scattering, following the definition in section 2.7, in most of the computations of this study. A visualization of the involved spectral shifts for higher scattering orders can be found in figure 2.3.

Due to the impact of every additional order on the computation time, a close look on the required accuracy should always be done before e.g. a lookup table generation with multiple variables, which can quickly include hundreds of thousands of cases, is started with the RT model. Furthermore every additional trans-spectral shift significantly adds to the spectral range of the IOPs needed as input. The good news is, that the additional contribution of second and third order Raman scattering effects to the total Raman fraction is very small.

Because the probability of additional Raman scattering events depends on the path length of the photons before being absorbed or leaving the ocean, it can be assumed that clear sea water simulations should be a good basis for the maximum error estimation of higher order contributions. Figure 6.7 shows the Raman fractions of $E_u(+0m)$ of first order, second order, third order and the total of the three. Due to the lack of availability of water IOPs in the lower UV region, the third order fraction is only shown for wavelengths greater than about $460nm$. The absolute contribution of the second order to the Raman fraction of E_u is less than a percent in the visible spectral range and less than 0.1% in the NIR, while the third order contribution generally stay below $\sim 0.05\%$ the green spectral region and slips beneath 0.01% in the red. The minimum order of magnitude between the contributions of the first and the second order is 1.5, while the third order ranges around and below three orders of magnitude under the first order contribution even in pure sea water. This means that errors introduced by not accounting for higher order Raman effects are far below those due to the uncertainty of the Raman IOPs shown in figure 6.3(a). While fore some applications in extremely clear waters the inclusion of the second order effect may be of interest, this will rather not be the case for the turbidities found in average Case 1 and Case 2 waters. These quantitative and spectrally resolved results generally support the earlier finding of Sathyendranath and Platt [104] of second and third order Raman scattering contributing qualitatively two orders of magnitude less than the first order at $520n$m.

6.2.5 Depth Dependence

While Raman scattering in the water body contributes significantly to the upwelling radiation at the sea surface, the fraction of elastically scattered radiation still dominates, except within some atmospheric absorption bands. In water depths of clear water of a few meter in the NIR, a few ten meter in the red and a few hundred meter in the green and blue spectral region, however, Raman scattering becomes the main source of radiation. This is shown for wavelengths of $500nm$ and $700nm$ exemplarily in the figures 6.9 (a) and (b). Wile the downwelling and upwelling irradiances due to elastic scattering and absorption follow an exponential decrease with depth, the irradiances that additionally include the Raman scattered fraction, leave this exponential decrease at a wavelength dependent depth and reach a exponential depth decrease with a steeper gradient after a transition depth range.

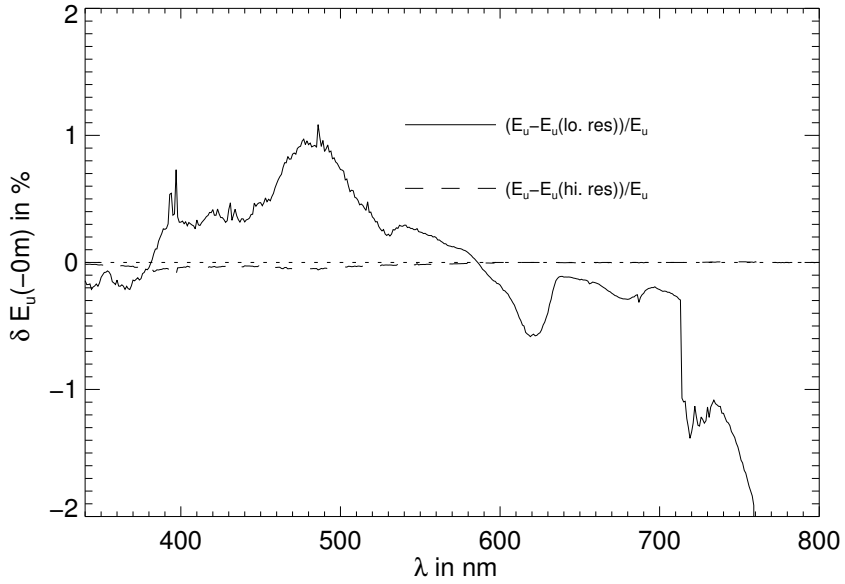

Figure 6.8: Difference in the upwelling irradiance E_u between the default number of layers (see section 6.2.2) and a $999m$ ocean simulated with a single homogeneous layer (solid line). The dashed line shows the latter differences to a model run with a significantly higher vertical resolution whose steps can be seen in the figures 6.9 (a) and (b).

This sort of depth dependence is known to be supported by depth dependent radiation measurements in open waters, if the IOPs don't exhibit a strong depth dependence (see e.g. Fig. 11 in [105]). With growing wavelength, the values of E_d and E_u are increasingly similar in greater depths, when Raman scattering is included, due to the symmetry of the Raman scattering phase function. This is not the case for the elastic fraction of E_d and E_u, where E_d dominates due to the strong component of direct sunlight reaching the water body.

In addition to the default computations with only a few depth steps, the simulations were repeated with a higher number of ocean layers, to also generate the irradiances at these intermediate steps. The negligible differences between the values at depths were both models have a layer boundary, show how well our adapted doubling algorithm for Raman sources (section 2.11) resembles the source operator depth dependence within the model layers. The negligible differences in terms of $E_d(-0m)$ between the two model runs can be seen in figure 6.8 (dashed line). This figure furthermore shows the differences in terms of $E_d(-0m)$ if the ocean is simulated with only one single layer (solid line). Even in this very time efficient computation mode, the reduction of accuracy accounts for a maximum of only approximately 1% error of $E_d(-0m)$ in the visible spectral range. It shall be pointed out that the minor differences remaining between the simulations with different amounts of layers arise purely from the assumptions that the Raman source doubling discussed in section 2.11 is based on. Earlier code versions (e.g. version 1.0 discussed in section 4.2)

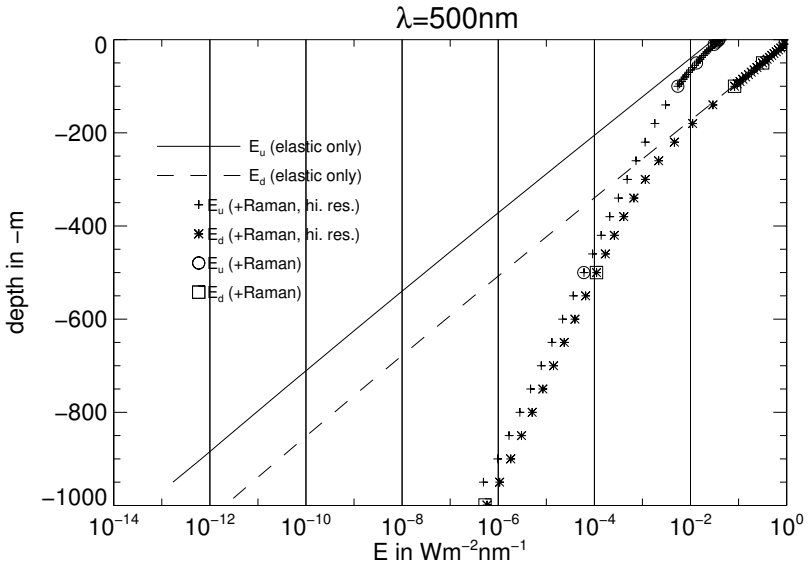

(a)

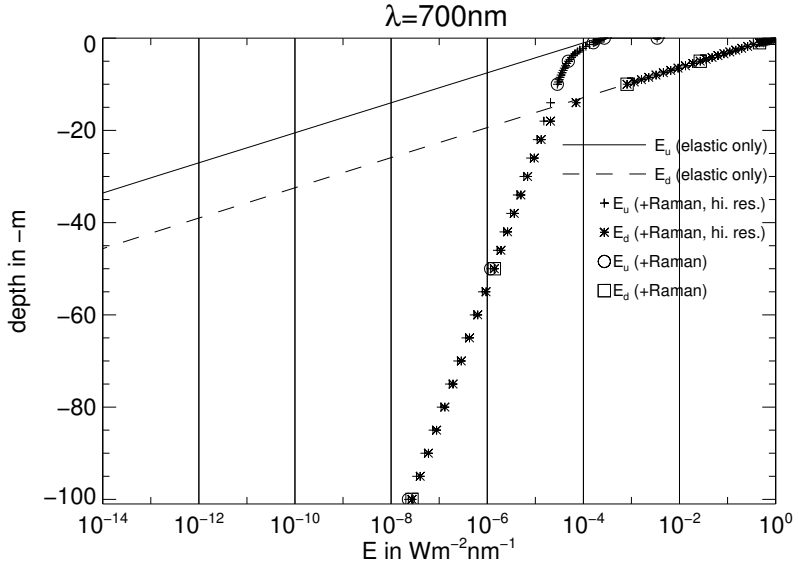

(b)

Figure 6.9: Upwelling and downwelling irradiances in pure sea water as a function of depth. The lines stand for the results when only elastic scattering is included. The boxes and circles are the results including Raman scattering for the depth steps of the default model used in this study. The pluses and stars are the results for a model run with a higher vertical resolution.

had a stronger dependence on the layer number, due to a simpler treatment of the Raman source depth dependence ,and therefore required a higher number of layers near the surface for accurate results in terms of E_u and L_u. Computations for a purely elastic scattering homogeneous medium show no dependence on the layer amount at all, since the doubling of reflection and transmission operators does not require the approximation of a depth gradient and the depth dependency of the source operator for elastically scattered direct solar radiation can be derived from the Lambert-Beer law.

6.2.6 Angular Dependence of the Raman Scattered Radiation Fraction

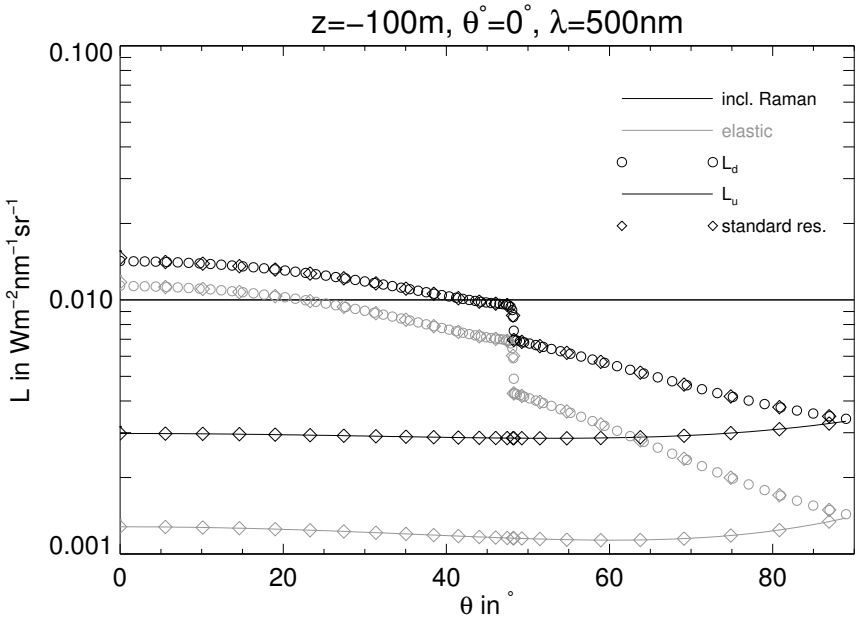

Figure 6.10: The zenith dependence of the radiances at a water depth of $100m$, when the sun is in the zenith. Black stands for computations including Raman scattering and grey without. The solid lines represent the downwelling radiances and the circles the upwelling radiances. The diamonds depict results for upwelling and downwelling radiances from a model run with a lower zenith resolution.

After having focused on irradiances and nadir radiances in the past sections, a closer look at the angular dependence of the radiation field and its Raman fraction shall be taken.

In pure water, radiation can either be absorbed or Rayleigh and/or Raman scattered. The dominant fraction of direct solar radiation and the fact that the forward/backward peak of the Rayleigh scattering function is more pronounced than that of Raman scattering (see figure 1.1), lead to the expectation that Raman scattering should qualitatively distribute radiation orthogonally away from the direction of the direct solar beam. This trend can be seen in figure 6.11, where the angular distribution of the Raman fractions

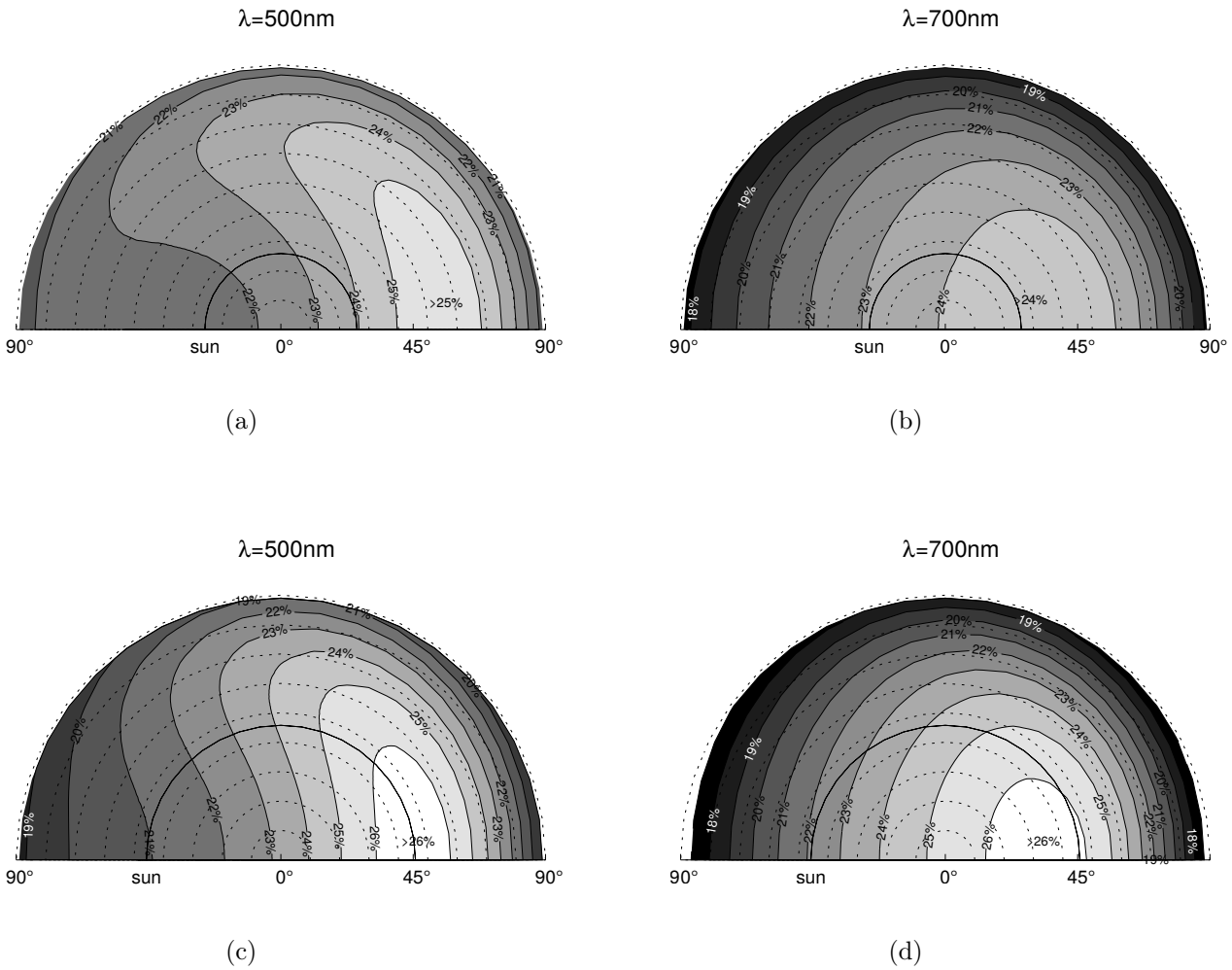

Figure 6.11: Raman fractions of $L_u(-0m)$ in pure sea water for (a): $\lambda = 500nm$ and $\theta° = 25°$, (b): $\lambda = 700nm$ and $\theta° = 25°$, (c): $\lambda = 500nm$ and $\theta° = 45°$, (d): $\lambda = 700nm$ and $\theta° = 45°$. The dotted concentrical circles have constant zenith angles and the solid half circle line is the almucantar. Thought lines of constant azimuth angle are those orthogonal to the concentrical dotted lines and all meet at $\theta = 0°$. The tick position of the sun in zenith and azimuth coordinates is labeled with the word 'sun'. The range margins of the color scale shades are marked with solid contour lines and are labeled with the respective margin values of the Raman fraction in %.

of the radiances $L_u(-0m)$ for the complete upwelling hemisphere is displayed, for two different wavelengths (500 and $700nm$) and two different solar zenith angles (25° and 45°). Clearly, the Raman fractions are greatest at an azimuth position near the opposite sun position. The variation range of Raman fractions depends both on wavelength and solar zenith angle. For the Raman fractions of the radiances at the two shown wavelengths,

which are both in the plateau region where Raman fractions of the upwelling irradiances are fluctuating around roughly 25% (see figure 6.3(a)), values vary between about 18% and 27%. The values below $19 - 20\%$ apply only to very large zenith angles were the featured matrix operator RT Model, with a stratified atmosphere and ocean system without curvature, may not accurately reflect real world cases.

Figure 6.10 shows the angular dependence of the up- and downwelling radiances for $500nm$ at a water depth of $100m$, with and without Raman scattering included. There is no azimuthal dependence because the sun is in the zenith. The angular features of Raman scattering are subtle in comparison to the general angular features of the downwelling light field. The step of increasing brightness for zenith angles $<\sim 49°$ mark the edge of the Fresnel cone. Radiation coming from angles $>\sim 49°$ can't have entered the water body directly from the atmosphere and therefore has been scattered at least once within the water. The upwelling radiation has a less pronounced and rather smooth angular dependence, i.a. due to the symmetric behavior of clear water elastic scattering and Raman scattering. The offset between the radiation including and excluding Raman scattered radiation is greater in the upwelling direction. The diamonds show results for a model run with the default zenith resolution, other symbols and lines stand for results from a higher resolved model run. As expected, no significant differences can be observed. The comparison of outputs for different angular resolutions is often performed as a sanity check of results of new RT models, in the early stages of validation. Obviously, this test was passed by the MOMO Raman model.

6.2.7 Consequences of the Assumption of Isotropic Raman Scattering

It may seem tempting to assume Raman scattering to be isotropic, owing to the less pronounced angular dependence in comparison to clear water elastic scattering (see figure 1.1). This would enable a simpler implementation in an RT model, comparable to the approaches for the inclusion of chlorophyll fluorescence, due to the azimuthal independence, and save computation time. While this may be justifiable for some applications, we give an overview of the quantitative differences in the resulting radiation fields in this section.

Figure 6.12 shows the differences in terms of Raman fractions of $L_u(-0m)$ of the standard case ,shown in figures 6.11 (a) and (b), to a case with isotropic Raman scattering. Note that the output is approximately the same as the respective relative differences in $L_u(-0m)$ between both cases. As can be expected, isotropic Raman scattering overestimates Raman fractions roughly opposite of the solar azimuth position by a few percent (absolute) and vice versa in clear water, due to the fact that isotropic scattering distributes more of the incident direct solar radiation sideways from the beam direction than actual Raman scattering. The same fact also leads to an underestimation of upwelling irradiances up to over a percent for small solar zenith angles (figure 6.13 (a)). The error introduced to the upwelling radiances $L_u(-0m)$ by the isotropic Raman scattering assumption even reaches values of over $5 - 10\%$, for angle regions that are of interest for satellite based

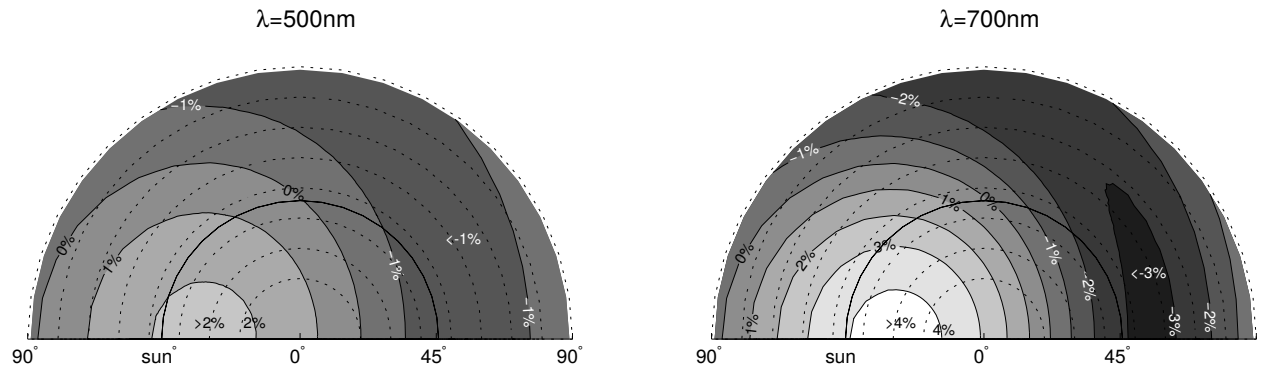

(a) (b)

Figure 6.12: Contour plot of the absolute differences in the Raman fractions of $L_u(-0m)$ for a solar zenith angle of 25°, for the normal angular resolved Raman case minus a case were Raman scattering is assumed to be isotropic. Positive values represent a greater Raman fraction than for the isotropic case and vice versa. The dotted concentrical circles have constant zenith angles and the solid half circle line is the almucantar. Thought lines of constant azimuth angle are those orthogonal to the concentrical dotted lines and all meet at $\theta = 0°$. The tick position of the sun in zenith and azimuth coordinates is labeled with the word 'sun'. The range margins of the color scale shades are marked with solid contour lines and are labeled with the respective margin values of the absolute fraction differences in %.

ocean color and atmosphere remote sensing (figure 6.13 (b)).

Figure 6.14 shows the solar zenith dependence of the effect of neglecting the angular dependence of Raman scattering on the nadir radiances just below the surface. Values of 4 to over 5% are reached only for small solar zenith angles in the red and near infrared spectral range.

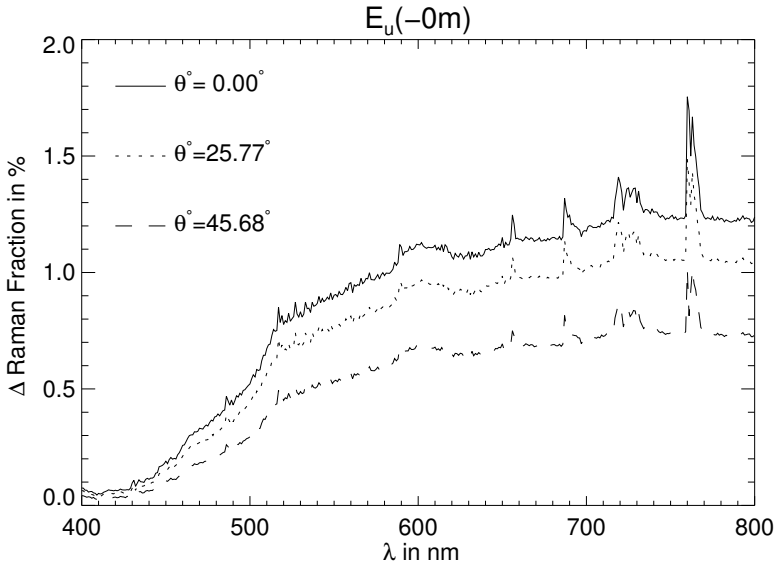

(a)

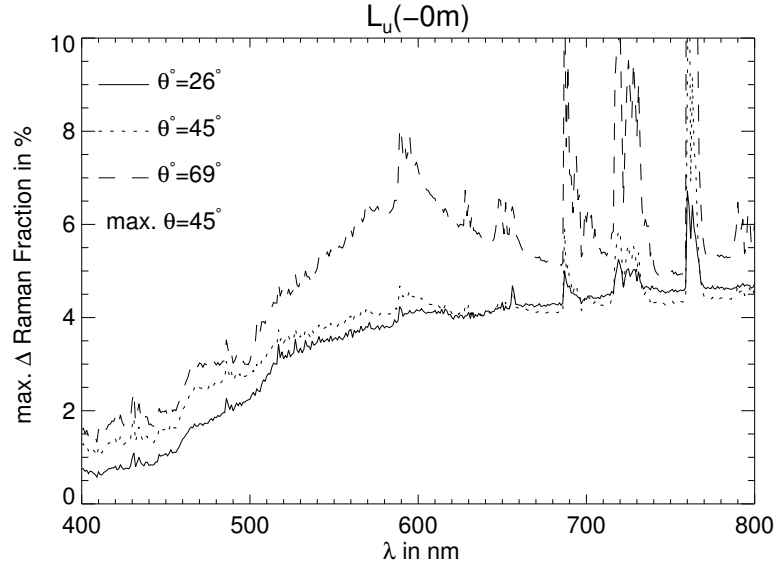

(b)

Figure 6.13: (a): Raman fraction of upwelling vector irradiances $E_u(-0m)$, for standard Raman scattering minus the values for a case where isotropic Raman scattering is assumed, for three different solar zenith angles. (b): Absolute value of the Maximum Raman fraction differences between the standard case and the case with isotropic Raman scattering of upwelling radiances $L_u(-0m)$ for the zenith angle range $0°\theta < 45°$ (but the full azimuth angle range).

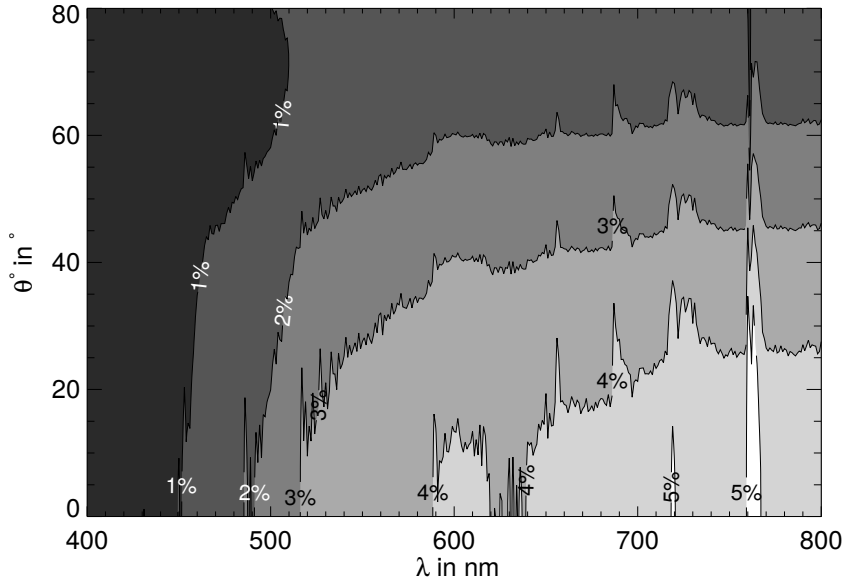

Figure 6.14: Spectral and solar zenith dependence of the Raman fractions differences of the upwelling nadir radiances $L_u(\theta = 0°, -0m)$ between actual and isotropic Raman scattering. The field values at the iso-lines are printed on the lines.

6.2.8 Influence of the Clear Water Absorption Coefficients

In section 1.3.8 the issues with some data sets for clear sea water absorption coefficients, regarding the knowledge of the degree to which they already contain absorption due to inelastic scattering processes, was discussed. Apart from the general measurement problem of maintaining clear sea water samples that have no contamination that influences the optical properties, especially in the UV, the mentioned issue adds a further uncertainty to the simulations. For this study the merged absorption spectra discussed in section 3.2.1 were used with the default assumption of included absorption due to Raman scattering ($\gamma = 1$ in relation 1.14). As can be seen in figure 6.15, the Raman fraction of $E_u(-0m)$ changes only slightly when setting $\gamma = 0$ (meaning that Raman scattering is assumed not to be included in the provided absorption coefficients). The relative decrease of $E_u(-0m)$ between the runs with $\gamma = 1$ and $\gamma = 0$ (but Raman scattering turned on in both) is up to almost 10%, due to a stronger absorbing ocean in the second case. When the formula 6.1 is used to compute the relative difference between a case including Raman scattering and absorption due to Raman scattering and a case, where only elastic scattering takes place and the absorption coefficient is therefore reduced by b^R, to reflect a situation with no optical influence by Raman scattering at all, the results can in principle get negative due to the stronger absorption in the Raman case. This result is shown in 6.15 with the dotted line. These relative differences of $E_u(+0m)$ with Raman compared to the pure elastic case are up to -15% at the spectral minimum of clear water absorption around $410nm$. Finally, it shall be repeated that phenomenological bio-optical models, due to the methods of their

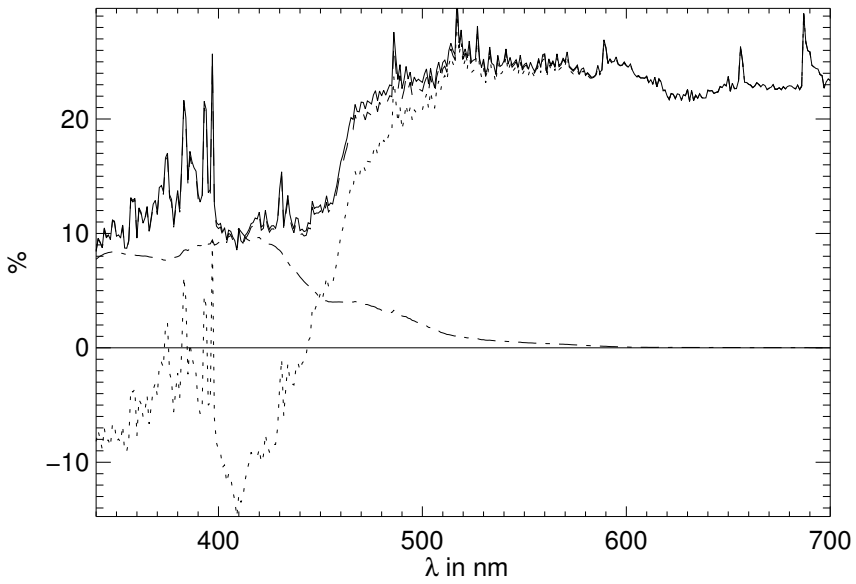

Figure 6.15: Solid line: Raman fraction of $E_u(-0m)$ for default absorption model with the assumption that absorption due to Raman scattering is already included in the tabled absorption coefficients ($\gamma = 1$ in relation 1.14). Dashed line (extinguishable from solid line only between about 450 and $520nm$): Raman fraction of $E_u(-0m)$ for the assumption that Raman scattering is not included in the tabled absorption coefficients ($\gamma = 0$ in relation 1.14). Dashed-dotted line: Relative differences between $E_u(-0m)$ for the latter two cases. Dotted line: Relative difference between $E_u(-0m)$ when Raman scattering is included with $\gamma = 1$ and results for an elastic run were b^R is subtracted from the total absorption coefficient to reflect a hypothetical case, where Raman scattering doesn't exist and therefore has no influence on the absorption at the observation wavelength λ.

retrieval, may also include fractions of Raman scattering as a "pseudo" absorber.

6.2.9 Case 1 Waters

This section features the the Raman contribution for Case 1 waters with a not negligible turbidity. Due to the demonstrative character of this study we have used the simple single parameter bio-optical model 1 introduced in section 3.2.4 to determine the radiation fields and the Raman contribution, for a range of water types associated to pigment concentrations of $0.01, 0.1, 1$ and $10 mg/m^3$. The results for $0.01 mg/m^3$ shall represent conditions found in the clearest ocean waters, $0.1 mg/m^3$ stands for a average value for uncontaminated open oceans in the tropics and sub tropics, while $1 mg/m^3$ already reflects cases found closer to landmasses and $10 mg/m^3$ represents a turbid case with a considerable amount of phytoplankton found in coastal zones and inland waters (see figure 3.4 for a global climatology of measured retrieved chlorophyll concentrations). Furthermore, a fresh water and a sea water case with no chlorophyll was considered as a basis for comparisons. The Raman fraction of the fresh water is significantly enhanced (by several %) in comparison to clear haline water, due to the decreased absolute contribution of elastic scattering as a result of the decreased scattering coefficient in fresh water (also see figure 3.2 with the salinity dependence of elastic scattering). It must be repeated here, that the trade-off of the simple, but widely used, single parameter bio-optical model with a fixed scattering phase function is a decreasing accuracy with increasing chlorophyll concentrations. Also, the accurate simulation of e.g. complex Case 2 waters generally requires more than one input parameter. A discussion addressing the issues can be found in section 3.2.4. In terms of Raman scattering this may lead to an underestimation which increases with growing chlorophyll concentrations, as stated by Gordon [35]. The latter source also suggests that the measured or extrapolated absorption coefficients in the UV are rather unreliable and therefore Raman output below approximately $450 nm$ should be taken with a grain of salt. On the other hand measurements in very clear oceanic regions have in some cases produced UV absorption coefficients that were below those derived for totally clear water under laboratory conditions, thus questioning the accuracy of the clear water coefficients in this spectral region[78].

Figure 6.16(a) shows the Raman fraction of $E_u(-0m)$ for fresh water, clear sea water and sea water with the mentioned pigment concentrations. The fresh water Raman fractions are significantly higher than those of salt water mainly due to the different refractive index resulting in a reduced elastic scattering coefficient in fresh water. while Raman fraction for a pigment concentration of $0.01 mg/m^3$ are only a few percent below those of clear sea water, those for $0.1 mg/m^3$ are approx. 10% in the green and red spectral region, those for $1 mg/m^3$ around 3% and those for $10 mg/m^3$ around $0.6 - 1\%$. This is in qualitative agreement to the values of Waters [129] computed with a similar bio-optical model and also to the values of Schroeder et al. [105], although the latter used separate concentration parameters for chlorophyll and yellow substance and included fluorescence effects and a slightly different bio-optical model. The results of Gordon [35] are higher than ours and those of the other mentioned publications. This can be attributed to the fact that he used the bio-optical model 1 only for the computation of the Raman offset, and a different semi-empirical model for water-leaving radiances that was based on actual radiation

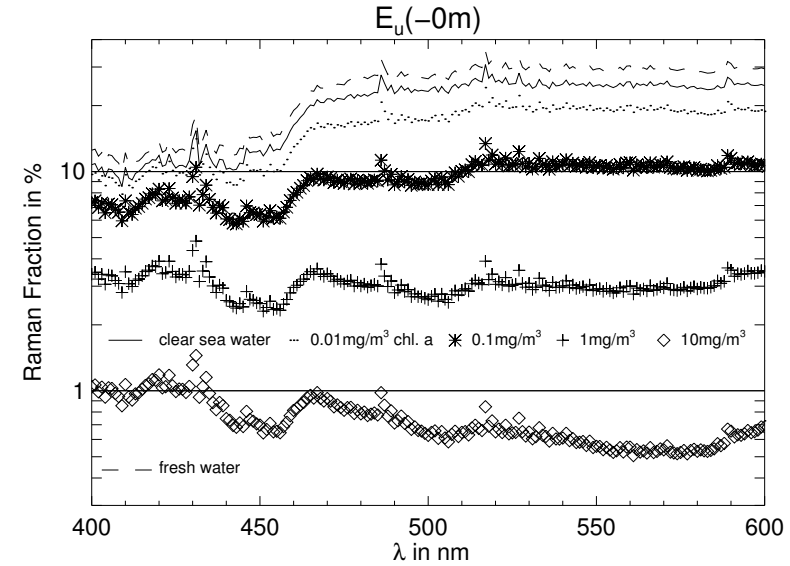

(a)

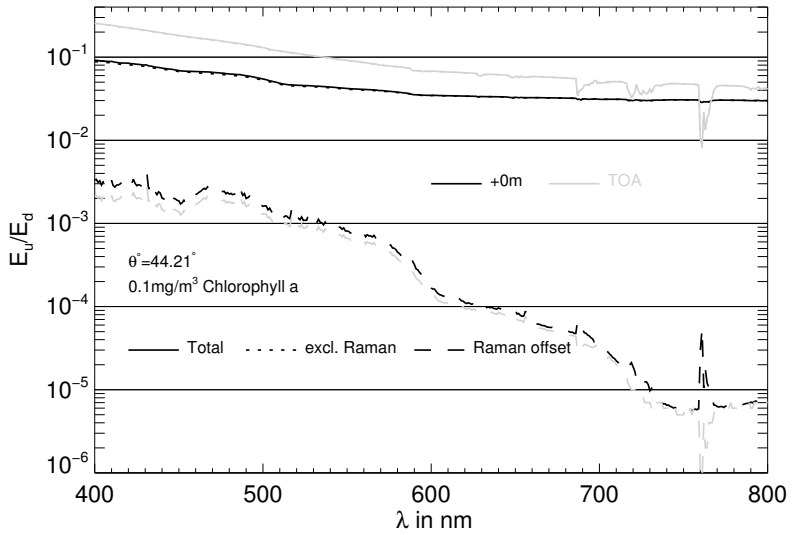

(b)

Figure 6.16: (a) Raman fraction of $E_u(-0m)$ for fresh water ($0PSU$), clear haline sea water ($35PSU$) and haline sea waters with 4 different chlorophyll (pigment) concentrations for bio-optical model 1 (see section 3.2.4). (b): The irradiance reflectance and irradiance reflectance Raman offset of bio-optical model 1 for Case 1 sea water with a chlorophyll concentration of $0.1mg/m^3$, just above the sea surface and at the top of the atmosphere.

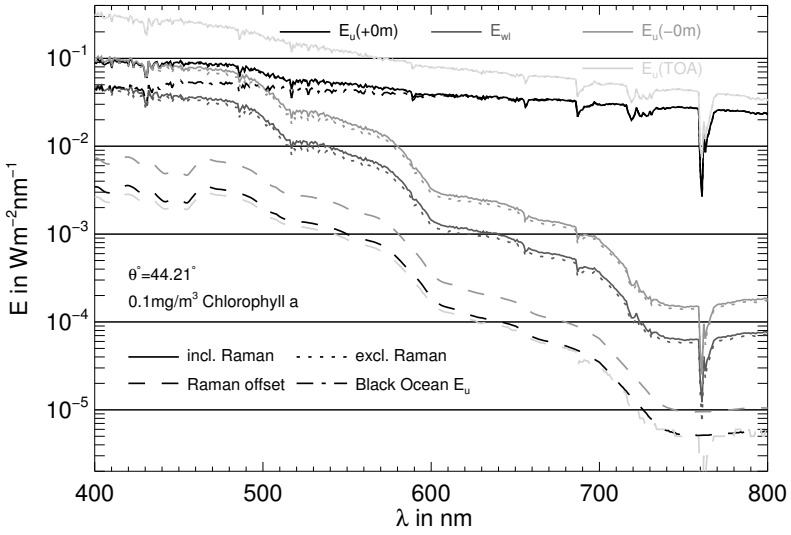

(a)

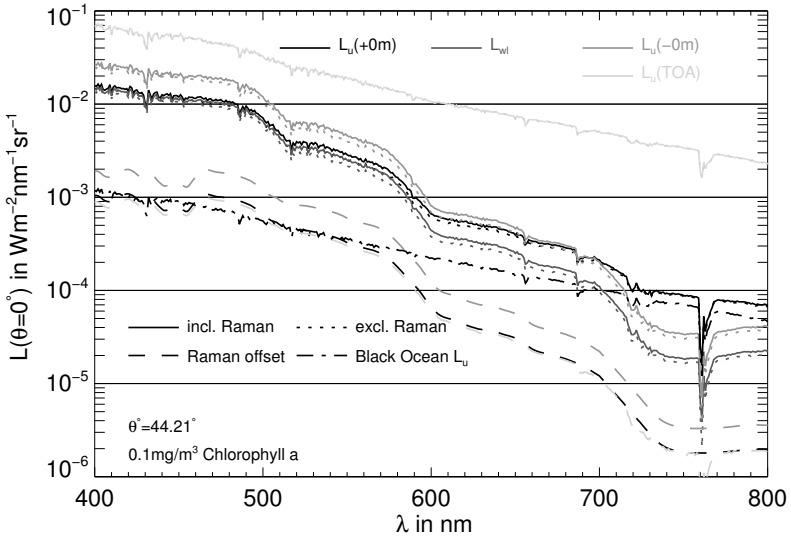

(b)

Figure 6.17: Upwelling irradiance (a) and nadir radiance (b) at the top of the atmosphere and just below the sea surface as well as the water leaving irradiance and radiance for a solar zenith angle of 44.21° for a Case 1 sea water with chlorophyll concentration of $0.1 mg/m^3$ (bio-optical model 1). The quantities are shown including Raman scattering effects and excluding the effect. Furthermore, the difference between the latter two values is shown (Raman offset). The results for a black ocean are shown to illustrate the amount of radiation that has not interacted with the water body, excluding the reflection at its surface.

measurements for the determination of the total radiation. He chose the latter approach to overcome the issues with the simple bio-optical model regarding the overestimation of scattering in turbid waters (see discussion in section 3.2.4).

Figures 6.16(b) and 6.17 show the same quantities discussed in section 6.2.3, but for a chlorophyll concentration of $0.1mg/m^3$, which represent typical Case 1 water conditions, rather than for clear sea water. It shall be pointed out that for quantitative computations of realistic Case 1 and Case 2 waters we use the bio-optical model 2, as e.g. in the SIOCS project introduced in section 6.4 as a basis for ocean color remote sensing algorithms.

6.2.10 A Case With Wind

Due to the influence of the sea surface roughness on Raman and elastically scattered radiation alike, a detailed investigation of the effects of wind speed shall not be included at this place. The effect of wind speed is i.a. included in the look up table generated for the SIOCS project, that is introduced in section 6.4. Nevertheless, we want to show results for a case with a rough surface for an average Case 1 water body here to show the contribution range of Raman scattering in the sun glint area and in the off-glint areas. The wind speed was set to resemble a fresh breeze of $10m/s$ (5 Beaufort). White caps were not simulated. The concentration of chlorophyll was assumed to be $0.1mg/m^3$ and bio-optical model 1 was used and the observation wavelength set to $\lambda = 500nm$.

Figures 6.18 show the upwelling radiances above the ocean and at the top of the atmosphere (a), and the according Raman fractions (b), for the case mentioned above. The position of the solar glint for the 3 different solar angles can be seen in the upper figure. As expected, the Raman fractions in the glint contaminated angle regions are decreased. However, for the two smaller solar zenith angles (0° and 28°), the Raman Fraction still reaches values of $1 - 1.5\%$ in the sun glint above the ocean and about 1% at the top of the atmosphere. Values in the off-glint area go up to 9% just above the ocean and up to about 2% at the top of the atmosphere. This implies that for satellite remote sensing applications that require an accuracy in terms of simulated signal strength of better than 1%, one may have to account for Raman scattering effects even in the sun glint area, if the latter is used for a retrieval in this spectral region (i.a. of atmospheric properties as aerosol optical depth etc.).

6.2.11 Conclusions

While studies of the effect of Raman scattering on the water-leaving radiation with a more qualitative character have been performed before in the past decades by other groups, the advantage of the capabilities of the new MOMO Raman model of accurately simulating the Raman effect spectrally and angularly resolved, in the coupled atmosphere-ocean system, enabled a more detailed look at the influence of Raman scattering. While supporting previous results (e.g. of Gordon [35]) of the generally strong Raman fraction in the upwelling irradiance above the ocean for clear and modestly turbid waters (10 to over 30%), atmospheric effects and spectral structures which were not accounted for in detail by the

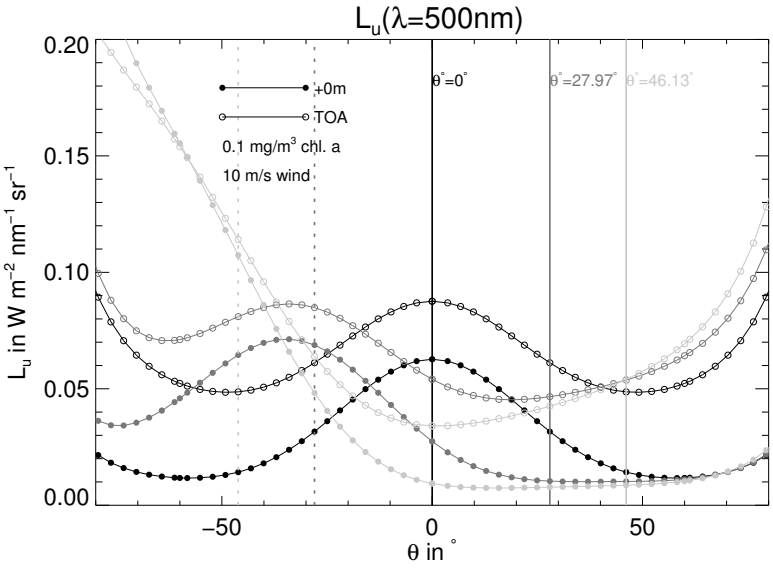

(a)

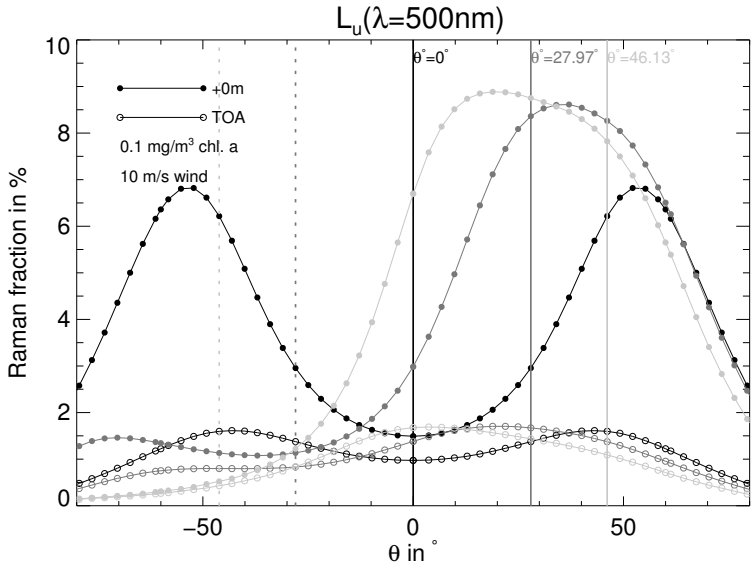

(b)

Figure 6.18: Upwelling radiation L_u and its Raman fraction just above the sea surface, and at the top of the atmosphere in the principal plane. Zenith angles referring to the azimuth angle opposite of the solar position have negative values and those on the solar side positive value. The values are given for three different solar zenith angles. The wind speed set to $10m/s$ and the according rough sea surface properties were computed with the model introduced in section 3.2.6. The chlorophyll concentration is assumed to be $0.1mg/m^3$. The position of the sun is marked by a vertical line in the grey shade of the corresponding results.

predecessors could be resolved. Furthermore, the importance of more precise Raman IOPs was quantified by computing the maximum error of several percent in terms of Raman fraction induced by the use of common input values, due to their uncertainty. It was shown that the accounting for multiple successive Raman scattering events brings only little accuracy gain (less than 1% in terms of Raman fraction of E_u in comparison to a faster first order Raman approximation. It was also demonstrated that our modified *doubling* technique for Raman sources in the RT model allows for fast and accurate results even when sampling the ocean with only a single layer. Also, the immense fraction of Raman scattered radiation in greater water depths was quantified. In addition to the results of previous publications about Raman contributions, we also performed a detailed study of the zenith and azimuth dependency of the Raman fraction and revealed, that errors of several percent in terms of water-leaving radiances would have to be accepted, if Raman scattering were assumed to be isotropic. The latter simplification also induced a significant error of up to over a percent to the upwelling irradiances. The somewhat unsatisfactory general impact of uncertainties of available clear water absorption coefficients in the UV and blue spectral region was shown to be of rather minor significance for the relative Raman fraction, but nevertheless has a significant impact of several percent on the total upwelling radiation in this spectral region. Finally, a study of a case with modestly turbid water and a wind roughened sea surface demonstrated the necessity to account for Raman scattering even in sun glint contaminated scenes, if accuracies of better than one percent of the simulated radiation reaching a satellite sensor are to be achieved (at $500nm$).

6.3 Raman Scattering Effect in the MERIS/OLCI Bands

MERIS (MEdium Resolution Imaging Spectrometer) was an imaging spectrometer aboard ESA's ENVISAT (ENVIronmental SATellite) with 15 spectral channels in the visible and near infrared, whose 8 channels in the visible (displayed in figure 6.19) were designed specifically for the needs of the ocean remote sensing community, but nevertheless used for many other remote sensing applications, including cloud and aerosol property retrievals. MERIS features 5 identical spectrometers arranged in fan shape with a total swath width of $1150km$ (68.5° field of view) and a maximum spatial resolution of $250x300m$ pointing from an $800km$ high sun synchronous orbit that enables global coverage every three days[95]. While MERIS' service lasted from 2002-2012, its successor, the OLCI (Ocean and Land Colour Instrument), an improved instrument version based on the MERIS concept but with additional spectral channels and radiometric accuracy, is awaiting launch aboard the ESA satellite Sentinel-3. The additional channels in the visible spectral range are aimed at improved water constituent retrievals (channel at $400nm$ with $15nm$ width) and a better sampling of the chlorophyll fluorescence ($673.75nm$ channel with $7.5nm$ width in addition to the $681.25nm$ heritage channel)[116]. A slight off-nadir tilt of the observation angle will also allow for a higher fraction of observations without sun glint contamination.

Figure 6.19 shows the Raman fraction of the nadir radiance for pure sea water at the sensor, for the actual spectral bands on MERIS and OLCI. The range of values between

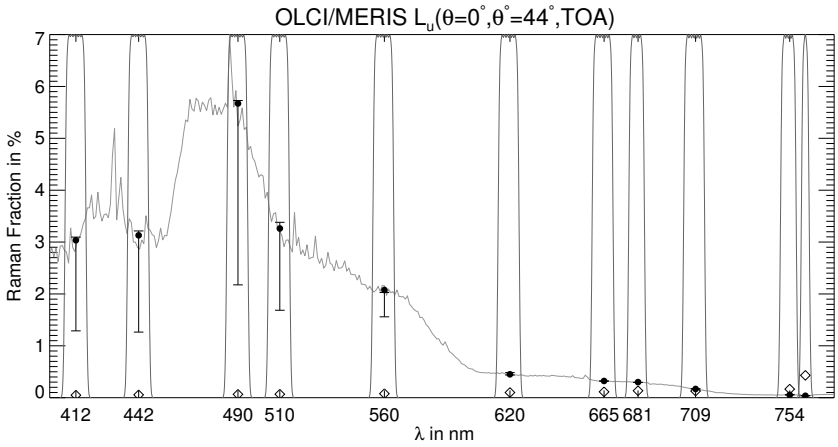

Figure 6.19: Raman fraction of the upwelling nadir radiance at the top of the atmosphere for a solar zenith angle of 44.21°, integrated to resemble the spectral bands of the MERIS (and OLCI) instrument. The MERIS channel filter functions are shown in grey. Additional OLCI channels are not shown. The solid line in the background stands for the Raman fraction of pure haline water ($35PSU$). The solid dots stand for the Raman fraction of pure haline water ($35PSU$) in the instrument channels. The upper end of the error bars marks values for pure fresh water and the lower end Raman fractions for a chlorophyll concentration of $0.1mg/m^3$ (bio-optical model 1) and $35PSU$. The diamonds mark the threshold of detectability determined from the anticipated OLCI signal-to-noise ratio (SNR from [116]) at a reference signal strength. Thus the Raman signal can only be detected in the channels of the visible spectral range and is below the instrument noise level in the shown NIR channels. All results were computed with MOMO Raman 2.1. and the atmosphere was considered to be aerosol free. The default settings from section 6.2.2 were used for the definition of the ocean and atmosphere state.

a Case 1 water with $0.1mg/m^3$ pigment (bio-optical model 1) and $35PSUI$ salinity and fresh water with $0PSU$ is shown in form of error bars. While values for clear water reach nearly 6% in the $560nm$ channel, those for the turbid case stay below 2%. In the red and near infrared, values are below 1% in general. The diamonds depict the technical detection threshold, approximated from the reciprocal signal-to-noise ratio from the OLCI technical specifications [116]. Accordingly, the Raman signal is stronger than the instrument noise throughout the visible spectral range, but falls below the detection threshold for the shown channels the near infrared, were the overall signal fraction coming from the ocean gets very weak. Due to the use of the near infrared channels mainly for atmospheric correction purposes in the field of ocean remote sensing, the latter is no surprise.

A very detailed sensitivity study of the effect of Raman scattering in Case 1 waters on radiances in the MERIS/OLCI bands has been prepared within the ESA support to science project WaterRadiance (von Bismarck and Fischer [122]). It discusses the dependence of the effect on salinity and temperature as well as the angular dependence and is based on the initial MOMO Raman version 1.0. Due to its extent and a partial overlap with the

results discussed in section 6.2, it shall solely be referred to the latter report for more details at this place.

6.4 Sensor Independent Ocean Colour Service

The remote sensing of the ocean from satellites is an increasingly popular field, as the instrument technology advances and the importance of the knowledge of the ocean state and pollution for the understanding of the global climate, ecology and the oceans role in the carbon cycle has been identified. Satellites are the only technological way to achieve temporal and global coverage of the retrieved states with a single instrument.

The general idea of ocean remote sensing is the relation of the ocean state, including i.a. the concentration of its constituents and its temperature, to the signals measured by a sensor. Due to the complexity of the earth system in terms of radiometric behavior, it is mostly not possible to find a direct analytical relationship between the measurement and the system state interested in. Therefore, a variety of inversion techniques are featured in ocean remote sensing applications. They generally consist of a forward model component, that generates synthetical measurements to any hypothetical system state, and a minimization component, that retrieves the actual system state by minimizing the residual between forward model output and measurement, under consideration of the model and measurement errors. The latter component often has to deal with ill posed problems, and therefore needs to be provided with additional a priori data to constrain the solution space. The forward models are most often based on the ability of radiative transfer models to simulate radiation quantities, as would be measured by a satellite sensor, when given the state of the earth in terms of inherent optical properties as input.

The Sensor Independent Ocean Colour service (SIOCS) project was the first to feature the new MOMO Raman radiative transfer model for a processor designed for the retrieval of oceanic constituents, due to the significance of Raman scattering for this type of application. SIOCS is a DLR (*German Aerospace Center*) and German BMWi (*Federal Ministry for Economic Affairs and Energy*) funded joint project of the Institute for Space Sciences of the *Free University of Berlin* (contributions by Lena Kritten, Rene Preusker and Jonas v. Bismarck) and *Brockmann Consult* (Daniel Odermatt and Carsten Brockmann). The basis for the forward model is a lookup table of atmosphere corrected water-leaving reflectances generated for the complete spectral region from $390 - 1040nm$ with the option for extension. It is therefore sensor independent and can be adapted to many different instruments, including but not limited to OLCI, SLSTR, MODIS, AVHRR and EnMAP. The dimensions of the lookup table (LUT) were defined by the five optical parameters of the featured bio-optical model 2 described in section 3.2.4. This bio-optical model that is based directly on IOPs related to different oceanic constituents rather than microphysical properties, was chosen due to its flexibility regarding the adaption to regionally varying conditions and its capability of modeling optically complex Case 2 water types. Rather than varying the absorption by CDOM and detritus independent of each other, there relative number ratio was varied. The same was performed for the white and blue scatterers. Owing to the high

number of model runs necessary to produce a table with six dimensions, associated to the 5 species and the water salinity, with a sufficient spacing for smooth interpolation, the MOMO computations were carried out on the computing cluster *CALVALUS* of *Brockmann Consult*. Nevertheless, the computation of the Raman offsets of the water-leaving reflectances with MOMO Raman was performed on a less dense IOP grid with subsequent interpolation to the native grid resolution, owing to the more time consuming Raman computations due to the necessary incorporation of the excitation band computations. A sensitivity study furthermore provided threshold values for the significance of Raman scattering in terms of the bio-optical model parameters. Raman contributions therefore only had to be computed for IOP values above the threshold. However, the development of the much faster MOMO Raman model versions 2.0 and 2.1 was i.a. a consequence of the SIOCS project requirements for high execution speed. Sensor specific adaption of the information is done by a convolution with respect to the actual sensor filter functions. To provide the forward operator with even faster access to the information stored in the lookup table, the latter LUT also may be used to train an artificial neural network (ANN) to provide the approximative relation of a set of all bio-optical model parameters (5 IOPs) to the water-leaving reflectance spectra [81].

The minimization of the cost function, describing the residuals of the forward model output in relation to the retrieved state, is performed by the use of an *optimal estimation* technique which is discussed in detail in Rodgers [97]. The latter method provides an iterative approach for the determination of the optimal system state, given the measurement, the measurement error and model error covariances, and an initial guess of the state. One advantage of the optimal estimation approach is the close integration and traceability of the error propagation and the ability to flexibly constrain the state space by a priori information. To ensure the applicability of the approach, which requires a normal distribution of the retrievable parameters, the MERMAID database [5] of globally distributed marine IOP measurements was used. Owing to the found distributions, the forward operator and inversion were equipped with the capability of retrieving in the logarithmic state space [55]. The latter or similar databases also provide a basis for the initial state guess and its regional and temporal variance.

The first applications for the new retrieval method included scenes detected by the existing data of the MERIS, MODIS and SeaWIFS instruments. For MERIS, e.g. the retrievals for the Yellow Sea, were algae blooms are abundant, showed that the measured reflectance spectra could be reproduced well by the model and that the retrieval of IOPs resulted in realistic values [55]. The processor is available within the BEAM software package [30] and one of its next applications will be the measurements of the OLCI and SLSTR instruments on the upcoming Sentinel-3 ESA satellite. Furthermore, an advanced atmospheric correction scheme for aerosols, developed within our group by Lena Kritten et al. under the name SIACS, promises an additional improvement of the retrieval.

Conclusions and Outlook

Having identified the need for accurate angular and spectral resolved predictions of the contributions of vibrational Raman scattering in the ocean to radiometric quantities of interest for the field of remote sensing, a method for the quantitative incorporation of non-isotropic inelastic scattering effects in matrix-operator numeric radiative transfer models has been developed and applied to the RT model MOMO for the combined atmosphere-ocean system. Although vibrational Raman scattering of liquid water was the primary motivation, the new Model version allows for the inclusion of additional sources of radiation in general, such as rotational Raman scattering in the atmosphere.

Studies of the contribution of Raman scattered radiation to the upwelling radiation at the sea surface and at the top of the atmosphere, with this new model, have qualitatively supported earlier findings about the order of magnitude of the effect and the turbidity dependence, but showed new details of the spectral and angular properties of the effect. Multiple Raman scattering has shown to contribute with less than a percent to the water-leaving radiances, which justifies a first order Raman scattering approximation for most applications. The approximation of isotropic Raman scattering has been found to lead to water-leaving radiance errors of several percent in the visible spectral range for clear water, and can therefore only be recommended were a qualitative treatment of Raman scattering is sufficient or if only interested in irradiances (water-leaving irradiances only show an error of roughly 1% in clear water for the approximation). On the other hand, a treatment of the depth dependency of the excitational energy with a logarithmic interpolation between two model layer positions has proven to be sufficient and computation time saving in the matrix-operator method, even for optically thick layers. At the top of the atmosphere, fractions of Raman scattered radiation are naturally lower than at sea level due to atmospheric scattering. Nevertheless, significant levels of several percent are reached in the the blue and green spectral region, and even in turbid waters at sun glint contaminated geometries, the Raman fraction may exceed one percent. It was also shown that the contribution of Raman scattering can in principal be detected in all channels of the ESA OLCI sensor in the visible, whereas in the near infrared channels the assumed instrument noise level exceeds the Raman signal. While the accuracy of the Raman scattering coefficient measurements have improved in the past decades, and doubtless this development will continue, the values widely used nowadays still have to be considered a non negligible source of error in the predictions of Raman contributions. The same can be said about the measurements of clear water absorption coefficients and their entanglement with the Raman scattering effect.

After having been successfully validated, the RT model MOMO Raman has i.a. demonstrated its capabilities in a new processor for the retrieval of ocean constituents from satellite images. The next related steps in preparation in our research group include the study of the combined effects of Raman scattering and chlorophyll fluorescence and an examination of the polarization of Raman scattered radiation.

Bibliography

[1] Charles Acquista and James L Anderson. A derivation of the radiative transfer equation for partially polarized light from quantum electrodynamics. *Annals of Physics*, 106(2):435–443, 1977.

[2] J. I. Antonov, D. Seidov, T. P. Boyer, R. A. Locarnini, A. V. Mishonov, H. E. Garcia, O. K. Baranova, M. M. Zweng, and D. R. Johnson. *World Ocean Atlas 2009, Volume 2: Salinity*, volume 2. U.S. Government Printing Office, Washington, D.C., 184 pp., noaa atlas nesdis 69 edition, 2010.

[3] US Standard Atmosphere. National oceanic and atmospheric administration. *National Aeronautics and Space Administration, United States Air Force, Washington, DC*, 1976.

[4] Roswell W Austin and George Halikas. The index of refraction of seawater. 1976.

[5] Kathryn Barker, Constant Mazeran, Christophe Lerebourg, Marc Bouvet, David Antoine, Michael Ondrusek, Guiseppe Zibordi, and Samantha Lavender. Mermaid: The meris matchup in-situ database. In *MERIS and (A) ATSR Workshop, Frascati*, 2008.

[6] Jasmine S. Bartlett, Kenneth J. Voss, Shubha Sathyendranath, and Anthony Vodacek. Raman scattering by pure water and seawater. *Appl. Opt.*, 37(15):3324–3332, May 1998. doi: 10.1364/AO.37.003324. URL `http://ao.osa.org/abstract.cfm?URI=ao-37-15-3324`.

[7] Ralf Bennartz and Jürgen Fischer. A modified k-distribution approach applied to narrow band water vapour and oxygen absorption estimates in the near infrared. *Journal of Quantitative Spectroscopy and Radiative Transfer*, 66(6):539–553, 2000.

[8] Craig F Bohren and Donald R Huffman. *Absorption and scattering of light by small particles*. John Wiley & Sons, 2008.

[9] Andrew Bray, Robert Chapman, and Taras Plakhotnik. Accurate measurements of the Raman scattering coefficient and the depolarization ratio in liquid water. *Appl. Opt.*, 52(11):2503–2510, Apr 2013. doi: 10.1364/AO.52.002503. URL `http://ao.osa.org/abstract.cfm?URI=ao-52-11-2503`.

[10] Annick Bricaud, Andre Morel, and Louis Prieur. Absorption by dissolved organic matter of the sea (yellow substance) in the UV and visible domains. *Limnology and oceanography*, 26(1):43–53, 1981.

[11] Annick Bricaud, Andre Morel, and Louis Prieur. Optical efficiency factors of some phytoplankters1. *Limnology and Oceanography*, 28(5):816–832, 1983.

[12] Annick Bricaud, Marcel Babin, André Morel, and Hervé Claustre. Variability in the chlorophyll-specific absorption coefficients of natural phytoplankton: Analysis and parameterization. *Journal of Geophysical Research: Oceans (1978–2012)*, 100(C7): 13321–13332, 1995.

[13] Annick Bricaud, André Morel, Marcel Babin, Karima Allali, and Hervé Claustre. Variations of light absorption by suspended particles with chlorophyll a concentration in oceanic (Case 1) waters: Analysis and implications for bio-optical models. *Journal of Geophysical Research: Oceans (1978–2012)*, 103(C13):31033–31044, 1998.

[14] Carsten Brockmann, Roland Doerffer, Shubha Sathyendranath, Kevin Ruddick, Vanda Brotas, Richard Santer, and Simon Pinnock. The coastcolour dataset. In *Geoscience and Remote Sensing Symposium (IGARSS), 2012 IEEE International*, pages 2036–2039. IEEE, 2012.

[15] Kelly V Chance and Robert JD Spurr. Ring effect studies: Rayleigh scattering, including molecular parameters for rotational Raman scattering, and the Fraunhofer spectrum. *Applied Optics*, 36(21):5224–5230, 1997.

[16] Subrahmanyan Chandrasekhar. *Radiative transfer*. Courier Dover Publications, 1950.

[17] Chin H Chang and Lee A Young. Seawater temperature measurement from Raman spectra. Technical report, DTIC Document, 1972.

[18] Paula G Coble. Characterization of marine and terrestrial DOM in seawater using excitation-emission matrix spectroscopy. *Marine chemistry*, 51(4):325–346, 1996.

[19] CHARLES COX and WALTER MUNK. Measurement of the roughness of the sea surface from photographs of the sun's glitter. *J. Opt. Soc. Am.*, 44(11):838–850, Nov 1954. doi: 10.1364/JOSA.44.000838. URL `http://www.opticsinfobase.org/abstract.cfm?URI=josa-44-11-838`.

[20] Russell A Desiderio. Application of the Raman scattering coefficient of water to calculations in marine optics. *Applied optics*, 39(12):1893–1894, 2000.

[21] R Doerffer and J Fischer. Measurement and model simulation of sun stimulated chlorophyll fluorescence within a daily cycle. *Advances in space research*, 7(2):117–120, 1987.

[22] Lionel Doppler, Cintia Carbajal-Henken, Jacques Pelon, François Ravetta, and Jürgen Fischer. Extension of radiative transfer code MOMO, matrix-operator model to the thermal infrared–Clear air validation by comparison to RTTOV and application to CALIPSO-IIR. *Journal of Quantitative Spectroscopy and Radiative Transfer*, 144: 49–67, 2014.

[23] Lionel Doppler, René Preusker, Ralf Bennartz, and Jürgen Fischer. k-bin and k-IR: k-distribution methods without correlation approximation for non-fixed instrument response function and extension to the thermal infrared - Applications to satellite remote sensing. *Journal of Quantitative Spectroscopy and Radiative Transfer*, 133: 382–395, 2014.

[24] Kerstin Ebert. *Exceptional Phytoplankton Bloom Recognition from Visible Spectral Satellite Radiometry Data.* PhD thesis, Freie Universität Berlin, 2009.

[25] Gregory W. Faris and Richard A. Copeland. Wavelength dependence of the Raman cross section for liquid water. *Appl. Opt.*, 36(12):2686–2688, Apr 1997. doi: 10.1364/AO.36.002686. URL `http://ao.osa.org/abstract.cfm?URI=ao-36-12-2686`.

[26] Frank Fell. *Validierung eines Modells zur Simulation des Strahlungstransportes in Atmosphäre und Ozean.* PhD thesis, Freie Universität Berlin, Institut für Weltraumwissenschaften, 1997.

[27] Frank Fell and Rene Preusker. Effects of the wind direction on the light-field reflected from a wind roughened sea surface. In *Ocean Optics XIII*, pages 78–83. International Society for Optics and Photonics, 1997.

[28] Juergen Fischer and Hartmut Grassl. Radiative transfer in an atmosphere-ocean system: an azimuthally dependent matrix-operator approach. *Applied Optics*, 23(7): 1032–1039, 1984.

[29] Juergen Fischer, Roland Doerffer, Hartmut Grassl, et al. Factor analysis of multispectral radiances over coastal and open ocean water based on radiative transfer calculations. *Applied optics*, 25(3):448–456, 1986.

[30] Norman Fomferra and Carsten Brockmann. Beam-the ENVISAT MERIS and AATSR toolbox. In *MERIS (A) ATSR Workshop 2005*, volume 597, page 13, 2005.

[31] Frank Fell and Jürgen Fischer. Numerical simulation of the light field in the atmosphere-ocean system using the matrix-operator method. *Journal of Quantitative Spectroscopy and Radiative Transfer*, 69(3):351 – 388, 2000. ISSN 0022-4073. doi: DOI:10.1016/S0022-4073(00)00089-3. URL `http://www.sciencedirect.com/science/article/B6TVR-42BTJX6-6/2/3a22b6d76579a6d07d279c4ae20ce479`.

[32] RDM Garcia, CE Siewert, and AM Yacout. On the use of Fresnel boundary and interface conditions in radiative-transfer calculations for multilayered media. *Journal of quantitative spectroscopy and radiative transfer*, 109(5):752–769, 2008.

[33] Yuntao Ge, Howard R Gordon, and Kenneth J Voss. Simulation of inelastic-scattering contributions to the irradiance field in the ocean: variation in Fraunhofer line depths. *Applied optics*, 32(21):4028–4036, 1993.

[34] Howard R Gordon. Diffuse reflectance of the ocean: the theory of its augmentation by chlorophyll a fluorescence at 685 nm. *Applied Optics*, 18(8):1161–1166, 1979.

[35] Howard R. Gordon. Contribution of Raman scattering to water-leaving radiance: a reexamination. *Appl. Opt.*, 38(15):3166–3174, May 1999. doi: 10.1364/AO.38.003166. URL `http://ao.osa.org/abstract.cfm?URI=ao-38-15-3166`.

[36] Howard R Gordon, Otis B Brown, and Michael M Jacobs. Computed relationships between the inherent and apparent optical properties of a flat homogeneous ocean. *Applied optics*, 14(2):417–427, 1975.

[37] Howard R Gordon, Otis B Brown, Robert H Evans, James W Brown, Raymond C Smith, Karen S Baker, and Dennis K Clark. A semianalytic radiance model of ocean color. *Journal of Geophysical Research: Atmospheres (1984–2012)*, 93(D9):10909–10924, 1988.

[38] JF Grainger and J Ring. Anomalous Fraunhofer line profiles. *Nature*, 193:762, 1962.

[39] IP Grant and GE Hunt. Discrete space theory of radiative transfer. i. fundamentals. *Proceedings of the Royal Society of London. A. Mathematical and Physical Sciences*, 313(1513):183–197, 1969.

[40] Sarah A Green and Neil V Blough. Optical absorption and fluorescence properties of chromophoric dissolved organic matter in natural waters. *Limnology and Oceanography*, 39(8):1903–1916, 1994.

[41] Luis Guanter, Christian Frankenberg, Anu Dudhia, Philip E Lewis, José Gómez-Dans, Akihiko Kuze, Hiroshi Suto, and Roy G Grainger. Retrieval and global assessment of terrestrial chlorophyll fluorescence from GOSAT space measurements. *Remote Sensing of Environment*, 121:236–251, 2012.

[42] Vladimir I. Haltrin and George W. Kattawar. Self-consistent solutions to the equation of transfer with elastic and inelastic scattering in oceanic optics: I. model. *Appl. Opt.*, 32(27):5356–5367, Sep 1993. doi: 10.1364/AO.32.005356. URL `http://ao.osa.org/abstract.cfm?URI=ao-32-27-5356`.

[43] Steven K Hawes, Kendall L Carder, and George R Harvey. Quantum fluorescence efficiencies of fulvic and humic acids: effects on ocean color and fluorometric detection. In *San Diego'92*, pages 212–223. International Society for Optics and Photonics, 1992.

[44] André Hollstein and Jürgen Fischer. Radiative transfer solutions for coupled atmosphere ocean systems using the matrix operator technique. *Journal of Quantitative Spectroscopy and Radiative Transfer*, 113(7):536–548, 2012.

[45] André Hollstein, Jonas von Bismarck, Jürgen Fischer, and René Preusker. Description of the vector radiative transfer model momo. ESA *support to science* project *waterradiance* document (contract AO 1-5859/08/NL/CT), December 2010.

[46] H.C. Hulst. *A New Look at Multiple Scattering*. NASA Institute for Space Studies, Goddard Space Flight Center, 1963. URL `http://books.google.de/books?id=OFFfHAAACAAJ`.

[47] Joanna Joiner, Pawan K Bhartia, Richard P Cebula, Ernest Hilsenrath, Richard D McPeters, and Hongwoo Park. Rotational Raman scattering (ring effect) in satellite backscatter ultraviolet measurements. *Applied Optics*, 34(21):4513–4525, 1995.

[48] George W Kattawar and Charles N Adams. Errors in radiance calculations induced by using scalar rather than stokes vector theory in a realistic atmosphere-ocean system. *Ocean Optics X*, 1302:2–12, 1990.

[49] George W. Kattawar, Terry J. Humphreys, and Gilbert N. Plass. Radiative transfer in an atmosphere-ocean system: A matrix operator approach. *Proc. SPIE*, 1978.

[50] GW Kattawar, Andrew T Young, and Terry J Humphreys. Inelastic scattering in planetary atmospheres. I-the ring effect, without aerosols. *The Astrophysical Journal*, 243:1049–1057, 1981.

[51] Milton Kerker. Some recent reflections on light scattering. *Journal of Colloid and Interface Science*, 58(1):100–112, 1977.

[52] VI Khalturin. The self-consistent two-stream approximation in radiative transfer theory. *Akademiia Nauk SSSR Fizika Atmosfery i Okeana*, 21:589–597, 1985.

[53] DA Kiefer, WS Chamberlin, and CR Booth. Natural fluorescence of chlorophyll a: Relationship to photosynthesis and chlorophyll concentration in the western south pacific gyre. *Limnology and Oceanography*, 34(5):868–881, 1989.

[54] Dale A Kiefer and Rick A Reynolds. Advances in understanding phytoplankton fluorescence and photosynthesis. In *Primary productivity and biogeochemical cycles in the sea*, pages 155–174. Springer, 1992.

[55] Lena Kritten. Sensorunabhängiges Verfahren zur Bestimmung von Wasserqualitätsparametern aus Daten der Sentinel Satelliten und nationaler Missionen. SIOCS Abschlussbericht, 50 EE 1205, 2014.

[56] R. L. Kurucz. High resolution irradiance spectrum from 300 to 1000 nm, revised 2 jan 2010. Kurucz.harvard.edu/sun/irradiance2005/irradthuwl.dat, 2005, 2010.

[57] Robert L Kurucz, Ingemar Furenlid, James Brault, and Larry Testerman. Solar flux atlas from 296 to 1300 nm. *National Solar Observatory Atlas, Sunspot, New Mexico: National Solar Observatory, 1984*, 1, 1984.

[58] Arve Kylling, Claudie Emde, and Ulrich Hamann. Wp2200: Preliminary algorithm theoretical basis document for libRadtran demonstration version. ESAS-Light, 2008.

[59] Johannes Lampel, Johannes Zielcke, Udo Frieß, Ulrich Platt, and Thomas Wagner. On the impact of vibrational Raman scattering of N_2/O_2 on max-doas measurements of atmospheric trace gases. In *Geophysical Research Abstracts*, volume 17, 2015.

[60] J Landgraf, OP Hasekamp, R Van Deelen, and I Aben. Rotational Raman scattering of polarized light in the earth atmosphere: a vector radiative transfer model using the radiative transfer perturbation theory approach. *Journal of Quantitative Spectroscopy and Radiative Transfer*, 87(3):399–433, 2004.

[61] R. A. Locarnini, A. V. Mishonov, J. I. Antonov, T. P. Boyer, H. E. H. E. Garcia, O. K. Baranova, M. M. Zweng, and D. R. Johnson. *World Ocean Atlas 2009, Volume 1: Temperature.*, volume 1. U.S. Government Printing Office, Washington, D.C., 184 pp., noaa atlas nesdis 68 edition, 2010.

[62] Z. Lu. *Optical absorbtion of pure water in the blue and ultraviolet.* PhD thesis, Texas A&M University, 2006.

[63] Bruce R. Marshall and Raymond C. Smith. Raman scattering and in-water ocean optical properties. *Appl. Opt.*, 29(1):71–84, Jan 1990. doi: 10.1364/AO.29.000071. URL `http://ao.osa.org/abstract.cfm?URI=ao-29-1-71`.

[64] Jean-Joseph Max and Camille Chapados. Isotope effects in liquid water by infrared spectroscopy. III. h_2o and d_2o spectra from 6000 to 0 cm^{-1}. *The Journal of Chemical Physics*, 131(18):184505, 2009. doi: 10.1063/1.3258646. URL `http://link.aip.org/link/?JCP/131/184505/1`.

[65] C. Mobley. *SEQUOIA HYDROLIGHT-ECOLIGHT 5.0.* SEQUOIA.

[66] C Mobley, E Boss, and C Roesler. Ocean optics web book, 2011.

[67] C.D. Mobley. *Light and water: radiative transfer in natural waters.* Academic Press, 1994. ISBN 9780125027502. URL `http://books.google.de/books?id=oS9RAAAAMAAJ`.

[68] Curtis Mobley. personal communication by email, 6 2011.

[69] Curtis Mobley. HydroLight Technical Note 10 - interpretation of Raman scattering interpretations. Technical report, Sequoia, 2012.

[70] Curtis D Mobley. A numerical model for the computation of radiance distributions in natural waters with wind-roughened surfaces, part 2: User's guide and code listing. Technical report, DTIC Document, 1988.

[71] Curtis D. Mobley. HYDROLIGHT TECHNICAL NOTE 4 - THE RADTRAN-X ATMOSPHERIC IRRADIANCE MODEL. Technical report, 1992.

[72] Curtis D. Mobley. *Light and Water: Radiative Transfer in Natural Waters*. Academic Press, 1994.

[73] Curtis D. Mobley, Bernard Gentili, Howard R. Gordon, Zhonghai Jin, George W. Kattawar, André Morel, Phillip Reinersman, Knut Stamnes, and Robert H. Stavn. Comparison of numerical models for computing underwater light fields. *Appl. Opt.*, 32(36):7484–7504, Dec 1993. doi: 10.1364/AO.32.007484. URL `http://ao.osa.org/abstract.cfm?URI=ao-32-36-7484`.

[74] Andre Morel. Optical properties of pure water and pure sea water. *Optical aspects of oceanography*, 1:1–24, 1974.

[75] André Morel. In-water and remote measurements of ocean color. *Boundary-Layer Meteorology*, 18(2):177–201, 1980.

[76] André Morel. Optical Modeling of Upper Ocean in Relation to its Biogenous Matter Content (Case 1 Waters). *Journal of Geophysical Research*, 93:10,749–10,768, 1988.

[77] André Morel and Bernard Gentili. Diffuse reflectance of oceanic waters: its dependence on sun angle as influenced by the molecular scattering contribution. *Applied optics*, 30(30):4427–4438, 1991.

[78] André Morel, Bernard Gentili, Hervé Claustre, Marcel Babin, Annick Bricaud, Joséphine Ras, and Fanny Tieche. Optical properties of the clearest natural waters. *Limnology and oceanography*, 52(1):217–229, 2007.

[79] W. F. Murphy and H. J. Bernstein. Raman spectra and an assignment of the vibrational stretching region of water. *The Journal of Physical Chemistry*, 76(8):1147–1152, 1972. doi: 10.1021/j100652a010. URL `http://pubs.acs.org/doi/abs/10.1021/j100652a010`.

[80] Teruyuki Nakajima and Masayuki Tanaka. Effect of wind-generated waves on the transfer of solar radiation in the atmosphere-ocean system. *Journal of Quantitative Spectroscopy and Radiative Transfer*, 29(6):521–537, 1983.

[81] Daniel Odermatt, Carsten Brockmann, and Lena Kritten. SIOCS process development - algorithm theoretical document basis document, 2014.

[82] Annamaneni Peraiah. *An Introduction to Radiative Transfer: Methods and applications in astrophysics*. Cambridge University Press, 2002.

[83] Theodore J. Petzold. Volume scattering functions for selected ocean waters. University of California, San Diego, SCRIPPS Ins. of Oceanography, October 1972.

[84] Gilbert N Plass and George W Kattawar. Monte Carlo calculations of radiative transfer in the earth's atmosphere-ocean system: I. flux in the atmosphere and ocean. *Journal of Physical Oceanography*, 2(2):139–145, 1972.

[85] Gilbert N Plass, George W Kattawar, and Frances E Catchings. Matrix operator theory of radiative transfer. 1: Rayleigh scattering. *Applied Optics*, 12(2):314–329, 1973.

[86] Plumbago. Average sea surface chlorophyll for the period january 1998 to december 2006 from the seawifs satellite. Plumbago at English Wikipedia [CC BY-SA 3.0 (http://creativecommons.org/licenses/by-sa/3.0) or GFDL (http://www.gnu.org/copyleft/fdl.html)], via Wikimedia Commons, 2008. URL `http://commons.wikimedia.org/wiki/File%3AAYool_SEAWIFS_annual.png`.

[87] Robin M. Pope and Edward S. Fry. Absorption spectrum (380–700 nm) of pure water. II. integrating cavity measurements. *Appl. Opt.*, 36(33):8710–8723, Nov 1997. doi: 10.1364/AO.36.008710. URL `http://ao.osa.org/abstract.cfm?URI=ao-36-33-8710`.

[88] S. P. S. Porto. Angular dependence and depolarization ratio of the Raman effect. *J. Opt. Soc. Am.*, 56(11):1585–1586, Nov 1966. doi: 10.1364/JOSA.56.001585. URL `http://www.opticsinfobase.org/abstract.cfm?URI=josa-56-11-1585`.

[89] John F Potter. The delta function approximation in radiative transfer theory. *Journal of the Atmospheric Sciences*, 27(6):943–949, 1970.

[90] Rudolph W Preisendorfer and Curtis D Mobley. Theory of fluorescent irradiance fields in natural waters. *Journal of Geophysical Research: Atmospheres (1984–2012)*, 93(D9):10831–10855, 1988.

[91] Louis Prieur and Shubha Sathyendranath. An optical classification of coastal and oceanic waters based on the specific spectral absorption curves of phytoplankton pigments, dissolved organic matter, and other particulate materials1. *Limnology and Oceanography*, 26(4):671–689, 1981.

[92] Xiaohong Quan and Edward S Fry. Empirical equation for the index of refraction of seawater. *Applied Optics*, 34(18):3477–3480, 1995.

[93] TI Quickenden and JA Irvin. The ultraviolet absorption spectrum of liquid water. *The Journal of Chemical Physics*, 72(8):4416–4428, 1980.

[94] Chandrasekhara Venkata Raman. A new radiation. *Indian Journal of physics*, 2: 387–398, 1928.

[95] M Rast, JL Bezy, and S Bruzzi. The ESA medium resolution imaging spectrometer MERIS a review of the instrument and its mission. *International Journal of Remote Sensing*, 20(9):1681–1702, 1999.

[96] Raymond Redheffer. On the relation of transmission-line theory to scattering and transfer. *J. Math. Phys.*, 41, 1962.

[97] Clive D Rodgers. Inverse methods for atmospheric sounding-theory and practice. *Inverse Methods for Atmospheric Sounding-Theory and Practice. Series: Series on Atmospheric Oceanic and Planetary Physics, ISBN: 9789812813718. World Scientific Publishing Co. Pte. Ltd., Edited by Clive D. Rodgers, vol. 2*, 2, 2000.

[98] NP Romanov and VS Shuklin. Raman scattering cross section of liquid water. *Optics and Spectroscopy*, 38:646–648, 1975.

[99] LS Rothman, IE Gordon, Y Babikov, A Barbe, D Chris Benner, PF Bernath, Manfred Birk, L Bizzocchi, V Boudon, LR Brown, et al. The HITRAN2012 molecular spectroscopic database. *Journal of Quantitative Spectroscopy and Radiative Transfer*, 130:4–50, 2013. URL `http://www.sciencedirect.com/science/article/pii/S0022407313002859`.

[100] Rüdiger Röttgers, Roland Doerfer, David McKee, and Wolfgang Schönfeld. Pure water spectral absorbtion, scattering, and real part of refractive index model. Algorithm Technical Basis Document, 2010.

[101] Rüdiger Röttgers, David McKee, and Christian Utschig. Temperature and salinity correction coefficients for light absorption by water in the visible to infrared spectral region. *Opt. Express*, 22(21):25093–25108, Oct 2014. doi: 10.1364/OE.22.025093. URL `http://www.opticsexpress.org/abstract.cfm?URI=oe-22-21-25093`.

[102] VV Rozanov, AV Rozanov, AA Kokhanovsky, and JP Burrows. Radiative transfer through terrestrial atmosphere and ocean: software package sciatran. *Journal of Quantitative Spectroscopy and Radiative Transfer*, 133:13–71, 2014.

[103] Roland Doerffer Jürgen Fischer Andre Hollstein Jonas von Bismarck Samntha Lavender Wolfgang Schönfeld Rüdiger Röttgers, Carsten Brockmann. The STSE-WaterRadiance project Final Report. Technical report, ESA, 2012.

[104] Shubha Sathyendranath and Trevor Platt. Ocean-color model incorporating transspectral processes. *Appl. Opt.*, 37(12):2216–2227, Apr 1998. doi: 10.1364/AO.37.002216. URL `http://ao.osa.org/abstract.cfm?URI=ao-37-12-2216`.

[105] Marc Schroeder, Hans Barth, and Rainer Reuter. Effect of inelastic scattering on underwater daylight in the ocean: Model evaluation, validation, and first results. *Appl. Opt.*, 42(21):4244–4260, Jul 2003. doi: 10.1364/AO.42.004244. URL `http://ao.osa.org/abstract.cfm?URI=ao-42-21-4244`.

[106] Karl Schwarzschild. Über das Gleichgewicht der Sonnenatmosphäre. *Göttinger Nachr*, 41, 1906.

[107] David J. Segelstein. *The complex refractive index of water*. PhD thesis, Department of Physics, University of Missouri Kansas City, 1981.

[108] Adolf Smekal. Zur Quantentheorie der Dispersion. *Naturwissenschaften*, 11(43): 873–875, 1923.

[109] Raymond C. Smith and Karen S. Baker. Optical properties of the clearest natural waters (200–800 nm). *Appl. Opt.*, 20(2):177–184, Jan 1981. doi: 10.1364/AO.20.000177. URL `http://ao.osa.org/abstract.cfm?URI=ao-20-2-177`.

[110] Robert Spurr, Johan de Haan, Roeland van Oss, and Alexander Vasilkov. Discrete-ordinate radiative transfer in a stratified medium with first-order rotational Raman scattering. *Journal of Quantitative Spectroscopy and Radiative Transfer*, 109(3):404–425, 2008.

[111] Knut Stamnes, S-Chee Tsay, Warren Wiscombe, Kolf Jayaweera, et al. Numerically stable algorithm for discrete-ordinate-method radiative transfer in multiple scattering and emitting layered media. *Applied optics*, 27(12):2502–2509, 1988.

[112] George G Stokes. On the intensity of the light reflected from or transmitted through a pile of plates. *Proceedings of the Royal Society of London*, 11:545–556, 1862.

[113] Arthur H Stroud and Don Secrest. *Gaussian quadrature formulas*, volume 374. Prentice-Hall Englewood Cliffs, NJ, 1966.

[114] Shigehiko Sugihara, Motoaki Kishino, and Noboru Okami. Contribution of Raman scattering to upward irradiance in the sea. *Journal of the Oceanographical Society of Japan*, 40(6):397–404, 1984. ISSN 0029-8131. doi: 10.1007/BF02303065. URL `http://dx.doi.org/10.1007/BF02303065`.

[115] M Tanaka. Radiative transfer in turbid atmospheres. i. matrix analysis for the problem of diffuse reflection and transmission. *J .Meteorol. Soc. Japan*, 49:296–312, 1971.

[116] Sentinel-3 Team. *Sentinel-3 User Handbook*. ESA, 1.0 edition, 2013.

[117] Eugene D Traganza. Fluorescence excitation and emission spectra of dissolved organic matter in sea water. *Bulletin of Marine Science*, 19(4):897–904, 1969.

[118] F.H. Tukhvatullin, V.Ye. Pogorelov, A. Jumabaev, H.A. Hushvaktov, A.A. Absanov, and A. Usarov. Polarized components of Raman spectra of o-h vibrations in liquid water. *Journal of Molecular Liquids*, 160(2):88 – 93, 2011. ISSN 0167-7322. doi: http://dx.doi.org/10.1016/j.molliq.2011.02.015. URL `http://www.sciencedirect.com/science/article/pii/S0167732211000729`.

[119] S Twomey, H Jacobowitz, and HB Howell. Matrix methods for multiple-scattering problems. *Journal of Atmospheric Sciences*, 23:289–298, 1966.

[120] Alexander P Vasilkov, Joanna Joiner, James Gleason, and Pawan K Bhartia. Ocean Raman scattering in satellite backscatter uv measurements. *Geophysical research letters*, 29(17):18–1, 2002.

[121] Jonas von Bismarck and Jürgen Fischer. An examination of errors in computed water-leaving radiances due to a simplified treatment of water Raman scattering effects. In *RADIATION PROCESSES IN THE ATMOSPHERE AND OCEAN (IRS2012): Proceedings of the International Radiation Symposium (IRC/IAMAS)*, volume 1531, pages 939–942. AIP Publishing, 2013.

[122] Jonas von Bismarck and Jürgen Fischer. The inclusion of Raman scattering effects in the combined ocean-atmosphere radiative transfer model momo to estimate the influence of Raman scattering in Case 1 waters on satellite ocean remote sensing applications. In *AGU Fall Meeting Abstracts*, page A7, 2011.

[123] Jonas von Bismarck and Jürgen Fischer. Quantitatively computed effects of water Raman scattering on water leaving radiances. ESA *support to science* project *waterradiance* document (contract AO 1-5859/08/NL/CT), 2011.

[124] Jonas von Bismarck and Jürgen Fischer. Validation report for MOMO including Raman scattering effects. ESA *support to science* project *waterradiance* document (contract AO 1-5859/08/NL/CT), September 2011.

[125] Jonas von Bismarck and Jürgen Fischer. Quantitative computed contribution of Raman scattering to water-leaving radiances. In *International Radiation symposium 2012, IRS2012-316*, 2012.

[126] G. E. Walrafen. Raman spectral studies of the effects of temperature on water structure. *J. Chem. Phys.*, 47, 1967.

[127] G. E. Walrafen. Continuum model of water-an erroneous interpretation. *J. Chem. Phys.*, 50:567–569, 1969.

[128] L. Wang. *Measuring optical absorption coefficient of pure water in UV using the integrating cavity absorption meter,*. PhD thesis, Texan A&M University, 2008.

[129] Kirk J. Waters. Effects of Raman scattering on the water-leaving radiance. *Journal of Geophysical Research: Oceans*, 100(C7):13151–13161, 1995. ISSN 2156-2202. doi: 10.1029/95JC00530. URL `http://dx.doi.org/10.1029/95JC00530`.

[130] David M. Wieliczka, Shengshan Weng, and Marvin R. Querry. Wedge shaped cell for highly absorbent liquids: infrared optical constants of water. *Appl. Opt.*, 28(9): 1714–1719, 1989. URL `http://ao.osa.org/abstract.cfm?URI=ao-28-9-1714`.

[131] Xin Xu. *Significance of Raman Scattering in the Ocean.* PhD thesis, Texas A&M University, 1994.

[132] Xin Xu and George W. Kattawar. Filling in of Fraunhofer lines in the ocean by Brillouin scattering. *Appl. Opt.*, 33(21):4835–4840, Jul 1994. doi: 10.1364/AO.33.004835. URL `http://ao.osa.org/abstract.cfm?URI=ao-33-21-4835`.

[133] Andrew T Young. Rayleigh scattering. *Appl. Opt*, 20(4):533–535, 1981.

[134] Peng-Wang Zhai, Yongxiang Hu, Jacek Chowdhary, Charles R Trepte, Patricia L Lucker, and Damien B Josset. A vector radiative transfer model for coupled atmosphere and ocean systems with a rough interface. *Journal of Quantitative Spectroscopy and Radiative Transfer*, 111(7):1025–1040, 2010.

[135] Tinglu Zhang, Frank Fell, Zhi-Shen Liu, René Preusker, Jürgen Fischer, and Ming-Xia He. Evaluating the performance of artificial neural network techniques for pigment retrieval from ocean color in Case I waters. *Journal of Geophysical Research: Oceans (1978–2012)*, 108(C9), 2003.

[136] Xiaodong Zhang, Lianbo Hu, and Ming-Xia He. Scattering by pure seawater: effect of salinity. *Optics express*, 17(7):5698–5710, 2009. URL `http://www.opticsinfobase.org/abstract.cfm?uri=oe-17-7-5698`.

Danksagung

Zunächst möchte ich meinem Doktorvater Prof. Dr. Jürgen Fischer danken, bei mir das Interesse an diesem großartigen Forschungsprojekt geweckt und mich bei dem Vorhaben seither unterstützt zu haben. Prof. Dr. Ralf Bennartz möchte ich für seine Bereitschaft danken, das Zweitgutachten zu übernehmen, aber auch für die interessanten Diskussionen und Fragestellungen, die er zu meiner Arbeit beigetragen hat. Darüberhinaus möchte ich André Hollstein, Cristopher Kyba, Thomas Ruhtz, Lena Kritten, Hannes Diedrich, Rene Preusker, Lionel Doppler, Cintia Carbajal-Henken, Gisela Brass, Sören Testorp, Nicole Docter, Florian Fillipitsch und natürlich auch allen anderen Kollegen für die Unterstützung, gute Zusammenarbeit und die interessanten und lustigen Gespräche danken. Meiner Lebensgefährtin Frederike Steinhoff und unserem Sohn Matteo möchte ich ebenfalls von ganzem Herzen für die Ausdauer, das Verständnis und die Unterstützung danken. Der U1 und der U9 danke ich für ihren fast täglichen zuverlässigen Dienst. Auch möchte ich auf die Finanzierung eines Teils der vorgestellten Arbeiten durch die ESA (STSE Projekt WaterRadiance) sowie das DLR und das BMWi (SIOCS Projekt) hinweisen.

Erklärung:

Ich versichere, dass ich diese Arbeit selbständig verfasst und keine anderen, als die angegebenen Quellen und Hilfsmittel benutzt habe. Diese Arbeit wurde in keinem früheren Promotionsverfahren eingereicht. Die Arbeit wurde ohne unzulässige Hilfe Dritter verfasst.

Ort, Datum	Unterschrift